

FINE-TUNING PLASMONIC RESPONSE FOR PLASMON-ENHANCED
PHOTONICS

A THESIS SUBMITTED TO
THE GRADUATE SCHOOL OF NATURAL AND APPLIED SCIENCES
OF
MIDDLE EAST TECHNICAL UNIVERSITY

BY

İBRAHİM MURAT ÖZTÜRK

IN PARTIAL FULFILLMENT OF THE REQUIREMENTS
FOR
THE DEGREE OF DOCTOR OF PHILOSOPHY
IN
PHYSICS

DECEMBER 2023

Approval of the thesis:

**FINE-TUNING PLASMONIC RESPONSE FOR PLASMON-ENHANCED
PHOTONICS**

submitted by **İBRAHİM MURAT ÖZTÜRK** in partial fulfillment of the requirements for the degree of **Doctor of Philosophy in Physics, Middle East Technical University** by,

Prof. Dr. Halil Kalıpçılar
Dean, **Graduate School of Natural and Applied Sciences** _____

Prof. Dr. Seçkin Kürkçüoğlu
Head of the Department, **Physics** _____

Prof. Dr. Alpan Bek
Supervisor, **Physics, METU** _____

Examining Committee Members:

Prof. Dr. Mehmet Emre Taşgın
Institute of Nuclear Sciences, Hacettepe University _____

Prof. Dr. Alpan Bek
Physics, METU _____

Assist. Prof. Dr. Ihor Pavlov
Physics, METU _____

Prof. Dr. Okan Esentürk
Chemistry, METU _____

Assoc. Prof. Dr. Ramazan Şahin
Physics, Akdeniz University _____

Date: 08.12.2023

I hereby declare that all information in this document has been obtained and presented in accordance with academic rules and ethical conduct. I also declare that, as required by these rules and conduct, I have fully cited and referenced all material and results that are not original to this work.

Name, Surname : İbrahim Murat Öztürk

Signature :

ABSTRACT

FINE-TUNING PLASMONIC RESPONSE FOR PLASMON-ENHANCED PHOTONICS

Öztürk, İbrahim Murat
Doctor of Philosophy, Physics
Supervisor : Prof. Dr. Alpan Bek

December 2023, 162 pages

Plasmonic interactions have found extensive applications in both industrial and fundamental scientific domains owing to scattering, absorption, and electric field enhancement properties of metal nano-structures. The oscillation of metal's free electrons, driven by the light's field, results highly geometry-dependent optical response with resonances at specific frequency bands. Tuning the plasmonic response for specific applications requires computer-aided simulations guiding the fabrications. In fact, recent advancements of nano-photonics owe to three collaborative efforts in fabrication, measurements, and simulations. In this thesis, hole mask lithography was chosen as the nano-fabrication method due to its large area compatibility and diverse geometrical potential. This method had successfully used for fabrication of both simple and complex geometries of nano-structures. Innovative approaches to control the surface distribution of nanostructures have been proposed, experimentally explored and yielded promising discussions. Experimental measurements are repeatedly modelled with computational tools. The simulation credibility improved when matching results are obtained from two different computational method, boundary element method and finite element method.

Plasmonic coupling is explored with Surface Enhanced Raman Scattering measurements of dimer disc fabrications with varied gap distances, indicating fields intensify at smaller interparticle gaps. A model is invented for quantitation of the plasmonic influence on the efficiency of nano-structure decorated photovoltaics. The model is used for quantitative comparison of various nano-geometries and materials at various physical surface coverages.

Keywords: Nano-optics, Plasmonics, Computational electrodynamics, Nano-fabrication.

ÖZ

PLAZMONİK TEPKİNİN HASSAS AYARLANMASI İLE PLAZMON- DESTEKLİ FOTONİK

Öztürk, İbrahim Murat
Doktora, Fizik
Tez Yöneticisi: Prof. Dr. Alpan Bek

Aralık 2023, 162 sayfa

Plazmonik etkileşimler metal nano-yapıların saçılma, emilim ve elektrik alanını artırma özellikleri sayesinde endüstriyel ve temel bilimsel alanlarda geniş kullanım alanı bulmaktadır. Işığın alanı tarafından sürülen serbest metal elektronlarının salınımı, belirli frekans bantlarında rezonansların meydana geldiği, geometriye güçlü-bağlı optik bir tepki oluşturur. Plazmonik tepkinin belirli uygulamalar için ayarlanması, üretimleri yönlendiren bilgisayar destekli simülasyonları gerektirmektedir. Nano-fotonik alanındaki yeni gelişmeler, üretim, ölçüm ve simülasyon alanlarında üçlü iş birliğine dayanmaktadır. Tez çalışmalarında nano-üretim yöntemi olarak deşik maske litografisi seçilmiştir, bu yöntem geniş alanlara uygulanabilir olması ve yüksek geometrik çeşitlilikte nano-yapı üretimine olanak vermesi ile öne çıkmaktadır. Bu yöntem kullanılarak çeşitli basit ve karmaşık nano-yapıların üretimi yapılmış, yapıların yüzey dağılımı kontrolü için yenilikçi fikirler test edilmiş umut vadeden değerlendirmeler elde edilmiştir. Optik Ölçümler tekrarlı olarak simülasyon araçlarında modellenmiştir. Sonlu eleman yöntemi ile sınır eleman yöntemi hesaplamalarda kullanılarak, iki farklı yöntemle aynı sonuçların

elde edilmesi hesaplamaların güvenilirliğini artırmıştır. Plazmonik kenetlenme farklı aralıklarda ikili disk yapıların üretimleri kullanılarak yüzey artırımı Raman spektroskopisi kullanılarak incelenmiş, küçülen aralıklarda alan yoğunlaşması gözlenmiştir. Plazmonik nano-yapılarla dekore edilmiş fotovoltaiik sistem uygulamalarında herhangi yapı geometrisi ve yüzey doluluđu için plazmonik yapıların etkisinin sayısal olarak değeriendirebilmesini sađlayan bir model geliřtirilerek, çeřitli nano-yapıların fotovoltaiik verimliliđine etkisi sayısal olarak incelenmiştir.

Anahtar Kelimeler: Nano-optik, Plazmonik, Hesaplamalı elektrodinamik, Nano üretim.

For my children

ACKNOWLEDGMENTS

I am deeply indebted to Dr. Alpan Bek, whose excellent guidance and scholarly wisdom have always been motivated me for my academic pursuits. Serving as my thesis advisor for over a decade, his excellent support and insightful direction have been immensely valuable. He has been more than an advisor, more like a role model effecting my life positively in many various aspects. His remarkable dedication to excellence, ethical approach to research, and commitment to fostering an environment of collaboration and growth have been truly inspiring throughout my academic journey. His patience, integrity, and passion for knowledge have not only shaped my research but also served as a guiding light in my personal and professional development.

I would like to express my deepest gratitude to Dr. Mehmet Emre Taşgın who has always been supportive, he introduced me to the numerical calculation methods that I used throughout my thesis, enhanced my view of physics with stimulating ideas in his excellent courses that I got the opportunity to join. I would like to thank Dr. Emre Yüce for listening many of my thesis progress presentations, he always guided me towards the better path. And I would like to thank my other jury members Dr. Ihor Pavlov, Dr. Ramazan Şahin, and Dr. Okan Esentürk. I also want to deeply thank Dr. Sadi Turgut from whom I got the opportunity to learn graduate level quantum mechanics and statistical thermodynamics, both of these courses expanded my physics view to a new level with his excellent explanations and ingenious questions. I want to express my gratitude to all my professors from METU Physics department, all of whom have been cornerstones in my learning through the courses and discussions.

My beloved wife, mother of my children, Zeynep Nilüfer Öztürk, whose unwavering love and support have been the cornerstone of my journey. Her endless encouragement, patience, and understanding have been my guiding light through

every challenge. Her presence has transformed difficult moments into opportunities for growth, her belief in my capabilities has been my greatest strength.

I thank and wish the best for to all my friends and colleagues; Hakan Keskin, Fırat İdikut, Özge Demirtaş, M. Kurtuluş Abak, Zeynep Cantürk, Hisham Naser, Tahir Çolakoğlu, Mona Borra, Burcu Altuntaş, S. S. Esmeilzad, Hüseyin Tepe, Mustafa Ünal, Ahmet Ünal, Zeynep Demircioğlu, B. Berkan Turgut, Tayfun Çelik, Zeynep Baz, A. Nur Eroğlu, Egemen Bilek, Selen Postacı, Emirhan Postacı, M. Sinan Yayla, Gence Bektaş, Fatih Ballı, Gamze K. Başlar, and all others that I forgot to mention.

I extend my deepest gratitude to my parents, Mustafa Öztürk and Melek Öztürk, whose support has been instrumental throughout my educational journey. Their encouragement and guidance have been invaluable at every step. I'm grateful to my dear little sisters, Zeynep Cansu Öztürk and Elif Göksu Öztürk, for their constant love and support.

I am grateful to Günam for generously providing access to their state-of-the-art laboratories and advanced equipment, which significantly contributed to the success of this research.

This work is partially funded by TÜBİTAK: The Scientific and Technological Research Council of Turkey under grant numbers 115F167 and 118M003.

TABLE OF CONTENTS

ABSTRACT	v
ÖZ.....	vii
ACKNOWLEDGMENTS	x
TABLE OF CONTENTS	xii
LIST OF TABLES	xv
LIST OF FIGURES	xvi
LIST OF ABBREVIATIONS	xxiii
CHAPTERS	
1 INTRODUCTION	1
1.1 History of Plasmonics.....	4
1.2 Literature Review	6
1.2.1 Nanofabrication	10
1.2.2 Computational Plasmonics	19
1.2.3 Surface Enhanced Raman Scattering (SERS).....	21
1.2.4 Plasmon-Enhanced Solar Cells	26
2 THE PLASMONIC INTERACTION	29
2.1 Light Interaction with Metals	30
2.1.1 Optical Constants	32
2.1.2 Optical Properties of Metals	34
2.2 Metals Under Illumination: Mie Theory	37
2.2.1 EM Field in The Vicinity of MNP	41
2.2.2 Scattering and Absorption	43

3	METHODOLOGY	47
3.1	Surface Nano-Structuring with Hole Mask Lithography	47
3.1.1	Hole Mask Colloidal Lithography.....	55
3.1.2	Hole Size Reduction.....	62
3.1.3	Strategies for Periodic Structuring With HMCL.....	66
3.2	Optical Characterization	71
3.3	Numerical Simulations.....	74
3.3.1	Cross Validation.....	77
3.3.2	Considerations about Discretization.....	81
3.3.3	Model Building	84
3.3.4	Experimental Validation	86
4	EXPLORATION OF PLASMONIC RESPONSE	89
4.1	Coupling of Closely Spaced MNPs	90
4.1.1	Scattering Cross-section Analyses	92
4.1.2	Field Enhancement Near Dimers	95
4.2	Fabrication and Analysis of Complicated Geometries	100
4.2.1	Scattering Measurements	104
4.2.2	Examination of Annealing	107
4.3	Preferential Scattering Calculations for Plasmon Enhanced Photovoltaics	110
4.4	A Model for Quantification of Plasmonic Contribution to Photovoltaics ..	116
4.4.1	Comparison of Basic Plasmon Geometries at Resonance.....	119
4.4.2	Broadband Calculations	124
5	CONCLUSION.....	133
	REFERENCES	137

APPENDICES

A. Mesh import into MNPBEM.....	153
B. DF Objective Matched Scattering Calculation in MNPBEM	155
CURRICULUM VITAE	159

LIST OF TABLES

TABLES

Table 1. Comparison of lithography methods in terms of area, resolution, variety and cost. Adapted from [100].	18
Table 2. Calculated values for Ag disc of diameter 71 nm on 10 nm thick SiO ₂ on Si at 532 nm illumination	121
Table 3. Calculated values for Ag sphere of diameter 195 nm on 10 nm thick SiO ₂ on Si at 532 nm illumination.....	122
Table 4. Calculated values for Ag disc of diameter 190 nm and Au disc of diameter 160 nm on 10 nm thick SiO ₂ on Si at 1000 nm illumination	123
Table 5. Comparison of the absorption contribution results for all four analyzed geometries	123

LIST OF FIGURES

FIGURES

Figure 1.1. Famous Lycurgus cup. Left: Front illuminated , right: Back illuminated. Retrieved from [2]	4
Figure 1.2. Number of articles published annually in the domains of plasmonics (blue) and metamaterials (yellow). Interior shots display significant landmark publications. Figure adapted [31].	7
Figure 1.3. A schematic setup for molecule detection by SPP excitation. Adapted from [34].	8
Figure 1.4. SEM images of nano geometries produced in a hexagonal array structure by evaporation of material from modified gaps between consecutive nanospheres by adjusting the polar and azimuth angles. Adapted from [94].	15
Figure 1.5. Right: Various metal structures produced using fixed-angle evaporation Left: Nanostructures fabricated using motorized sample holder-enhanced HML. Adapted from [95] and [96].	16
Figure 1.6. SERS measurements from HMCL fabricated substrates, adapted from [97]	17
Figure 1.7. The three different types of electromagnetic light scattering.	22
Figure 1.8. Images of various SERS substrates reported in literature, figure adapted from [157].	24
Figure 1.9. Up: SEM images of gold nanoparticles with four different surface morphology. Mid: 3D models based on SEM images. Down: Calculated field distributions. Adapted from [190].	25
Figure 1.10. Three distinct mechanisms can be employed for plasmon-enhanced photovoltaic applications. Adapted from [194].	26
Figure 1.11. Simulation results for comparison of a 60nm side Ag cube with a sphere. Left: field enhancement and angular scattering distribution. Right: Spectral graph of forward scattering ratio. Adapted from [196].	27

Figure 2.1. (a) Surface plasmon polaritons on a metal-dielectric interface. (b) Excitation of LSP by illumination of subwavelength MNPs.....	38
Figure 2.2. Electric field distribution calculation near a spherical Ag nanosphere when illuminated with 532nm, the graph shows the field decay on the field calculation line	42
Figure 2.3. Scattering and absorption cross-sections calculated for Au spheres of increasing diameters.....	44
Figure 2.4. Spectral scattering efficiency calculated for different diameters of Au nano spheres	45
Figure 2.5. Spectral scattering efficiency calculated for large diameters of Au nanospheres	46
Figure 3.1. Visualization of directional material deposition through undercut holes in Hole Mask Lithography	48
Figure 3.2. Hole mask lithography material deposition through the holes	49
Figure 3.3. Left: An illustration of deposition chamber setup for achieving continuous control in undercut region. Right: Achievable geometries with material evaporation with varying only one angle.....	50
Figure 3.4. SEM image of split-ring resonators fabricated with continuous back and forward rotation at a fixed tilt angle	51
Figure 3.5. Fabricated asymmetrical Ag dimers on Si substrate with 40 – 60 nm and 40 – 75 nm thicknesses.....	52
Figure 3.6. Multi-material dimer fabrication, 150nm hole diameter with 40 nm Ag and 20 nm Au deposition at fixed tilt angle.	53
Figure 3.7. SEM images taken in between 3 consecutive evaporation of Ag at fixed 20° tilt angle showing hole shrinkage	54
Figure 3.8. SEM image of highly asymmetric Ag dimers fabricated by HMCL by utilization of hole shrinkage.....	54
Figure 3.9. Sample preparation for HMCL, a schematic procedure	56
Figure 3.10. SEM images taken after hole mask preparation steps, nanosphere decoration, nanosphere removal and cavity formation from left to right.	56

Figure 3.11. Left: SEM image of a surface decorated with holes masked for grain analysis. Right: Size distribution histogram with grain analysis results averaged from 3 SEM images.....	60
Figure 3.12. SEM images of fabricated structures with complicated geometrical aspects.....	61
Figure 3.13. SEM images of PS nanosphere size reduction by Oxygen plasma etching (a) 500nm nanospheres as deposited (b) 5 minutes (c) 10 minutes (d) 20 minutes etched nanospheres	63
Figure 3.14. SEM images of hole size reduction tests by tilted evaporation of Au mask layer PS nanospheres of 500nm diameter are used. (a) no tilt (b) 10 ^o tilt (c) 20 ^o tilt (d) 30 ^o tilt.....	64
Figure 3.15. SEM images left: PMMA surface decorated with 170 nm silica nanospheres, right: hole mask layer after particle removal	65
Figure 3.16. SEM images of Left: close packed deposited 1 μ m spheres, right: reduced diameter spheres after 10 minutes O ₂ plasma etching	67
Figure 3.17. Schematic of Lloyd's mirror setup for interference lithography.	68
Figure 3.18. Proposed experimental procedure periodic hole mask fabrication with interference lithography.....	68
Figure 3.19. Left: AFM image of 27.5 sec orthogonally double exposed sample after development. Right: line cross-section analysis on the sample	69
Figure 3.20. Up: AFM images of 27.5 seconds exposed samples after oxygen plasma etching for 0min, 6min, 10 min and 20 min respectively. Down: The line cross-section plots taken from hole regions of respective images.	70
Figure 3.21. Left: schematic of dark field spectroscopy. Mid: The inverted microscope setup used in measurements. Right: A dark field image of a surface with different plasmonic resonances.	71
Figure 3.22. Left to right 174nm and 270nm average sized Au nanodiscs. Upper: SEM lower: Dark field optical microscope images.....	73
Figure 3.23. Dark field scattering spectra obtained from samples of Au nanodiscs of 175nm and 270nm average sizes respectively.....	73

Figure 3.24. A FEM simulation of periodic array of 100nm diameter discs. Left: Meshed geometry of 100nm disc on Si substrate. Mid: Electric field distribution on the substrate surface. Right: Calculated reflection and transmission coefficients. .	76
Figure 3.25. Workflow of simulations	77
Figure 3.26. Scattering cross-section of a 10nm diameter Au nanosphere, the comparison of Mie solution, quasistatic solution and retarded full Maxwell solution calculated using Mnpbem toolbox	78
Figure 3.27. Scattering cross-section of a 100 nm diameter Au nanodisc, comparison of quasistatic approximation and retarded full Maxwell solution	79
Figure 3.28. Comparison of scattering spectrum graphs calculated with MNPBEM and COMSOL. For a sphere with diameter 170 nm placed on 10nm SiO ₂ coated Si substrate	79
Figure 3.29. Comparison of scattering spectrum graphs calculated with MNPBEM and COMSOL for a 60 nm side length cube placed on 8, 12 and 19 nm of Si ₃ N ₄ coated Si substrate.....	80
Figure 3.30. Scattering cross-sections calculated for same structure but different meshing parameters using MNPBEM.....	82
Figure 3.31. Reflection and transmission coefficients of a surface covered with periodically placed Ag nanocubes calculated using Comsol. Left: coarse meshed cube (~2hr solution time), right: finer meshed cube (~10 hr solution time).....	83
Figure 3.32. Scattering absorption and extinction spectrum of a nanorod on glass for parallel and perpendicular illumination obtained by BEM simulations. Left: particle is 0.1 nm above the surface, right: particle is 0.5 nm above the surface ...	86
Figure 3.33. Calculations for a 175nm Au disc on glass. Up: Total of 18 simulations calculated for dark field objective illumination. Down: The average of all results is expected to match the experimental measurements.....	87
Figure 3.34. Left: SEM image of fabricated Ag discs with 150 nm average diameter Right: Measured scattering spectrum (blue) and Mnpbem simulation (red)	88
Figure 4.1. Simulation results for scattering spectra of 150 nm Ag dimers with varied gap size with normal illumination.....	90

Figure 4.2. Up: Surface distribution of fabricated dimers, down: Close up SEM view of dimers fabricated with fixed azimuth angle of ± 10 for dimer 1 and ± 9.5 degrees for dimer 2.....	91
Figure 4.3. Polarized illumination scattering spectra collected from dimer1 and dimer2, black curves are obtained with polarization axis parallel to dimer axis and red curves with perpendicular.	92
Figure 4.4. Scattering cross-section calculated for dimer gaps 10, 20 and 30 nm with DF objective matched illumination conditions	94
Figure 4.5. Relative electric field calculations around 100nm diameter dimers at 532nm illumination a) 5nm, b) 10nm, c) 20nm, d) 30nm, e) 40nm and f)100nm ..	96
Figure 4.6. Raman measurement collected from BCB coated dimer1, dimer2 and bare Si surface with unpolarized laser.....	97
Figure 4.7. Raman measurement collected with polarized laser for polarization direction is parallel (red) and perpendicular (black) to dimer axis from dimer-2 ...	98
Figure 4.8. Plot of electric field distribution on and around of a dimer with 150 nm disc diameter on Si with 10 nm gap with parallel polarized 532nm illumination...	99
Figure 4.9. SEM images of complicated nano-structures with rotation and evaporation parameters and structure names.....	102
Figure 4.10. SEM image array with thicknesses of several structures	103
Figure 4.11. Same structure left: on Si substrate right: on glass substrate	104
Figure 4.12. Scattering spectra of “exclamation mark” and two Gaussian peak fit analysis. Green curves show the sum of two fitted curves.....	105
Figure 4.13. Scattering spectra of “plus sign” and two Gaussian peak fit analysis. Green curves show the sum of two fitted curves.....	105
Figure 4.14. Scattering spectrum of “eye” structure	106
Figure 4.15. Scattering spectra of “egg” and “half circle with dots” structures....	107
Figure 4.16. Structural effects of annealing on fabricated structures, up: before, down: after annealing	108
Figure 4.17. Dark field spectrum before (black) and after annealing (red), insets for respective SEM images	108

Figure 4.18. two Gaussian peak fit analysis on “exclamation mark” after annealing. Green curves show the sum of two fitted curves.	109
Figure 4.19. Polarized DF spectrums of a dimer fabrication with thicker discs, left: before and right: after annealing.	110
Figure 4.20. Mnpbem simulation results. 3D polar plots for angular far field scattering distribution pattern for a) 100 nm diameter sphere b) 100 nm diameter disc at 800 nm wavelength. c) Hemisphere defined at infinity for poynting vector calculation.	111
Figure 4.21. Simulation results showing fraction of incident radiation scattered into substrate for 4 different plasmonic structures. Left: simulation results acquired from [213], right: Reproduction of results by Mnpbem simulations	112
Figure 4.22. Fraction scattered into Si substrate for Dimers and quadromers.....	113
Figure 4.23. Fraction scattered into Si substrate for rods of different aspect ratio, the short axis length is left: 100nm, right: 150 nm.	113
Figure 4.24. Angular distribution of pointing vector norm of scattered light inside the substrate. Left: A sphere, Right: A disc with 100nm diameter each at 500nm wavelength. Red lines indicate the TIR angle of Si/air interface	114
Figure 4.25. Calculation of the fraction of scattered light directed into guided modes of a thin film Si solar cell for different plasmonic structures.....	115
Figure 4.26. Calculated scattering and absorption efficiencies for discs on Si substrate. Blue curves are for disc diameter 100nm and green curves are for 150nm	116
Figure 4.27. Scattering cross-section calculations for finding the diameter of the disc resonant at 532nm on 10 nm thick SiO ₂ on Si substrate.....	120
Figure 4.28. Angular distribution of scattered radiation for Ag disc of diameter 71nm on 10 nm thick SiO ₂ on Si at 532 nm illumination	120
Figure 4.29. Angular distribution of scattered radiation for Ag sphere of diameter 195 nm on 10 nm thick SiO ₂ on Si at 532 nm illumination	121

Figure 4.30. Scattering, absorption and extinction efficiencies and plasmonic interaction factor calculations for 200nm Au Sphere. Left: surface coverage 20%, right: surface coverage 10%	124
Figure 4.31. Preferential scattering to substrate and total portion scattered into substrate calculations for 200nm Au sphere. Left: surface coverage 20%, right: surface coverage 10%. Inset: angular scattering distribution at 800nm	125
Figure 4.32. Plasmonic contribution to absorption calculations for 200nm Au sphere. Left: surface coverage 20%, right: surface coverage 10%	125
Figure 4.33. Left: Scattering, absorption and extinction efficiencies and plasmonic interaction factor calculations. Right: Plasmonic contribution to absorption calculations for 200nm Ag sphere with 15% surface coverage.....	126
Figure 4.34. Left: Scattering, absorption and extinction efficiencies and plasmonic interaction factor calculations. Right: Plasmonic contribution to absorption calculations for 100nm Au disc with 0.8 surface coverage.	127
Figure 4.35. Left: Scattering, absorption and extinction efficiencies and plasmonic interaction factor calculations. Right: Plasmonic contribution to absorption calculations for 100nm Ag disc with 0.4 surface coverage.....	128
Figure 4.36. Plasmonic contribution to absorption calculations for 100nm Ag disc with 70% surface coverage.....	128
Figure 4.37. Average plasmonic contribution to PV absorption plotted against surface coverage for the analyzed nanostructures.	129
Figure 4.38. Average plasmonic contribution to PV absorption plotted against surface coverage for Ag discs of various diameters.	130
Figure 4.39. Interaction efficiencies of a 100nm diameter Ag disk placed on Si substrate	130

LIST OF ABBREVIATIONS

ABBREVIATIONS

MNP	Metal Nano Particle
SPR	Surface Plasmon Resonance
SPP	Surface Plasmon Polariton
LSP	Localized Surface Plasmons
EOT	Extraordinary Light Transmission
SERS	Surface Enhanced Raman Scattering
EF	Enhancement Factor
HCL	Hole Mask Lithography
HMCL	Hole Mask Colloidal Lithography
HMIL	Hole Mask Interference Lithography
PMMA	polymethyl methacrylate
MEMS	Micro-Electro-Mechanical Systems
AFM	Atomic Force Microscopy
SEM	Scanning Electron Microscopy
EBL	Electron Beam Lithography
NIL	Nano Imprint Lithography
TEM	Transmission Electron Microscopy
UV	Ultra Violet
NIR	Near-Infrared

BEM	Boundary Element Method
FEM	Finite Element Method
FDTD	Finite-Difference Time Domain
DF	Dark Field
PV	Photovoltaic

CHAPTER 1

INTRODUCTION

Nanotechnology offers vast possibilities, while remarkable discoveries have been made, the world of nanotechnology continues to offer enormous opportunities. In the context of nanotechnology, nano-photonics assume an essential role. It specifically addresses the interaction between light and matter at the nanoscale. Some of the most intriguing nanophotonic interaction occurs when the material of the nanostructure is metal, in which the conduction band electrons collectively oscillate inside the structure. These oscillations may resonate depending on the geometry, material, and frequency. Surface plasmon resonances (SPR) are the resonance modes of these structures. Nanostructures can be nano-engineered for desired response. Plasmonics has revealed nano-optics with many remarkable phenomena, with far-reaching implications for both fundamental optics and practical applications. Tuning the plasmonic response for a specific application requires suitable nano-fabrication method and measurement setups together with computer aided simulations.

The most application-aimed plasmonic response mechanisms can be handled under two categories. Firstly, Metal nanoparticles (MNP) can trap and confine light energy in the form of plasmons in volumes much smaller than the wavelength of light itself. This phenomenon, known as "nanoscale light trapping," enables the concentration of light energy in extremely tiny regions (several nm). When the illumination frequency is resonant, localized surface plasmon resonance (LSPR) enables a highly localized and intensified field for a nearby matter to interact. The second mechanism appears at the far-field region, at least several tens of wavelengths away from the metallic structure, as scattering. When MNPs are illuminated with a broadband source and the scattering spectrum is collected, scattering peaks are observed at the resonance frequency. Near the resonance frequency, the scattering cross-section may

be several orders of magnitude higher than the geometrical cross-section of the nanostructure. This indicates that particles may interact with light in a much larger space than they actually occupy. The scattered light may be highly directional depending on the irregularity of surrounding media as well as the geometrical features of the structure.

Scattering from MNPs becomes intriguing when the scattering from an array of MNPs is considered; the scattering direction may differ compared to isolated particles due to the interference of scattered waves. This interference completely alters the far field distribution of scattered light. This property coincides with well-established the antenna theory and relatively newer research field Metamaterials. Metamaterials are engineered materials that can obtain unique optical properties and specific light manipulation capabilities at far-field regions. Very thin, periodically decorated surfaces can be engineered to work similarly to conventional optics like lenses; moreover, they can achieve light-bending properties that conventional optics cannot achieve.

In this chapter, the history of plasmonics is briefly summarized and an overview of recent advancements in plasmonics and plasmonic-related fields are discussed. There are many valuable articles published in this field over recent years; in this context, only a few selected papers could be discussed. Moreover, advancements in fabrication methods, computation methods, and some important applications, such as surface enhanced Raman scattering and photovoltaic applications are discussed.

Theoretical considerations are explored in CHAPTER 2. Optical constants are defined for the explanation of light-matter interaction. The Drude theory for the prediction of optical constants of metals is detailed. The analytical solutions of plasmonic resonance properties, scattering and absorption are shown with Mie theory. Indications of the results are discussed together with examples by computer-aided simulations.

The experimental and computational methodology employed in thesis is depicted in CHAPTER 3, discussing their capabilities, limitations, challenges, solutions,

examples, and improvements. The fabrication method of hole mask colloidal lithography (HMCL) is discussed in terms of its strengths and weaknesses. Experimental work involving optimization and application is detailed. Experimental studies about possible improvements in fabrication properties are explained. Issues experienced are noted, and their definitive or possible solution approaches are discussed. Computer-aided Modeling methods, considerations, and result validation approaches are detailed. Methods for the detection and resolution of wrong calculations have been discussed.

Application-oriented studies and results are detailed in CHAPTER 4. First, dimer fabrications and observation of plasmonic coupling of closely spaced structures have been shown. The indications of measurement results are discussed with simulations. Second, the fabrication attempts and the results of complicated nano-geometries are shown. Optical scattering measurements of some of these structures have been discussed with analyses and discussions. Finally, the calculation of directional light scattering properties of structures is shown. These calculations allowed the development of a novel model for predicting the overall plasmonic effect when the photovoltaic surface is decorated with MNPs. The model allows quantification of the plasmonic photovoltaic enhancement at varied physical surface coverage of nanoparticles with arbitrary nano-geometry at various sizes. Several geometries, sizes, and surface coverages of structures are explored using the model. Results and indications are discussed.

1.1 History of Plasmonics

The earliest known application of surface plasmons in human history is found in an artwork called the Lucurgus Cup. This artifact is believed to have been unintentionally produced during the fourth century. Individuals were drawn to this particular piece of work because of the noticeable color difference between the reflected and transmitted light, a dichroic effect, as shown in Figure 1.1. In contemporary times, there exist church windows that employ the same phenomenon. The dichroic effect is attained by the incorporation of minute quantities of gold and silver nanoparticles distributed in the colloidal form inside the glass matrix. The methodology employed in this fabrication remains to be determined. The scientific understanding of the mechanisms behind this optical response developed far later than their practical use [1].



Figure 1.1. Famous Lycurgus cup. Left: Front illuminated , right: Back illuminated.

Retrieved from [2]

Michael Faraday carried out the first published studies with plasmonic nanostructures during the mid-19th century. He successfully created colloidal solutions comprised of gold nanoparticles, meticulously analyzed them, and afterward referred to them as “*Activated Gold*” [3]. Approximately four decades after Faraday’s research about the creation of colloidal gold particles, Richard Zsigmondy successfully observed these particles using the “*ultra-microscope*”, an invention of his own [4]. Subsequently, Gustav Mie conducted theoretical calculations by solving Maxwell's equations to determine the absorption and scattering properties of spherical metal nanostructures [5]. The calculations formulated by Mie continue to be extensively employed within the plasmonics field [6], [7].

In 1902, an intriguing plasmonic phenomenon was found by Robert Wood [30]. During the investigation of reflections originating from metallic gratings, the researcher encountered spectral characteristics that posed difficulties for explanation [8]. Subsequently, it was shown that these phenomena corresponded to the excitation of surface plasmon resonances within the gratings [9]. The term "plasmon" was initially introduced by David Pines in the 1950s to describe a form of high-frequency electron oscillations observed in metals [10]. The plasmon is a quasiparticle that arises as a consequence of the quantization of plasma oscillations. During the mid-1970s, Martin Fleischman observed of significant Raman scattering signals emanating from molecules on uneven metal surfaces [11]. This phenomenon was subsequently termed surface-enhanced Raman scattering (SERS) [12]. SERS has been attributed to generating of highly amplified local electromagnetic fields through surface plasmon resonances.

Before the end of the 20th century, investigations related to surface plasmons were conducted individually without a unified name for the topic. However, a significant milestone in achieving an accurate understanding of this field was the discovery of extraordinary optical transmission (EOT). Extraordinary optical transmission (EOT) refers to the phenomenon of light propagation through sub-wavelength apertures on thick metal films at significantly greater levels than what was initially calculated

[13], [14]. The phenomenon under consideration, observed within the apertures, can be elucidated through the concept of plasmon resonances. The enhanced ability to confine and manipulate light at the sub-nanometer scale has significantly contributed to the growing interest in plasmonic interactions, leading to the establishment and development of the field of plasmonics as it exists today.

Plasmonics has gained unprecedented popularity among scientists and engineers. Researchers are actively exploring the intriguing properties of plasmonic MNPs to unlock new scientific discoveries. Simultaneously, optical engineers are designing innovative devices that harness these properties for diverse industrial applications.

1.2 Literature Review

Many researchers have been drawn to the field of plasmonics since the beginning of the 21st century. In 2001, H. A. Atwater's paper gathered researchers' interest in this promising research area by emphasizing plasmonics as the route for nano-scale optical devices [15]. Plasmonic nanostructures have a great potential to reduce the size and increase the speed of electronic chips [16]. In addition to their exciting potential in information technology, plasmonic MNPs have undergone significant developments that enhance detection, renewable energy, and sensing [17]–[22]. And are the foundation of many applications due to their unique optical characteristics.

A review article published in 2017 highlights the exponential growth of plasmonic investigations in recent years. Figure 1.2 presents ground-breaking work in the field of plasmonics and metamaterials. Interior pictures show landmark studies chosen by writers. From the left side of Figure 1.2, the landmarks are extraordinary optical transmission (EOT) through subwavelength apertures [13], [23], lasing at the nanoscale [24], optical antennas [25], plasmonic nano-printing [26], graphene plasmonics [27], metamaterials [28], cloaking [29] and negative refraction [30], respectively. The article predicts that the scientific discoveries in these study fields will continue to develop and eventually become a part of everyday technology. The

authors emphasize how various seemingly distinct research fields have been brought together by plasmonic research, and they argue that these connections offer optimism for the future of the plasmonics field [31].

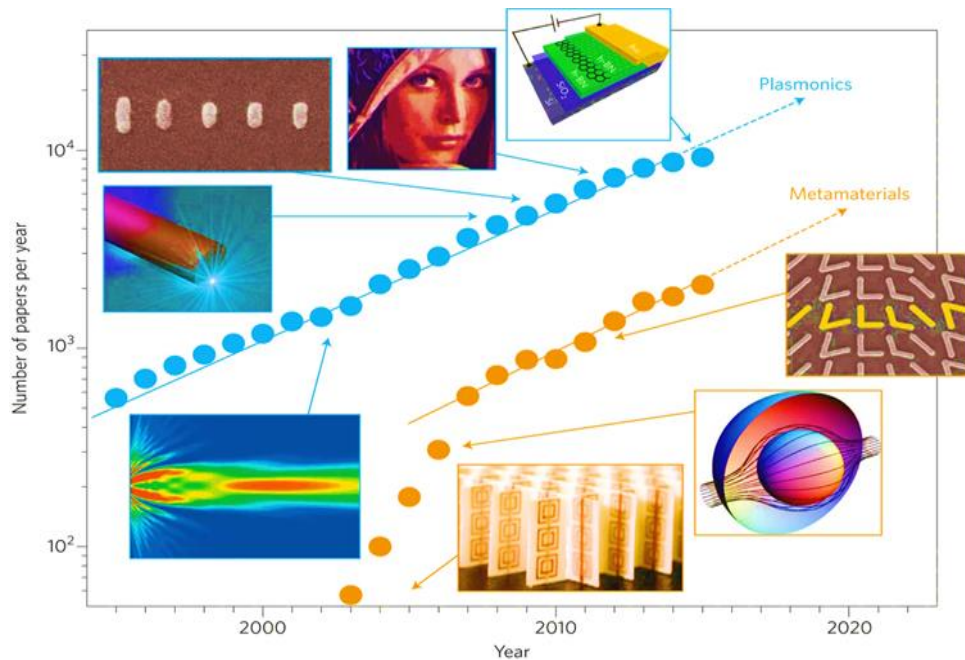


Figure 1.2. Number of articles published annually in the domains of plasmonics (blue) and metamaterials (yellow). Interior shots display significant landmark publications. Figure adapted [31].

Plasmonic MNPs have many applications in biology, medicine, and health with their excellent capabilities. Some of these high-tech applications are actively being used in the medical industry. The primary approach to utilize these properties in sensing is to exploit changes in the plasmonic response due to alterations in the local environment (e.g., refractive index changes) to detect minute quantities of molecules or particles. Applications range from medical diagnostics to environmental monitoring like attenuated total reflection (ATR). In ATR, reflection dips are observed due to the coupling of evanescent field to Surface Plasmon Polaritons (SPP) at a specific angle on a metallic interface [32], [33]. ATR uses the fact that the

plasmonic response is highly dependent on surrounding media. This dependence enables the detection of targeted molecules in a liquid sample by utilizing agents to bind them on a thin metal surface. A schematic for such a detection setup is shown in Figure 1.3. The graph on the right shows the reflection by angle of incidence. A sharp plasmonic dip occurs at the specific angle where SPPs are excited on the thin metal interface. When the refractive index surrounding media changes slightly, a significant reflection dip angle shift occurs, enabling the detection of the targeted molecule [34], [35].

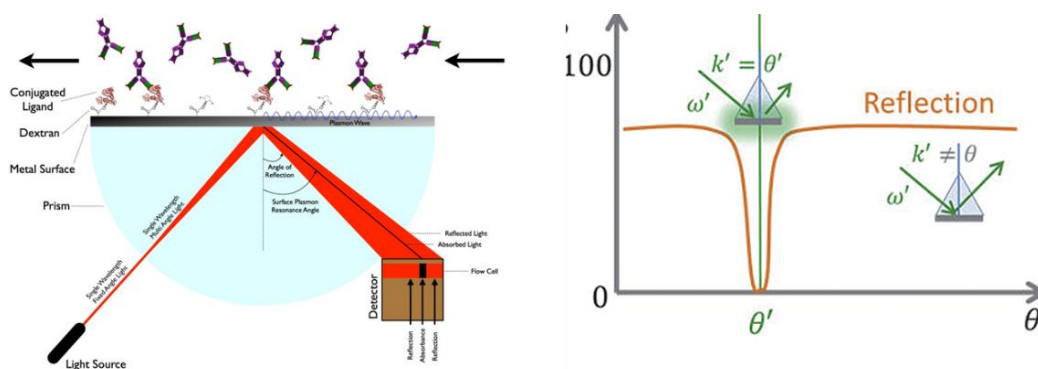


Figure 1.3. A schematic setup for molecule detection by SPP excitation. Adapted from [34]

Plasmonics enable the detection and quantification of biomolecules with exceptional precision and sensitivity. This capability finds crucial applications in disease diagnosis, real-time monitoring of biological processes, and the development of state-of-the-art testing devices [36]. Additionally, plasmonic nanoparticles are essential for targeted medicine delivery. Their unique ability to enhance the local electromagnetic field makes it possible to precisely regulate how therapeutic agents are released within the body, reducing adverse effects and increasing the effectiveness of treatment [37], [38]. Furthermore, plasmonics has revolutionized photothermal therapy. Here, nanoparticles are selectively heated by laser light, destroying cancer cells while sparing healthy tissue. This approach holds promise for non-invasive and highly targeted cancer treatments [39], [40]. Plasmonics has

found its place in optogenetics, a revolutionary technique for controlling neural activity using light. Plasmonic nano-antennas enhance the efficiency of photovoltaic devices in optogenetics, facilitating precise manipulation of neural circuits [41], [42].

Plasmonic nanostructures enable the development of super-resolution optical imaging techniques. 2014 Nobel Prize in Chemistry is awarded for exceptional work in developing super-resolved fluorescence microscopy [43]. Plasmonic enhancement to fluorescence contributes to the development of similar super-resolution imaging techniques [44], [45]. Plasmonic structures also contributed to super-resolution optical imaging techniques like structured illumination microscopy (SIM) [46], [47] and stimulated emission depletion microscopy (STED) [48], [49]. These methods break the diffraction limit and allow for imaging structures well below the wavelength of light [50].

Sub-wavelength plasmonic metal structures can be used to develop optical components such as lenses [51] and beam splitters [52] by utilizing collective far-field manipulation properties. These components enable precise control and manipulation of light, leading to better-performing, nano-enhanced optical components. Such devices usually called metamaterials, which are artificially engineered materials with properties not found in nature. Precise nano-engineering of the size, shape, and arrangement of sub-wavelength metallic features enables the control of far-field optical response. The field of metamaterials covers a broader range of light spectrum than the field of plasmonics currently covers. Researchers can craft metamaterials with super lensing properties, negative refractive indices, optical cloaking capabilities, and other fine-engineered optical properties by designing sub-wavelength metallic unit cells. This engineering allows for the creation of materials with custom-tailored optical properties. [29], [28], [53].

Quantum plasmonics studies quantum properties of light-matter interaction at nanoscale [54]. One of the areas of interest is quantum-plasmonic sensing. By leveraging the quantum properties of plasmons, researchers can achieve ultrasensitive detection of chemical and biological molecules [55], [56].

Furthermore, quantum plasmonics offers promising avenues for quantum computing and information processing. When coupled with quantum bits or qubits, plasmonic nanostructures can serve as the building blocks for single photon sources for quantum logic gates and quantum networks [57], [58]. This potential could revolutionize computing and secure communication systems [59].

Researchers continually push the boundaries of what is possible, creating innovative devices and technologies that impact various fields. The topic of using sub-wavelength metallic structures for optical products is a frontier where scientific curiosity converges with technological advancement.

1.2.1 Nanofabrication

Over the last century, nanofabrication has dramatically improved with the numerous applications of nanotechnology. The integrated circuit (IC) industry and microelectronic devices (MEMS) research and development are the main driving fields. Manufacturing processes have been getting better and better in resolution every year for over 50 years. Moore made one of the early predictions regarding the forthcoming advancements in transistor technology and was published in Electronics magazine in April 1965 [60]. In his research, Moore predicted that production costs would be halved and that the number of transistors in a chip of the same size would double yearly. This prediction is referred to as a "law" in subsequent years by Carver Mead, a professor at Caltech [61], [62]. Over the years, many scientists have argued if *Moore's Law* will eventually fail and discussed its implications. Ultimately, *Moore's Law* is materialized as “a *prophecy that came true*” [63]–[67].

One driving charge towards developing advanced nanofabrication methods is the recent evolution of plasmonic technologies, which takes advantage of some of the already optimized nanofabrication techniques that the IC and MEMS industry developed. Commercial computer processors are now being produced with ~5 nm resolution. Still, the methods for producing metal nanostructures over expansive

areas are restricted. Most of the methods bear drawbacks compared to others, such as high costs or the inability to accommodate nanostructure fabrication within all geometric configurations [68].

For Plasmonic research, the predominant technique adopted to produce various shapes of metal nanoparticles, such as cubes, stars, rods, and spheres, is chemical synthesis of nanostructures suspended in an aqueous suspension. This is because the reaction parameters, such as surfactants, temperature, and precursors, may be controlled independently [69]–[71]. While solution-based approaches can be scaled up, the significant variation in both the form and size of nanoparticles inside a single reaction vessel remains a challenge for accurate analysis. Furthermore, suspended metal particles can be organized on surfaces into two-dimensional (2D) and three-dimensional (3D) lattices using various methods. The interparticle distances and lattice geometry can be adjusted to manipulate the optical characteristics of these assemblies [72].

Surface nanofabrication techniques provide an alternate approach as they directly decorate surfaces with plasmonic nanostructures. Direct-write techniques, such as Direct Laser Writing (DLW), may be used to fabricate structures with resolutions limited by the diffraction limit of the laser wavelength [73], [74]. Electron-beam lithography (EBL) may be used to decorate substrates with MNPs with several nanometer resolutions limited by the motorized stage mechanics. EBL writing areas larger than a millimeter square area may take several days. Both methods can create 2D arrays of nanoparticles with varying distances between them [75], [76]. Scanning probe lithography (SPL) can even decorate surfaces with atoms reaching Angstrom scale resolution with very low throughput [77]. The predominant technique for creating hole and slot shapes in optically thick metal films is focused ion-beam (FIB) milling [13]. This technique has the capability to penetrate the film either whole or partially while also allowing for precise control over the size and arrangement of the structures, with an approximate accuracy of 100 nm. The production of multilayered metal films using focused ion beam milling and reactive ion etching is challenging

and time-consuming. However, these methods successfully created free-standing suspended films [78].

Methods employing the reproduction of structures from a pre-fabricated mask are the reason such structured devices, including microchips and MEMS devices, are accessible commercially. The most commonly used technique for pattern transfer is photolithography, where a pre-fabricated mask is used to selectively expose photoresist on the surface to transfer. The features are transferred to the underlying resist subsequent to the development process. Photolithography has emerged as a highly efficient and widely utilized technique in the production of commercial integrated circuits (ICs). This is primarily due to its ability to rapidly and conveniently structure numerous samples with almost the same features as those found on the employed photomask. The primary constraint of photolithography is the feature size, which is restricted by the diffraction limit of the light source. Standard UV photolithography commonly employs two types of light sources: visible g-line (with a wavelength of 436 nm) and UV i-line (with a wavelength of 365 nm). However, these light sources are limited in accurately reproducing sub-micrometer features. This constraint led to devices with shorter wavelengths. Deep ultraviolet (UV) lamps and lasers have been produced and are used to achieve smaller features, typically around 500 nanometers in size. Extreme UV lithography sources have a wavelength of approximately 13.5 nm, and X-ray sources have a wavelength of approximately 0.5 nm [79], [80]. Photolithography employing X-rays has the capability to accommodate smaller features compared to what can be achieved with Electron Beam Lithography (EBL) [81], [82].

Another widely used transfer-based lithography method is called nanoimprint lithography (NIL), also referred to as soft lithography. NIL is a technique used to transfer pre-fabricated patterns onto particular substrates. As a contact transfer method, the constraints imposed by the diffraction limit of light, which can limit the capabilities of photolithography, are not a concern in nanoimprint lithography. NIL operates analogous to traditional typewriters; wherein pre-fabricated letter stamps are utilized to transfer inked letters onto paper. There are multiple methods available

for the transfer process in NIL. These methods include the transfer of molecules and stamping a heated polymer followed by cooling. The technology offers a significant increase in throughput and resolution at a comparatively lower cost when compared to short-wave photolithography [83]–[85].

A direct pattern generation technique, interference lithography utilizes the interference pattern resulting from the superposition of multiple laser beams to expose photoresist. This method can fabricate periodic structures. In order to produce patterns, a coherent laser beam is partitioned into several beams, which are subsequently enlarged to cover the entire surface to be decorated. Recombination of beams propagating at different angles at the surface produces an interference pattern due to the phase differential between them. This method is promising for fabrication of periodic nano-structures over large areas [86], [87]. Multiple exposures can be utilized for fabrication of wider spectrum of structure geometries [88].

In addition to direct-write and transfer techniques, self-assembly methods are often employed for large-area surface decoration with somewhat lower fabrication controllability but incredibly higher throughput compared to direct-write methods. Such methods decorate surfaces with metal nano-structures fabricated in an aqueous suspension directly onto surfaces. This approach found many applications in plasmonic detection, such as the fabrication of SERS substrates. Another lithographic approach involves the use of highly monodispersed colloidal spheres, commonly referred to as colloidal lithography or nanosphere lithography (NSL). The significance of NSL in nanotechnology has been recognized in many applications [89]. Colloidal spheres may have a diameter that spans several micrometers to several nanometers, which is beyond the resolution limit of traditional lithographic techniques. Under the right circumstances, these colloidal spheres can self-assemble into two- and three-dimensional colloidal crystals. The first proposal using a self-assembled PS monolayer as a mask for a lithographic approach was in 1981 and later upscaled to cover a significant surface area for patterning [90], [91]. The field has witnessed significant progress, leading to a broader range of viable methodologies. The progress in synthesis techniques has facilitated the production of densely packed

particles with diverse forms and from various materials, employing a high degree of size and shape uniformity in a cost-effective manner. NSL has been identified as a rapid and cost-efficient method for the production of nanoscale devices. In one of the early works NSL used with photolithography, in which silica spheres with a diameter of 1 μm were employed as micro-lenses to expose the photoresist layer. Through numerical analysis, it was calculated that the focal point's size was approximately 150 nm [92].

In one of the pioneering studies of NSL, researchers used the openings in the hexagonal nanosphere monolayer as evaporations masks. The gaps between consecutive spheres were utilized in conjunction with polar and azimuthal angled deposition. [93]. In another study, detailed and systematic investigations were conducted on the periodic fabrication of complex nanostructures using NSL. This group extensively examined the deposition shading parameters of nanospheres and successfully generated a wide range of nanostructures using. Nanostructures with complex geometries in hexagonal periodic structures produced using the shading features of nanosphere lithography are shown in Figure 1.4 [94].

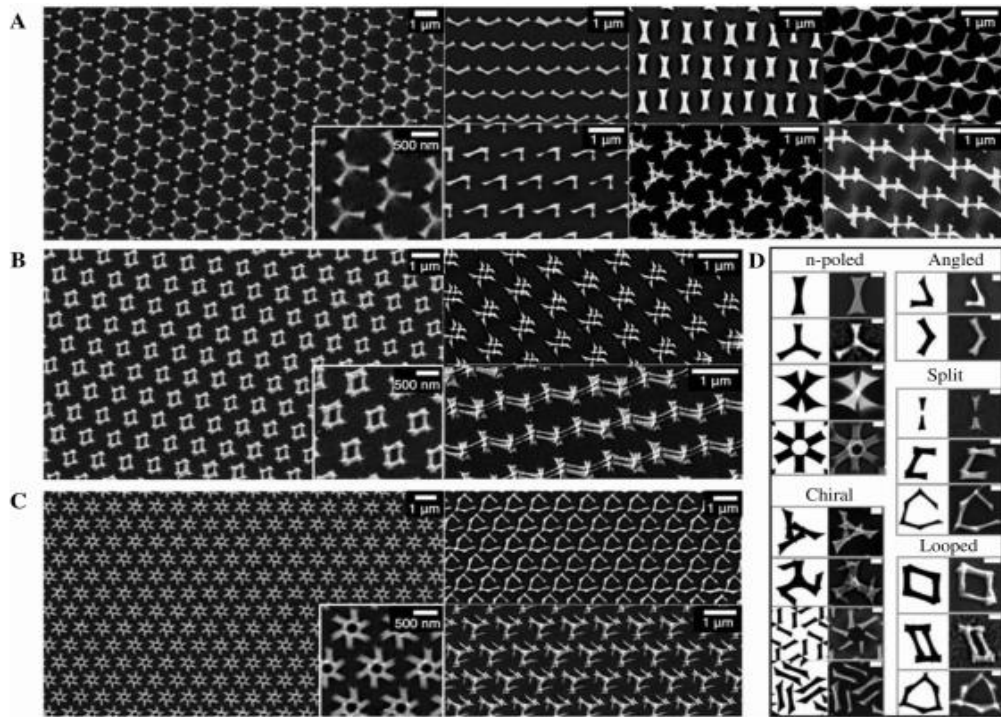


Figure 1.4. SEM images of nano geometries produced in a hexagonal array structure by evaporation of material from modified gaps between consecutive nanospheres by adjusting the polar and azimuth angles. Adapted from [94].

The foundation of the fabrication strategy of this thesis, hole mask colloidal lithography (HMCL), was introduced in 2007. In the paper various producible structures through this technique were discussed. The research team that invented the technique used a method of hole formation that involved spreading colloidal spheres at random on the substrate surface. The researchers detailed the hole-forming method for HMCL and made several fabrications at fixed-angle evaporation. They produced Ag pyramids by using the shrinkage of holes due to evaporation [95].

A 2012 article showed the broad spectrum of nanostructures that may be produced using motorized sample holders augmented by HMCL. Similarly, the technique of randomly coating colloidal spheres was used in this work to create holes. Structures fabricated with fixed angled multi-deposition are shown in Figure 1.5. The same group's subsequent efforts included the creation of Au nano helical structures using HML and analyzing their tunable infrared resonance [96].

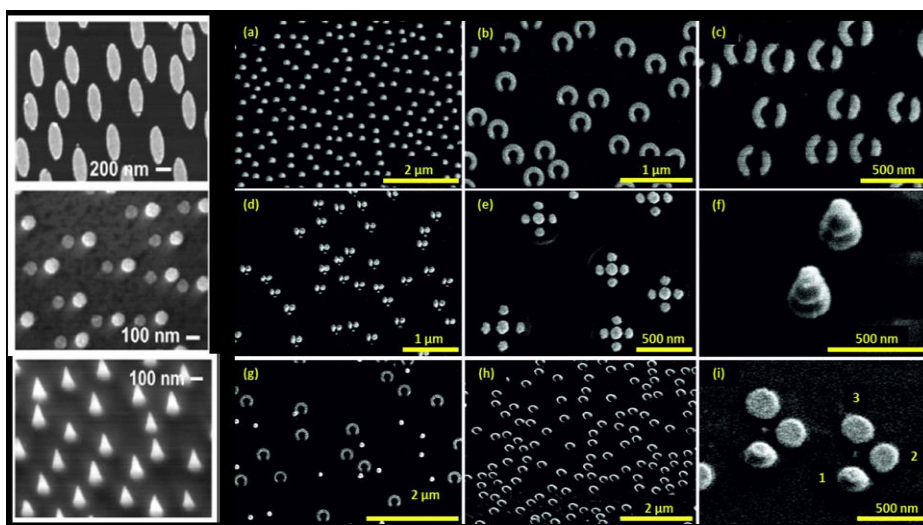


Figure 1.5. Right: Various metal structures produced using fixed-angle evaporation
 Left: Nanostructures fabricated using motorized sample holder-enhanced HML.

Adapted from [95] and [96].

The impact of various HMCL-produced geometries on Raman amplification was studied in a paper that explores the plasmonic resonance effects on SERS [97]. In this study, binary dimer, nano-funnel, and nano-cylinder structures were fabricated, and the effects of these structures on Raman enhancement were examined. After conducting the investigation, it was discovered that the HMCL method is the only method that can create the nano-funnel structures that yield the largest SERS enhancement in this work. The SERS measurements of this work are shown in Figure 1.6.

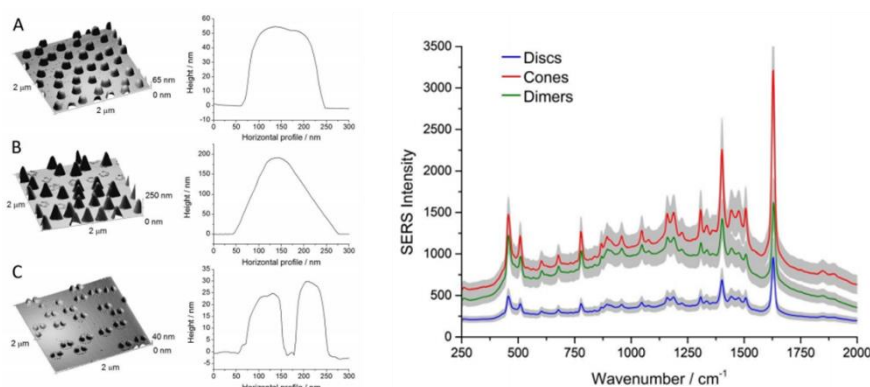


Figure 1.6. SERS measurements from HMCL fabricated substrates, adapted from [97]

In another work, inclined hole masks were fabricated, and dimer structures were evaporated using these holes. Due to the inclined hole-sample distance, dimer discs with varying interparticle distances were obtained on the same sample, enabling the investigation of scattering properties of various gap distances from a single fabrication. The researchers also fabricated semi-circle isolated ring resonators on the same sample, orienting their openings in different directions. They examined the polarization conversion properties of these structures [98], [99].

We can compare commonly used lithography techniques under four main criteria: area of applicability, resolution, geometrical variety, and cost. Many conventional methods are either too costly or not sufficiently facile to allow a wide variety of different geometries. Hole mask colloidal lithography, conversely, gets excellent grades under all of these four criteria. A comparison of conventional lithography methods and HMCL under these criteria is made in Table 1 [100]. Detailed explanations and further discussion about HMCL are given in section 3.1.

Table 1. Comparison of lithography methods in terms of area, resolution, variety and cost. Adapted from [100].

Lithography	Area	Resolution	Variety & Authenticity	Cost
Direct Laser Writing (DLW)	Moderate (mm's)	Sub μm	Very High (even 3D structuring possible)	Moderate
Electron Beam Lithography (EBL)	Low (Few Hundreds of μm 's)	several nm's	High	High
Focused Ion Beam Lithography (FIBL)	Low (Few Hundreds of μm 's)	several tens of nm's	High	High
Scanning Probe Lithography (SPL)	Very low (nm's to μm)	Molecular	Very High	High
UV&DUV Photolithography	Large (cm's)	$\geq 200\text{ nm}$	Limited (bound to other methods)	Low
Extreme UV Photolithography	Large (cm's)	Several tens of nm's	Limited (bound to other methods)	High
Nanoimprint Lithography	Large (cm's)	nm's	Limited (bound to other methods)	Low
Interference Lithography	Large (cm's)	100 nm	Moderate (only interference patterns of two or more beams)	Moderate
Colloidal Lithography	Very large (10s of cm's)	nm's	Low (only several geometries possible)	Very low
Hole Mask Colloidal Lithography	Very large (10s of cm's)	nm's	Very High	Very low

1.2.2 Computational Plasmonics

In order to investigate the dynamics of systems characterized by complicated mathematical models, the utilization of numerical simulations becomes essential. In nanophotonics, the Maxwell equations are rarely solved exactly despite their establishment. Gustav Mie [5] solved Maxwell's equations for the first time for nano-spheres. The plasmonic response of spherical and elliptical nanoparticles were calculated. Discrete Dipole Approximation (DDA) [101], [102] is used for the calculation of plasmonic response for a variety of geometries. In time, many numerical approaches have been established to simulate the physical behavior of more sophisticated nanophotonic systems that lack an analytical solution. Approximations for complicated problems are reliably obtained by discretizing the problem and solving it for every node in the time domain or the frequency domain. The electromagnetic finite difference time domain (FDTD) [103], [104]. The finite element method (FEM) [105], [106] and the boundary element method (BEM) [107]–[110] are commonly used in nanophotonics. With computers getting faster and faster, researchers can discretize either the volume or surface of the problem for either finite or infinite domains to approximate full Maxwell equations solutions for each discretized point in the problem domain or surface. The computational memory and time needed vary depending on the specific problem and the chosen methodology for its solution [111], [112]. Still, however, larger problems tend to be very computationally demanding; thus, researchers frequently use simplification models like dimension reduction by keeping the problem symmetric on one axis or mirror methods for problems with symmetries. Some problems may be simplified by using problem-specific analogies, such as the RLC circuit approach for frequency-selective surfaces [113], [114]. Such approaches generally extract information on a more specific case rather than a complete solution approximation of Maxwell equations but use minimal computational resources [115]–[118].

In recent years, computational plasmonics has made significant progress, particularly in transitioning from classical electrodynamics to approaches

incorporating quantum effects. A 2022 review of the advances summarizes some of these developments [119]. Most modern research focuses on finding models for incorporating classical electrodynamics with quantum phenomena [120]–[126], atomistic effects [127]–[132], creating techniques to handle strong coupling [133]–[137] and cavity phenomena [138]–[141].

Some of the recent developments in quantum-classical incorporation models are summarized in this paragraph. In a research paper, researchers developed a quantum-corrected model incorporating quantum effects into classical equations with excellent agreement to dependent density functional theory (TDDFT) based, fully quantum mechanical calculations [120]. Researchers developed a self-consistent hydrodynamic model that allows for the determination of the parameters of the ground state and the excited state of an electron gas. This method enables size-dependent surface resonance shifts of Na and Ag nanowires and nanospheres [126]. The projected dipole model accurately incorporates quantum plasmonic features of nonlocal response and a finite work function with the same level of accuracy as TDDFT to any system size that can be effectively analyzed within classical electrodynamics. When researchers applied the theory to dimers, they discovered that there are quantum corrections to the hybridization as long as the gap size is smaller than one nanometer [142]. In another work, researchers have introduced an atomistic electrodynamics model to accurately describe the optical characteristics of silver clusters with sizes ranging from 1 to 5 nm. The model comprises atom-type capacitances and polarizabilities that interact with each other to collectively describe the overall response of the nanoclusters [127].

The MNPBEM toolbox, used for most of the numerical calculations in this thesis, is designed for the computational modeling of metallic nanoparticles (MNP) through the utilization of a boundary element technique (BEM) approach. The solution to Maxwell's equations when dielectrics of arbitrary shapes are present can be mathematically described using surface-integral equations at the interfaces. The calculation is performed by considering the boundary charges and currents that are derived in a self-consistent manner [108]. The primary objective of the toolbox is to

provide a solution for Maxwell's equations inside a dielectric environment, specifically in cases where bodies with uniform and isotropic dielectric properties are separated by sudden interfaces [143]–[145].

1.2.3 Surface Enhanced Raman Scattering (SERS)

One of the most published branches of plasmonic field enhancement is Surface-enhanced Raman scattering (SERS). SERS, a pivotal technology in analytical chemistry and material science, has introduced an essential method for molecular detection. Raman scattering includes molecular fingerprint information, which can be used to determine the contents of an analyte at the molecular level, which may not be possible with other molecular analysis methods. The main bottleneck of Raman scattering is incredibly low signal levels, as the cross-section of the scattering event is typically in the order of 10^{-28} to 10^{-30} $\text{cm}^2 \text{ molecule}^{-1} \text{ steradian}^{-1}$ [146]. Which roughly corresponds to only 1 of 10^8 photons spontaneously Raman scatters [147]. Plasmonic near-field enhancement can significantly increase the Raman scattering probability when the Raman molecule is in the vicinity, this attracted researchers to develop more efficient surfaces for enhanced Raman scattering [148], [149]. By harnessing a significant enhancement in signal amplification that occurs during the interaction between molecules and metallic nanostructures, surface-enhanced Raman spectroscopy (SERS) exhibits unique sensitivity, allowing the detection of even single molecules. The uses of this technology encompass a broad range, extending from the identification of minute chemical elements within a small amount of analyte. SERS offers insights into molecular structures, vibrational modes, and chemical compositions, making it an indispensable tool for chemists studying complex reactions and intricate chemical environments.

Raman scattering, defined as the inelastic scattering of light by either exciting (Stokes) or absorbing (anti-Stokes) molecular vibrational energy, was discovered by C.V. Raman in 1928. Raman observed that light scattering by molecules yielded two distinct types of scattered light. The first type, known as Rayleigh scattering, exhibits

the same energy as the incident light. The second type, constituting a tiny fraction of the scattered light, has a different frequency. This discrepancy in energy was attributed to the inelastic scattering of light from the molecular vibrations. The schematic representation of the three types of scattering in relation with energy levels is shown in Figure 1.7. Raman received the Nobel Prize in Physics in 1930 in recognition of his significant discovery [150].

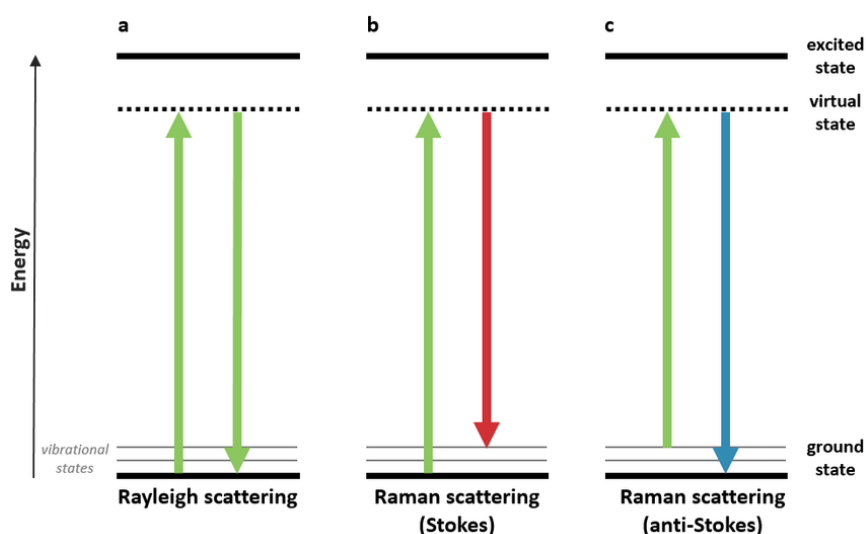


Figure 1.7. The three different types of electromagnetic light scattering.

In 1974, Fleischmann and colleagues made a discovery regarding the efficient Raman scattering of pyridine molecules when adsorbed on silver electrode surfaces. Their observations revealed a remarkable phenomenon: the Raman signal emitted from a roughened silver electrode was a staggering 10^5 to 10^6 times more intense than that of bulk pyridine [151]. This astounding enhancement did not go unnoticed, as both Jeanmaire and Creighton, in independent studies, corroborated these findings on roughened silver electrodes. Jeanmaire proposed an explanation using electric field enhancement mechanism, while Creighton suggested that the observed intensification is due to the interaction between the molecular electronic states of the pyridine molecule and the metal surface [152], [153]. This phenomenon, eventually

coined as Surface Enhanced Raman Scattering (SERS), marked a pivotal moment for molecular detection via spectroscopy techniques.

Since then, numerous enhancement mechanisms have been suggested to comprehend the underlying effects in the early stages of SERS. However, only two mechanisms, namely the electromagnetic (EM) model and the chemical enhancement (CE) model, are widely acknowledged and accepted today. The hypothesis of chemical enhancement (CE) relies on the chemical interaction between probe molecules and noble metals, and it is suggested to provide a maximum contribution of approximately 2-3 orders of magnitude [154]. The electromagnetic (EM) hypothesis is founded on the collective oscillation of free electrons, which gives rise to localized surface plasmons (LSPs). These LSPs have the potential to significantly amplify the EM field at or near the plasmonic resonance frequency [155].

Researchers and engineers have reported many SERS substrates over the years in order to amplify the Raman scattering signal. The variety of SERS substrates that reported in recent years is vast, making it difficult to review them comprehensively [156]. A schematic review of various SERS substrates proposed over the years is shown in Figure 1.8 [157]. The enhancement factor (EF) of SERS is commonly used as a metric to assess the performance of SERS substrates. The number of hot spots and field enhancement in these spots on the substrate determines the Raman EF for an analyte that will be adsorbed on these Raman surfaces before measurement. The initial documentation of self-assembled MNPs on solid substrates noted an enhancement factor (EF) of 10^5 [158]. Generally, the reported average EFs for surface MNP decoration by immobilizing suspended MNPs vary from 10^4 to 10^7 [159]–[162]. At the same time, there are occasional claims of more substantial EFs reaching up to 10^{10} [163].

Nevertheless, it is crucial to note that the estimation of EFs typically involves several approximations that may result in over or underestimations. Several researchers addressed this issue and worked on reliability of EF calculations and discussed common mistakes [164], [165].

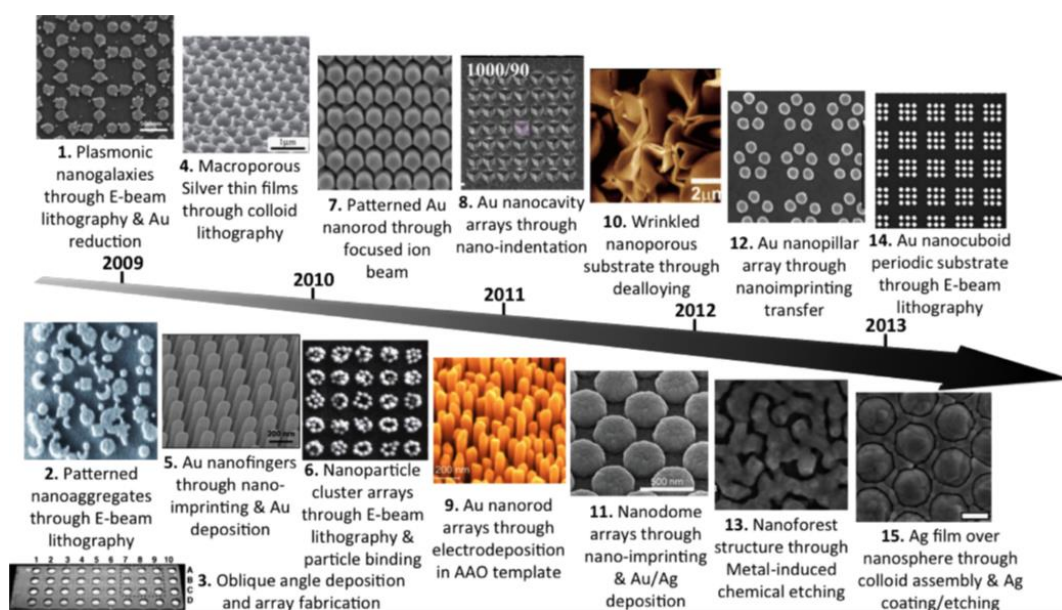


Figure 1.8. Images of various SERS substrates reported in literature, figure adapted from [157].

Raman spectroscopy is an established technique for detection and characterization today. SERS substrates are used for trace detection of explosives and chemical threats [166]–[168]. SERS is also used for the characterization of two-dimensional (2D) materials, such as graphene [169], [170], and transition metal dichalcogenides [171], [172], for the analysis of phonon modes in crystalline structures [173]. Raman spectroscopy can be employed to extract many properties for the study of materials, including but not limited to the number of monolayers [171], [174], in-plane anisotropy [175], doping type and concentration [176]–[178], crystal defects [179], [180], thermal conductivity [172], [181], [182], stress/strain [183]–[185], and phonon modes [146], [186]–[189].

In one of our group’s works, SERS substrates are prepared consisting of five different chemically synthesized gold nanoparticles with various surface features. The SERS enhancement properties are experimentally examined. Enhancement factors are numerically calculated by simulation. For this purpose, the structures are first 3D modeled by their SEM images, and then the electric field amplitude distribution around the surface is calculated using the considerations discussed in

this thesis in section 4.1. The SEM images, the 3D model used for computations and field distribution simulations, are shown in Figure 1.9 [190]. In another paper, simulations were conducted for closely spaced multi-spiked spheroids with complicated surface morphology and assembled as a close-packed monolayer. A maximum SERS enhancement factor of 8×10^9 is calculated with the plasmonic coupling. The surfaces show excellent SERS enhancements experimentally at the order of 10^7 [191]. With a similar approach, Ag spheroids with atomically flat surfaces are examined experimentally and numerically at another publication, with surface coverages as low as $\sim 1\%$. Field distribution shows strong enhancements at the edges of these flat-faceted structures [192].

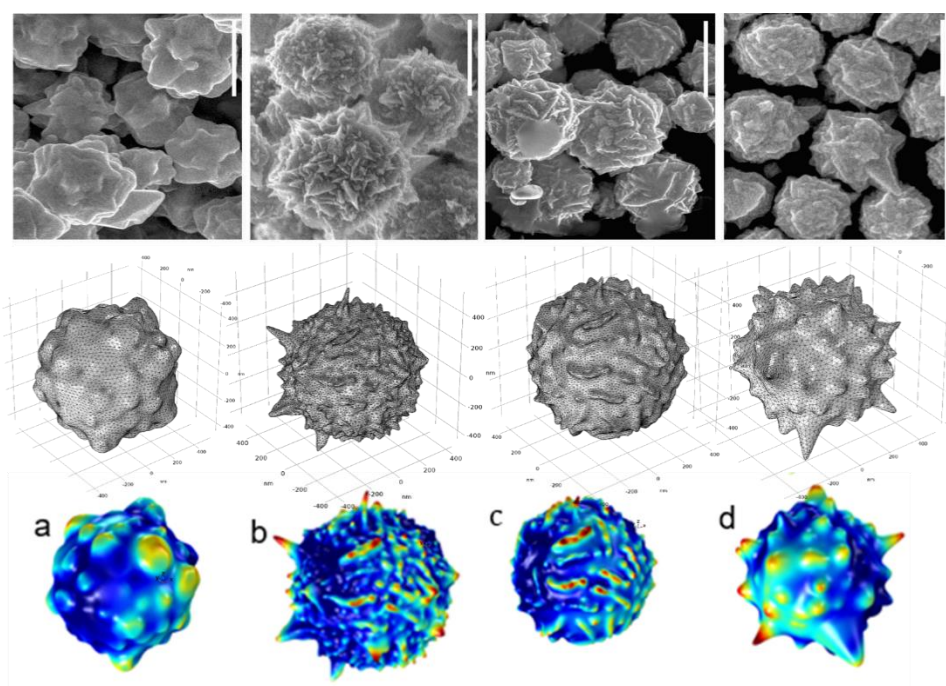


Figure 1.9. Up: SEM images of gold nanoparticles with four different surface morphology. Mid: 3D models based on SEM images. Down: Calculated field distributions. Adapted from [190].

1.2.4 Plasmon-Enhanced Solar Cells

Another important application of plasmonics is the use of plasmonic nanoparticles for photovoltaic devices. This idea has gathered the interest of numerous researchers over the years. Three distinct mechanisms can be employed for photovoltaic applications. These mechanisms are the scattering of light by metal particles, the augmentation of the electric field in the vicinity of the particles, and the direct creation of charge carriers within the semiconductor substrate. A schematic for solar cell enhancement mechanisms depicting the locations of metal nanoparticles in a PV junction is shown in Figure 1.10. The primary mechanism accounting for the observed enhancement in photocurrent for inorganic devices is attributed to scattering, whereas for organic devices, near-field enhancement is typically responsible [193]–[195]. Further discussion about photocurrent enhancement of photovoltaics by scattering from plasmonic nanostructures has been made in section 4.3.

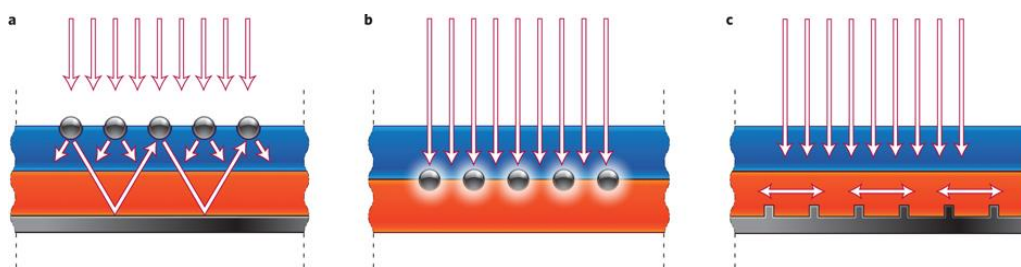


Figure 1.10. Three distinct mechanisms can be employed for plasmon-enhanced photovoltaic applications. Adapted from [194].

Plasmon-enhanced photocurrent in photovoltaics has been observed in various types of solar cells, such as c-Si [196], a-Si:H [197], GaAs [198], CdSe [199], InGaN/GaN [200], InP/InGaAsP [200], as well as organic semiconductors [201], [202], dye-sensitized solar cells [203] and perovskite solar cells [204].

In a paper published by our research group about spray coating of Ag nanocubes on conventional c-Si solar cells with thin passivation layers with thicknesses 8, 12, and 19 nm, a photovoltaic conversion efficiency increase of 3.5% to 6.4% was observed relative to uncoated case [196]. In the simulations, the scattering cross-section and angular distribution of scattering are calculated for the nano-cube with the considerations discussed in section 4.4.1 of this thesis. The ratio of scattering into the substrate to total scattering has been calculated and compared with a sphere of the same size; due to its flat sides, the cube is better at scattering the radiation toward the substrate.

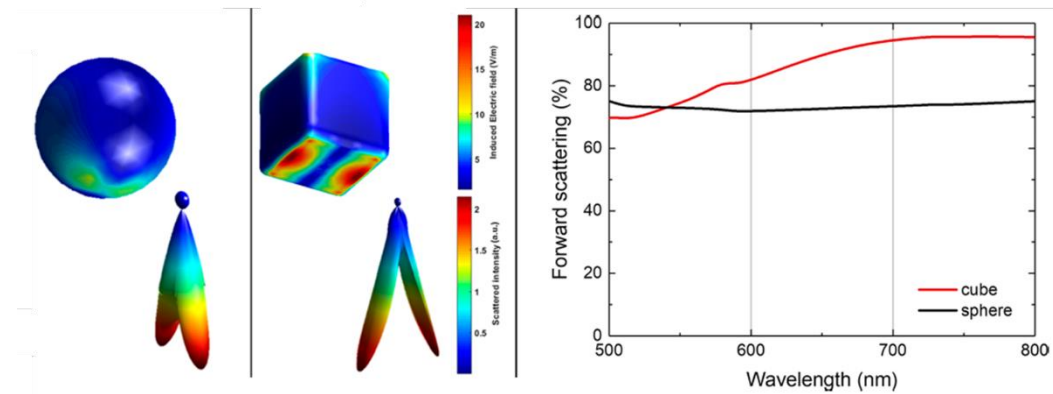


Figure 1.11. Simulation results for comparison of a 60nm side Ag cube with a sphere. Left: field enhancement and angular scattering distribution. Right: Spectral graph of forward scattering ratio. Adapted from [196].

CHAPTER 2

THE PLASMONIC INTERACTION

The complex and highly geometry dependent nature of the plasmonic response makes the prediction for a specific geometry and frequency extremely challenging. Analytical approaches able to solve and predict the response for relatively simpler geometries such as spheres. The groundwork of this response is first analytically worked out by Gustav Mie in 1908 [5]. Theoretical background leading these analytical solutions for this response outcomes are detailed in this chapter, starting from description of optical properties to complete solutions for spherical nanoparticles, where implications of these solutions are analyzed and discussed.

The theoretical foundations of plasmonic interactions are built upon classical electromagnetic theory. The interaction between metals and electromagnetic fields can be thoroughly comprehended using a classical framework based on Maxwell's equations. Even when examining metallic nanostructures at sizes as small as a few nanometers, the plasmonic behavior, depending on calculation outputs, can be adequately described without resorting to the principles of quantum mechanics [205]. However, quantum tunneling is important to incorporate when dealing with nano-aggregates, and nanojunction cannot be included in a classical model [206]. Even without quantum mechanical considerations, the investigation of metallic systems with complex geometries and their interaction with light at the nanoscale was a challenge before the development of numerical approaches enabled by computers.

This chapter aims to elucidate the core principles governing surface plasmons and explore their behavior. The scattering and absorption cross-sections are calculated for a sub-wavelength spherical particle, as previously done by Gustav Mie [5]. Detailed explanations of Mie theory can be found in the books by Stratton [207] and

by Born and Wolf [208]. The book by van de Hulst [209] gives a thorough summary of the studies done on the phenomenon of nanoparticle-induced light scattering throughout the first part of the 20th century. The results are discussed with simulations to grasp better the physical principles governing the plasmonic response.

2.1 Light Interaction with Metals

Prior to providing an elementary description of the optical characteristics of metals, it is necessary to revisit the fundamental equations that regulate the electromagnetic response, namely Maxwell's equations governing macroscopic electrodynamics, which are defined in the following form:

$$\begin{aligned}
 \vec{\nabla} \cdot \vec{D} &= \rho_{ext} \\
 \vec{\nabla} \cdot \vec{B} &= 0 \\
 \vec{\nabla} \times \vec{E} &= -\frac{\partial \vec{B}}{\partial t} \\
 \vec{\nabla} \times \vec{H} &= \vec{J}_{ext} + \frac{\partial \vec{D}}{\partial t}
 \end{aligned}
 \tag{2-1}$$

These equations connect the external charge and current densities (ρ_{ext} and \vec{J}_{ext}) with four macroscopic fields: the dielectric displacement \vec{D} , the electric field \vec{E} , the magnetic field \vec{H} , and the magnetic induction \vec{B} .

Polarization \vec{P} and magnetization \vec{M} are connected to the macroscopic fields with constitutive relations:

$$\begin{aligned}
 \vec{D} &= \epsilon_0 \vec{E} + \vec{P} \\
 \vec{H} &= \frac{1}{\mu_0} \vec{B} - \vec{M}
 \end{aligned}
 \tag{2-2}$$

Where, ϵ_0 is the electric permittivity and μ_0 is the magnetic permeability of free space. For nonmagnetic media used in this text, we can omit \vec{M} from our description. The polarization \vec{P} represents the electric dipole moment per unit volume within the material, resulting from the orientation of microscopic dipoles in response to the electric field and is zero in vacuum. The relationship between the internal charge density and the divergence of the polarization vector is expressed as $\vec{\nabla} \cdot \vec{P} = -\rho$. The principle of charge conservation, as expressed by the equation $\vec{\nabla} \cdot \vec{J} = -\frac{\partial \rho}{\partial t}$, reveals a connection between the internal charge and current densities. The current density can be written in terms of polarization as $\vec{J} = \frac{\partial \vec{P}}{\partial t}$.

For linear and isotropic media constitutive relations becomes:

$$\begin{aligned}\vec{D} &= \epsilon_0 \epsilon \vec{E} \\ \vec{B} &= \mu_0 \mu \vec{H}\end{aligned}\tag{2-3}$$

Where ϵ is relative permittivity, also known as the dielectric constant; and μ is magnetic permeability. $\mu = 0$ can be assumed for nonmagnetic materials. The polarization \vec{P} can be described linearly with \vec{E} using dielectric susceptibility $\chi = \epsilon - 1$ by:

$$\vec{P} = \epsilon_0 \chi \vec{E}\tag{2-4}$$

Another important relationship is between internal current density and the electric field, which are related by conductivity σ .

$$\vec{J} = \sigma \vec{E}\tag{2-5}$$

Until now the dispersive properties of metals have not been considered. For the case where all characteristic dimensions such as electron mean free path and lattice constant of the media are significantly smaller than wavelength wave-vector dependence can be ignored, the dielectric function only depends on frequency. The constitutive relations for electric field in equation (2-3) should be written as;

$$\vec{D}(\vec{k}, \omega) = \epsilon_0 \epsilon(\omega) \vec{E}(\vec{k}, \omega) \quad (2-6)$$

And equation (2-5) as;

$$\vec{J}(\vec{k}, \omega) = \sigma(\omega) \vec{E}(\vec{k}, \omega) \quad (2-7)$$

Combining the equations (2-2) and (2-7),

$$\epsilon(\omega) = 1 + \frac{i \sigma(\omega)}{\epsilon_0 \omega} \quad (2-8)$$

In this equation the existence of a close correlation between the variables $\epsilon(\omega)$ and $\sigma(\omega)$ is shown, both functions assume complex values. Electromagnetic properties of metals may be described with any of them. Generally, conductivity has been prioritized at low frequencies, whereas at higher frequencies typical explanations are conducted in terms of the dielectric constant.

2.1.1 Optical Constants

The material's response to light is represented by the complex refractive index $N = n + ik$, or equivalently by the complex dielectric function $\epsilon = \epsilon' + i\epsilon''$. While commonly known as optical "constants," those variables are not constant quantities with respect to wavelength of illumination. In fact, this dependence is more

significant for metals which makes resonance band quite narrow in plasmonic interactions.

The variables (n ; k) are primarily obtained with the direct measurement of transmission, reflection and attenuation, while (ϵ' , $i\epsilon''$) are a more convenient means of connecting to Maxwell's equations. The two expressions are completely identical and have a direct relationship with each other, as shown in equations (2-9).

$$\begin{aligned}\epsilon' &= n^2 - k^2 \\ \epsilon'' &= 2nk \\ n &= \sqrt{\frac{\sqrt{\epsilon'^2 + \epsilon''^2} + \epsilon'}{2}} \\ k &= \sqrt{\frac{\sqrt{\epsilon'^2 + \epsilon''^2} - \epsilon'}{2}}\end{aligned}\tag{ 2-9 }$$

Note that ϵ mentioned here is the relative dielectric function $\epsilon_r = \epsilon/\epsilon_0$, subscript removed for simplicity. Assuming that permittivity $\mu = \mu_0$ such that the material is not magnetic, the optical constants are related to material susceptibility as $\chi = \epsilon - 1$.

Generally, optical constants follow a parametrizable wavelength dependence; this property is called dispersion. Researchers found such parametrization is very useful for working with optical constants. The optical characteristics of most dielectric materials exhibit weak dispersion, meaning the refractive index remains slowly changing with respect to frequency, particularly within longer wavelengths of visible spectrum and near-infrared region. For dielectrics like SiO₂ Cauchy equation shown in equation (2-10) with three or more parameters can accurately represent wavelength dependence of refractive index in the visible region, while Sellmeier equation with three or more terms shown in (2-11) offers more accuracy in NIR region.

$$n(\lambda) = A + \frac{B}{\lambda^2} + \frac{C}{\lambda^4} + \dots$$

(2-10)

$$n^2(\lambda) = 1 + \frac{B_1 \lambda^2}{\lambda^2 - C_1} + \frac{B_2 \lambda^2}{\lambda^2 - C_2} + \frac{B_3 \lambda^2}{\lambda^2 - C_3} + \dots$$

(2-11)

The process of transforming values of $\epsilon(\omega)$ into a compact parametric model is intriguing and often necessary for simulations and analysis. In contrast to dielectric materials, the dielectric function of metals exhibits a significant variation depending on the wavelength. Depending on the frequency range of analysis, this parametrized model may be chosen as a polynomial fit for metals, which requires more orders thus more parameters to obtain better accuracy. Thus, it is more beneficial to utilize a physically motivated parameterization for metals, such as the Drude model, instead of an arbitrary model like a polynomial fit. The following section discusses the Drude model for the parametrization of metal-dielectric functions.

2.1.2 Optical Properties of Metals

The electron plasma model provides an explanation for the optical characteristics of metals within a specific frequency range. This approach is called the Drude model for the optical characteristics of metals. In the plasma model, an external electric field drives a gas of free electrons. As this model does not consider metallic transitions, it is thus not very accurate at higher frequencies; however, it plays a vital role in understanding the plasmonic response.

Electrons in the electron gas have an effective mass represented by “ m ”, according to model collisions that occur at a particular collision frequency denoted as “ γ ”. The equation of motion for an electron in a plasma, under the influence of an external electric field $E(t)$, equations of motions can be written as;

$$m\ddot{\vec{x}} + m\gamma\dot{\vec{x}} = -e\vec{E}(t) \quad (2-12)$$

Equation (2-12) can be solved when the driving field oscillates with frequency ω . $\vec{E}(t) = \vec{E}_0 e^{-i\omega t}$ as in the case of light. The solution becomes,

$$\vec{x}(t) = \frac{e}{m(\omega^2 + i\gamma\omega)} \vec{E}(t) \quad (2-13)$$

Now the polarization can be calculated by including the number density of the electron gas and charge

$$\vec{P}(t) = -\frac{ne^2}{m(\omega^2 + i\gamma\omega)} \vec{E}(t) \quad (2-14)$$

We can use equation (2-14) for linear isotropic media using the definition in equation (2-4);

$$\epsilon_0(\epsilon(\omega) - 1) = -\frac{ne^2}{m(\omega^2 + i\gamma\omega)} \quad (2-15)$$

The plasma frequency for metals is defined as;

$$\omega_p^2 = \frac{ne^2}{\epsilon_0 m} \quad (2-16)$$

Inserting equation (2-16) into equation (2-15), the dielectric function can be found as,

$$\epsilon(\omega) = 1 - \frac{\omega_p^2}{\omega^2 + i\gamma\omega} \quad (2-17)$$

We can separate real and imaginary parts,

$$\begin{aligned} \text{Re}[\epsilon(\omega)] &= 1 - \frac{\omega_p^2 \tau^2}{1 + \omega^2 \tau^2} \\ \text{Im}[\epsilon(\omega)] &= \frac{\omega_p^2 \tau}{\omega(1 + \omega^2 \tau^2)} \end{aligned} \quad (2-18)$$

Where, τ is the relaxation time or inverse of characteristic collision frequency. This result for metal dielectric function is known as Drude model for metal dielectric function.

At the excitation frequencies where $\omega > \omega_p$ the response is like of a dielectric material as the electron cloud plasma response is not enough to support frequencies above ω_p . Thus, the metal dielectric function models are only to be considered up to ω_p .

The single-oscillator Drude model can be enhanced in its generality by include the superposition of $j + 1$ separate oscillators. This model is called Lorentz-Drude multi-oscillator model.

$$\epsilon_{\text{Lorentz-Drude}}(\omega) = 1 - \frac{f_0 \omega_{p,0}^2}{\omega^2 + i\gamma_0 \omega} + \sum_{j=1}^{j_{\max}} \frac{f_j \omega_{p,j}^2}{\omega_j^2 - \omega^2 - i\gamma_j \omega} \quad (2-19)$$

Each term in the sum is characterized by four independent parameters: the oscillator strength (f_j), the damping rate (γ_j), the oscillator frequency (ω_j), and the plasma frequency (ω_p). The zeroth order or "Drude" term outside the sum is roughly the same, but with an oscillator frequency that is exactly equal to zero. This term refers to the contribution of unbound electrons that do not experience any restorative force when they are relocated. By utilizing the variable "j" with a maximum value of five, it is feasible to create a highly accurate representation of the measured optical characteristics for various metals and a wide range of semiconductors over the visible

spectrum. Typically, the free parameters in the multi-oscillator model mentioned above can be calculated using various nonlinear curve fitting procedures.

Free electrons largely determine the optical characteristics of some metals. Metals like aluminum (Al), sodium (Na), and potassium (K), can be accurately represented by solely utilizing the Drude model. The metals Ag and Au, which are significant for plasmonics, display a significant influence from bound electrons, in addition to their inherent behavior resulting from free electrons. The dielectric function's imaginary component exhibits a rise when photon energy triggers transitions between electronic bands. The transitions brought about by these photons are commonly referred to as interband transitions. Interband transitions at visible frequencies are observed in some metals, such as gold and copper, resulting in the absorption of specific frequencies and the manifestation of distinct colors of these metals.

2.2 Metals Under Illumination: Mie Theory

The subject of surface plasmons encompasses two primary interactions: surface plasmon polaritons (SPPs) and localized surface plasmons (LSPs), as noted before. SPPs, or surface plasmon polaritons, are electromagnetic waves propagating along the surface of metals at the interfaces between metal and dielectric materials. The waves can travel across the surface for distances ranging from tens to hundreds of micrometers but eventually diminish due to absorption in the metal and scattering via the dielectric medium Figure 2.1(a). Detailed information about SPPs may be found in Chapter 2 and 3 of Maier's book [205].

When a metal nanoparticle is subjected to an external oscillating field, its conduction band electrons move under the electromagnetic field, exciting the LSPs [210]. Particle polarization under an electromagnetic field is illustrated in Figure 2.1(b). A metal nanoparticle can be viewed as an electron resonator with a moderate level of damping depending on frequency and material. The enclosed surface of the metal nanoparticle applies restorative forces on the electrons propelled by the field, which

gives rise to resonance modes. The amplitude of resonant oscillation can far exceed the amplitude of excitation, resulting in a significant increase in the electromagnetic field near the particle and its extinction cross-section, which may be orders of magnitude higher than the actual projection area of the nanoparticle.

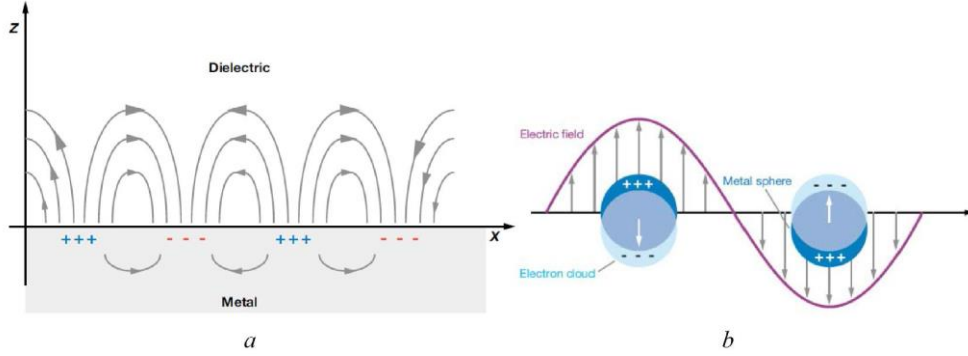


Figure 2.1. (a) Surface plasmon polaritons on a metal-dielectric interface. (b) Excitation of LSP by illumination of subwavelength MNPs.

An analytical solution is possible when a simpler case is considered. When the particle diameter is considerably shorter than wavelength of excitation field, at any instant the field distribution on the nano-particle is constant, called quasi-static approximation. This way, the time dependence term becomes independent of space of interest, such that it may be added to the equations later.

Let us consider a spherical MNP of diameter “a” embedded inside a dielectric medium, illuminated with a z axis polarized ($\vec{E} = E_0 \hat{z}$) monochromatic light of angular frequency ω . The Laplace’s equation can be solved to calculate the field inside and outside of the sphere.

Electric potential inside and outside of the sphere can be written as:

$$\Phi_{in}(r, \theta) = \sum_{l=0}^{\infty} A_l r^l P_l(\cos\theta)$$

$$\Phi_{out}(r, \theta) = \sum_{l=0}^{\infty} [B_l r^l + C_l r^{-(l+1)}] P_l(\cos\theta) \quad (2-20)$$

Where $P_l(\cos\theta)$ is the Legendre polynomials of order l , θ is the angle between position vector and the polarization axis. At the limit where $r \rightarrow \infty$, $\Phi_{out} \rightarrow -E_0 z = E_0 r \cos\theta$. Then $B_1 = -E_0$ and $B_l = 0$ for $l \neq 1$.

At the MNP interface ($r = a/2$) the boundary condition for tangential component of the electric field:

$$-\frac{1}{a} \frac{\partial \Phi_{in}}{\partial \theta} \Big|_{r=a/2} = -\epsilon_0 \epsilon_m \frac{\partial \Phi_{out}}{\partial \theta} \Big|_{r=a/2} \quad (2-21)$$

The boundary condition for the normal component of the electric field:

$$-\epsilon_0 \epsilon(\omega) \frac{\partial \Phi_{in}}{\partial r} \Big|_{r=a/2} = -\epsilon_0 \epsilon_m \frac{\partial \Phi_{out}}{\partial r} \Big|_{r=a/2} \quad (2-22)$$

Where the electric function of the surrounding medium be ϵ_m and the dielectric function of sphere be $\epsilon(\omega)$.

The boundary equations indicate $A_l = C_l = 0$ for $l \neq 1$.

Then the potential is evaluated as;

$$\Phi_{in} = -\frac{3\epsilon_m}{\epsilon(\omega) + 2\epsilon_m} E_0 r \cos\theta \quad (2-23)$$

$$\Phi_{out} = -E_0 r \cos\theta + \frac{\epsilon(\omega) - \epsilon_m}{\epsilon(\omega) + 2\epsilon_m} E_0 a^3 \frac{\cos\theta}{4 r^2} \quad (2-24)$$

for the inside (2-23) and outside (2-24) of the particle. These equations describe a superposition and a dipole placed at the center of the particle at the outside thus we can introduce a term to represent the dipole moment (\vec{p}), the equation then becomes;

$$\Phi_{out} = -E_0 r \cos\theta + \frac{\vec{p} \cdot \vec{r}}{4\pi\epsilon_0\epsilon_m r^3} \quad (2-25)$$

where;

$$\vec{p} = \vec{E}_0 4\pi\epsilon_0\epsilon_m a^3 \frac{\epsilon(\omega) - \epsilon_m}{\epsilon(\omega) + 2\epsilon_m} \quad (2-26)$$

Now that the polarizability (α) can be defined as a term in equation (2-26) can be defined in terms of particle size and material dielectric functions as shown in equation (2-28).

$$\vec{p} = \epsilon_0\epsilon_m \alpha \vec{E}_0 \quad (2-27)$$

$$\alpha = \frac{a^3 \epsilon_m (\epsilon(\omega) - \epsilon_m)}{8 \epsilon(\omega) + 2\epsilon_m} \quad (2-28)$$

When we examine the denominator in the limit, the polarizability peaks showing resonant behavior.

$$Re[\epsilon(\omega)] \rightarrow -2\epsilon_m \quad (2-29)$$

This outcome holds significant importance in understanding optical phenomena that originate from sub-wavelength metallic nanoparticles. The equation is possible when metals are surrounded by a dielectric medium. Au and Ag exhibit this resonance at the visible range [205]. Note that the resonance is generally satisfied in a considerably small band, with roughly around 20 nm bandwidth. This is due to strong dependence resonance condition to the dielectric function and highly dispersive nature of metals. The spectral band of the resonance is highly responsive to even very little changes in the surrounding dielectric function. Based on the Drude model, the resonance frequency undergoes a red shift when the dielectric constant of the surrounding medium increases.

2.2.1 EM Field in The Vicinity of MNP

Electric field can be evaluated by using the relation between electric field and electric potential $\vec{E} = -\vec{\nabla} \Phi$ in the equations (2-23) for the inside and (2-24) for the outside of a spherical particle.

$$\vec{E}_{in} = E_0 \frac{3\epsilon_m}{\epsilon(\omega) + 2\epsilon_m} (\cos\theta\hat{r} + \sin\theta\hat{\theta}) \quad (2-30)$$

$$\begin{aligned} \vec{E}_{out} &= E_0 + E_{ind} \\ &= E_0(\cos\theta\hat{r} + \sin\theta\hat{\theta}) + \frac{(\epsilon(\omega) - \epsilon_m)a^3}{\epsilon(\omega) + 2\epsilon_m} \frac{1}{8r^3} E_0(\cos\theta\hat{r} + \sin\theta\hat{\theta}) \end{aligned} \quad (2-31)$$

Where, E_0 is incident field and E_{ind} induced field. At near the surface, $a \rightarrow r$, equation (2-31) can be written as;

$$\vec{E}_{surface} \cong E_0(\cos\theta\hat{r} + \sin\theta\hat{\theta}) + \frac{(\epsilon(\omega) - \epsilon_m)}{\epsilon(\omega) + 2\epsilon_m} E_0(\cos\theta\hat{r} + \sin\theta\hat{\theta}) \quad (2-32)$$

The Equation (2-31) suggest that the field amplitude decays with the 3rd power of distance as the distance from the particle boundary increases linearly. We can observe this behavior via a relatively simpler simulation shown in Figure 2.2 for a 50 nm Ag nanosphere at 532 nm. In the graph induced electric field decay is shown by defining a line moving away from the surface of the sphere in the direction of light polarization.

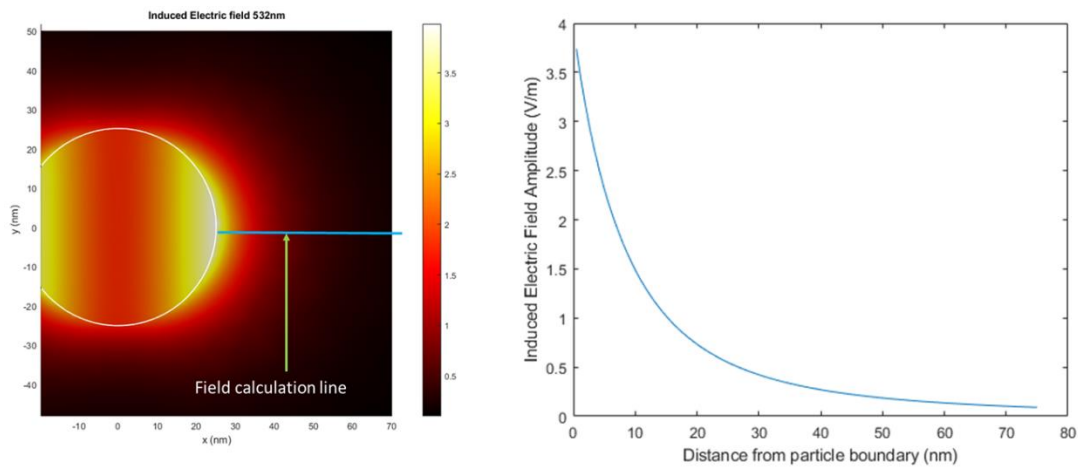


Figure 2.2. Electric field distribution calculation near a spherical Ag nanosphere when illuminated with 532nm, the graph shows the field decay on the field calculation line

The peak of near-field enhancement is apparent in equation (2-32). It is important to note that at resonance, where $Re[\epsilon(\omega)] \rightarrow -2\epsilon_m$, the field strength at the particle surface diverges to infinity, this is due to the limitation of classical approach. In reality, quantum effects start to dominate at around a few nanometers outside the particle, preventing this divergence. It can be said that in the quantum realm, the particle boundary is not so sharply terminated. This is also a consideration for classical numerical simulations for near-field enhancement, to determine realistically how far from the particle the field strength saturates. Quantum mechanics incorporated hydrodynamical models can accurately predict the EM fields' realistic behavior near the nanoparticles' boundaries.

2.2.2 Scattering and Absorption

The polarizability α , determined by equation (2-26) is used for calculation of the scattering and absorption cross-sections as:

$$C_{sca} = \frac{k^4}{6\pi} |\alpha|^2 = \frac{\pi}{24} k^4 a^6 \left| \frac{\epsilon(\omega) - \epsilon_m}{\epsilon(\omega) + 2\epsilon_m} \right|^2 \quad (2-33)$$

$$C_{abs} = k \text{Im}[\alpha] = \frac{\pi}{2} k a^3 \left[\frac{\epsilon(\omega) - \epsilon_m}{\epsilon(\omega) + 2\epsilon_m} \right] \quad (2-34)$$

Extinction cross-section is defined as the sum of scattering and absorption cross-sections, $C_{ext} = C_{sca} + C_{abs}$. C_{ext} emphasizes the total interaction cross-section of the nano particle.

It is important to note that the scattering cross-section in equation (2-33) is proportional to the sixth power of the sphere size, while the absorption cross-section in equation (2-34) is proportional to the third power. The rapid increase in the scattering cross-section can be seen in the simulations shown in Figure 2.3 for spherical Au particles with diameters increasing from 100nm to 150nm. The equations and simulations clearly show that, As the particle size gets bigger, the ratio of C_{sca}/C_{abs} increases rapidly, making the plasmonic particle a more efficient at scattering. Continuous lines in Figure 2.3 are scattering cross-sections, and dashed lines are absorption cross-sections. It can be observed that up to 120nm, the scattering cross-section is lower than absorption cross-sections; after a diameter of 130nm, the scattering overcomes absorption. In other words, for smaller sizes, absorption dominates the interaction, while as size increases, scattering becomes the dominant part of the interaction.

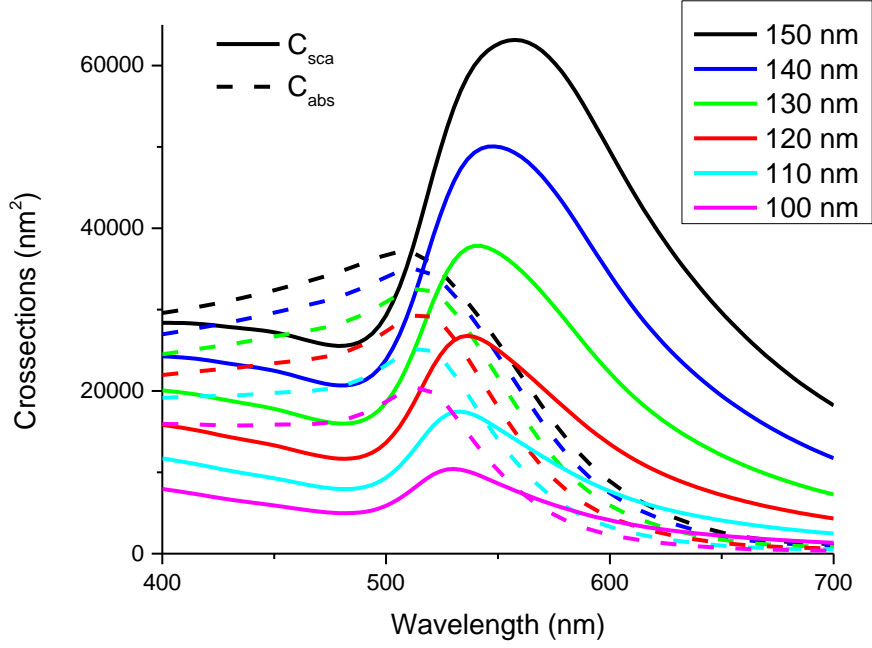


Figure 2.3. Scattering and absorption cross-sections calculated for Au spheres of increasing diameters

Cross-section results are sometimes given in terms of efficiencies, which is the cross-section divided by cross-sectional area of the nanoparticle, plugging into equations (2-33) and (2-34) we find the interaction efficiencies as:

$$Q_{sca} = \frac{C_{sca}}{A} = \frac{1}{6} k^4 a^4 \left| \frac{\epsilon(\omega) - \epsilon_m}{\epsilon(\omega) + 2\epsilon_m} \right|^2 \quad (2-35)$$

$$Q_{abs} = \frac{C_{abs}}{A} = 2ka \left[\frac{\epsilon(\omega) - \epsilon_m}{\epsilon(\omega) + 2\epsilon_m} \right] \quad (2-36)$$

Nanoparticles in close proximity to their resonant frequencies exhibit a significantly enhanced scattering and absorption efficiencies, which can reach values significantly above 1. Indicating the interaction cross-sections surpass their geometrical cross-sectional area which puzzled scientists in late 20th century [211]. This an important implication for applications where nanoparticles are used as scatterers, such as

photovoltaic applications. In calculations shown in Figure 2.4, dependence of Q_{sca} to Au sphere diameter has been calculated. For spheres smaller than 100nm the scattering efficiency stays below one even at resonance peak, diameters of 100 nm and above scatters light with efficiency more than one. For larger sizes scattering efficiency stays above one even at off-resonance spectral positions.

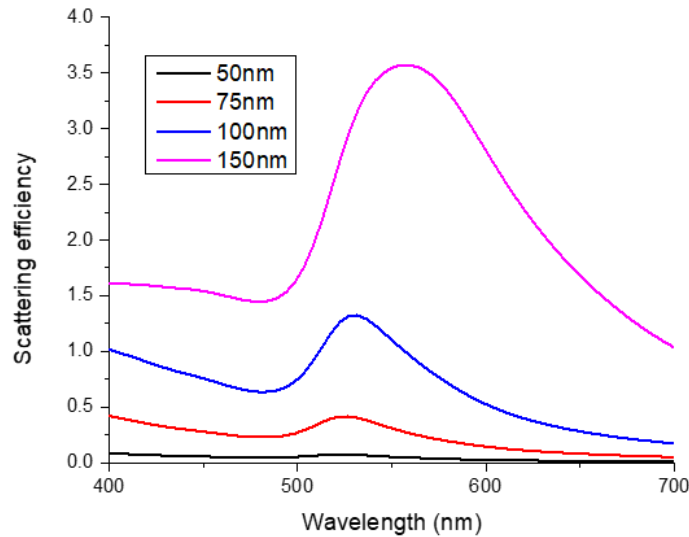


Figure 2.4. Spectral scattering efficiency calculated for different diameters of Au nano spheres

The trend of this fast increase of scattering efficiency with increasing particle size does not continue as the sizes get above 150 nm; the increase in scattering efficiency slows down. Higher-order resonance modes dominate the overall scattering response at these sizes. Calculations for an Au sphere with 150 to 600nm diameters are plotted in Figure 2.5. The figure shows that the scattering efficiency increases when the sphere diameter increases from 150 to 200nm. However, the relative difference in the peak height is much smaller than between 100nm and 150nm, as shown in Figure 2.4. Moreover, at 300nm diameter, the peak value is smaller than that for a 150nm diameter sphere. Increasing sphere size deforms plasmonic peak, leading a flatter but still strong response in a wider band.

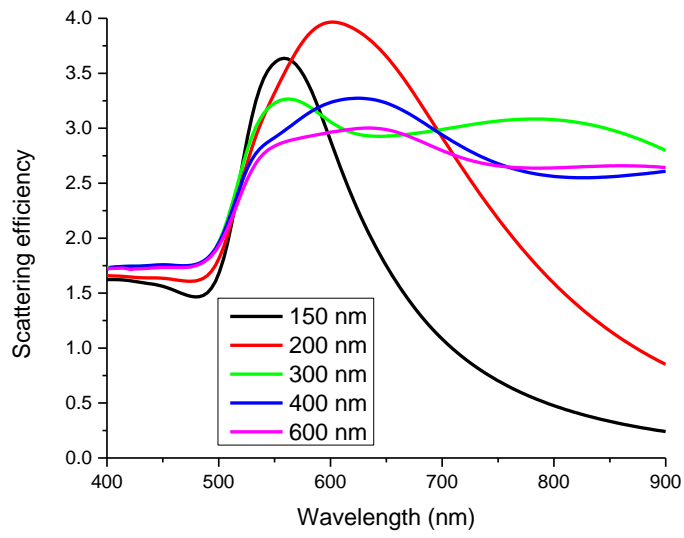


Figure 2.5. Spectral scattering efficiency calculated for large diameters of Au nanospheres

CHAPTER 3

METHODOLOGY

Fine-tuning the plasmonic response requires well-studied methods for nanostructure fabrication, reliable measurement methods, and computational modeling tools. The fabrication method used in this work is the hole mask colloidal lithography. HMCL is mainly chosen for its compatibility with large areas, geometry variation, and surface distribution variation possibilities. Scanning Electron Microscopy (SEM) is used as the primary tool for geometrical characterization, together with Atomic Force Microscopy (AFM) for specific requirements. Optical characterizations are made using dark field (DF) spectroscopy, which allows examination of scattering properties of plasmonic structures. 3D numerical simulations are done mainly using the BEM method, and for specific calculations and validations, the FEM method is used. Validation of numerical results is as important as the corrections and calibrations for experimental measurements.

This chapter explains the experimental methods for fabricating nano-structures and their optical characterization. Improvements done or proposed have been discussed. Numerical simulation methods, considerations, errors, and result validation approaches have been discussed.

3.1 Surface Nano-Structuring with Hole Mask Lithography

Nano-structuring methods for producing MNPs over large areas with precision are restricted. Some of these methods bear drawbacks, such as high costs or low throughputs when applied to large areas or the inability to accommodate more than a few sizes or shapes as discussed in CHAPTER 1. Hole Mask Lithography (HML) is a possible improvement to widely adopted surface nano-structuring methods. HML enables the economical fabrication of complex or straightforward nano-

structure geometries across large areas. Our aspiration revolves around developing an augmented HML technique, harnessing its considerable potential within nanofabrication and bringing it closer to its potential. It is expected that HML will accelerate empirical studies in the field of plasmonics, and it is expected to be used in the final application areas thanks to its wide area fabrication capability.

The idea of HML involves creating cavities in a sacrificial film using directional vapor deposition. The material is evaporated inside through these holes. This approach opens up opportunities to determine precisely where metal will be deposited under a hole in a sample placed at a certain distance from the surface. Various geometries can be produced by manipulating the angle during deposition. A visualization of deposition through the holes can be seen in Figure 3.1. The nanostructures formed on the sample surface below the holes are aligned according to the placement of the holes on the surface. Thus, the hole placement is essential for HML.

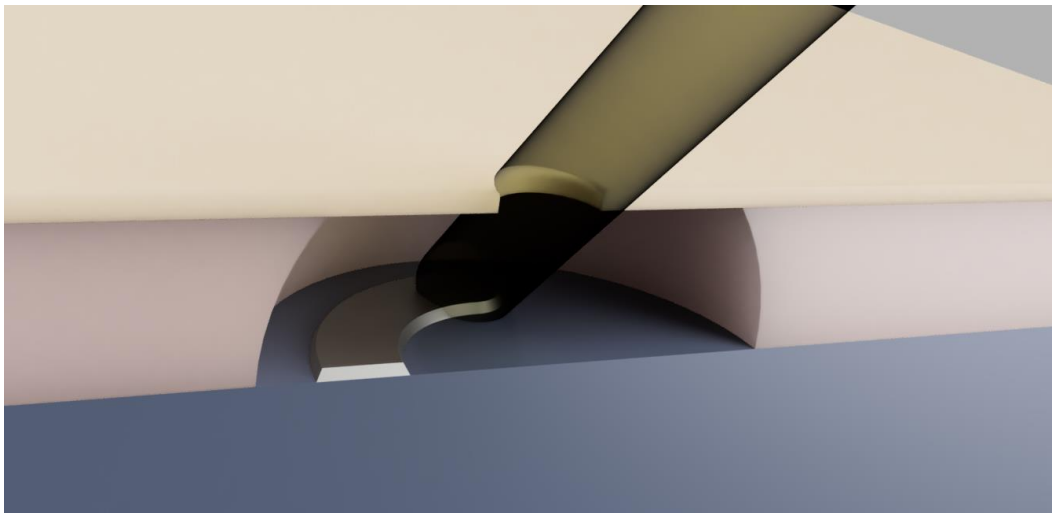


Figure 3.1. Visualization of directional material deposition through undercut holes in Hole Mask Lithography

HML employs specifically crafted hole arrays on the surface, enabling high-resolution capabilities and facilitating the production of structures in complex geometries. These holes can be fabricated using low-cost lithography techniques that allow large-area decoration, such as colloidal lithography. Fabricated hole mask allows complicated nanostructures to be parallelly produced across expansive surfaces, unlike direct writing methods like EBL, significantly increasing the throughput of fabrication. Although the fabrication method HML was called Hole Mask Colloidal Lithography (HMCL) when first introduced [95], we tried to keep the colloidal part optional since improvement opportunities will be proposed.

Nano-structuring with HML occurs by vapor deposition of material into holes positioned at a predetermined distance above the surface. The introduction of an angle between the normal vector of the substrate surface and the trajectory of the material traveling from the source to the sample within the thermal evaporation chamber makes the control possible. An illustration of deposition from a hole is shown in Figure 3.2. The angles from the surface normal in both perpendicular axes are used to determine precisely where the material will be deposited relative to the hole after passing through the hole. A crucial determinant of the method's accuracy is the directional nature of vapor deposition, wherein the vaporized material follows a linear path within the vacuum chamber after departing from the source.

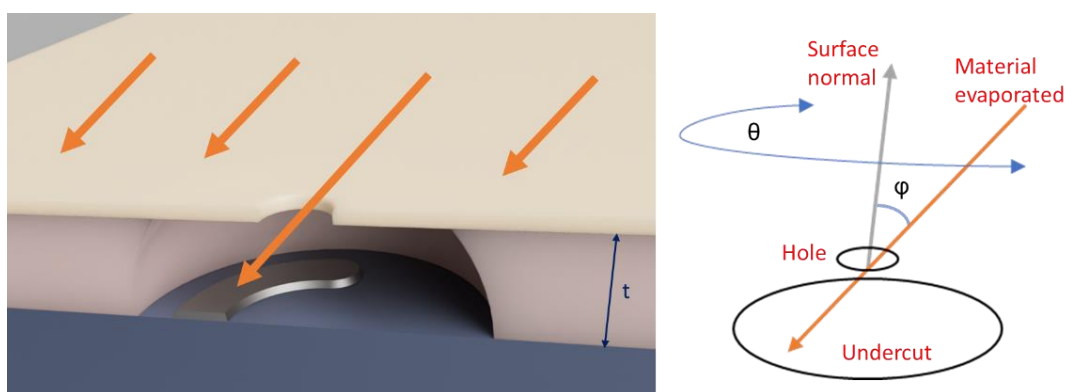


Figure 3.2. Hole mask lithography material deposition through the holes

During the material deposition, the angle imparted to the sample can be controlled using a motorized sample holder, ensuring precise alignment with the desired nanostructure formation on the sample surface. With simultaneous control over coating speed, this approach allows for the desired nanostructure to be deposited onto the sample surface with the intended thickness. A dual-motor sample holder enhances production diversity, enabling the rotation of the sample holder around two axes; an illustration of such a setup is shown in Figure 3.3 . With this system, the sample holder can be rotated around two axes, enabling heightened control over the area beneath the holes and maximizing the scope of producible structures. A split-ring resonator fabrication with continuous back-and-forth rotation with a fixed tilt angle is shown in Figure 3.4.

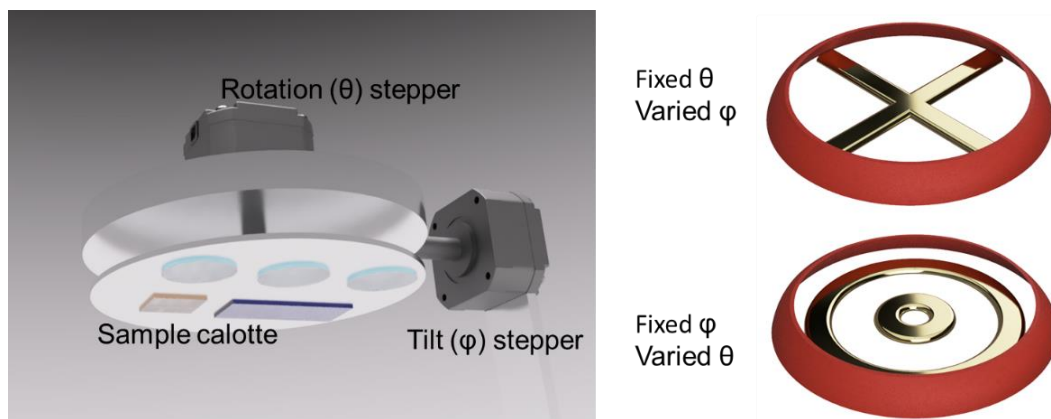


Figure 3.3. Left: An illustration of deposition chamber setup for achieving continuous control in undercut region. Right: Achievable geometries with material evaporation with varying only one angle.

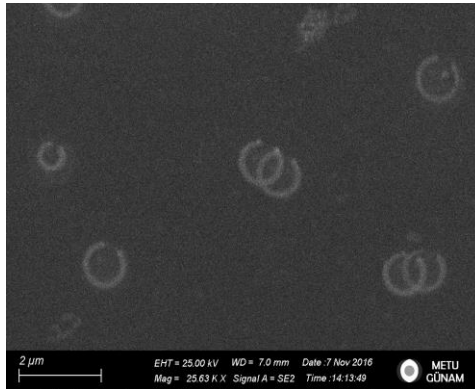


Figure 3.4. SEM image of split-ring resonators fabricated with continuous back and forward rotation at a fixed tilt angle

We will discuss several distinguishing characteristics of HML that make it unique compared to other micro and nanolithography methods.

First, the capacity to construct distinct areas of a structure with varied thicknesses provides control over the produced structure's third dimension. This thickness control makes an in-depth study of structural thicknesses and the characteristics of asymmetric structures possible, allowing for the construction of even more complex structures. A fabrication that takes advantage of variable thickness control is made by fabricating dimers with different thicknesses, as shown in Figure 3.5, where 750 nm diameter discs are evaporated at a fixed tilt angle with different thicknesses to fabricate asymmetrical dimers.

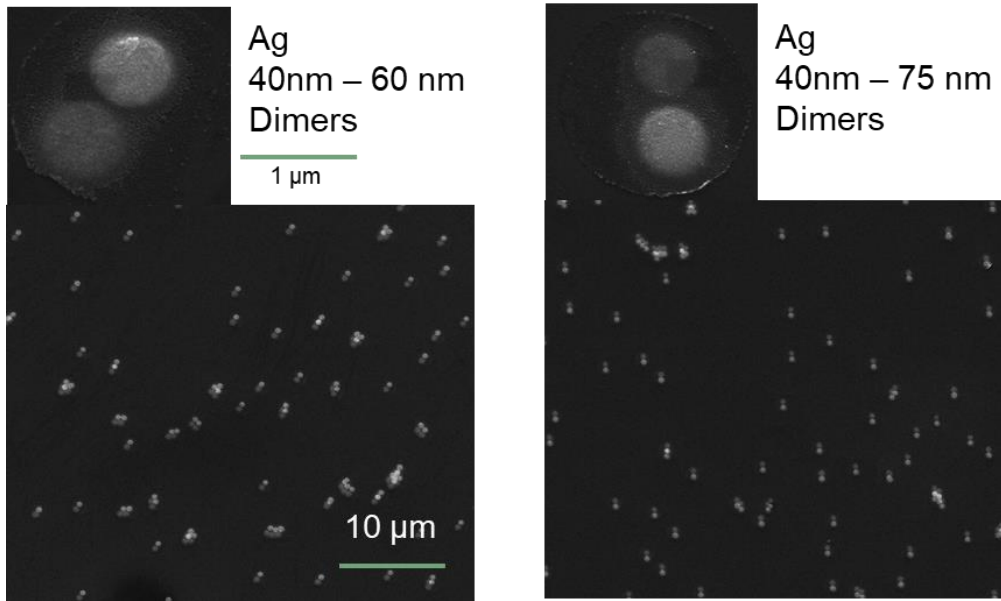


Figure 3.5. Fabricated asymmetrical Ag dimers on Si substrate with 40 – 60 nm and 40 – 75 nm thicknesses

Second, co-deposition of different materials is possible. One can use different materials in a single structure fabrication. This property can fabricate structures with different sections consisting of different materials. Figure 3.6 shows an SEM image of a multi-material dimer fabricated with asymmetrical thickness. This sample is fabricated by fixed tilt angle deposition of 40 nm of Ag after a 180-degree rotation and 20 nm of Au deposition. Multi-material compatibility can also be used for fabricating multilayer structures such as metal-dielectric-metal sandwiches.

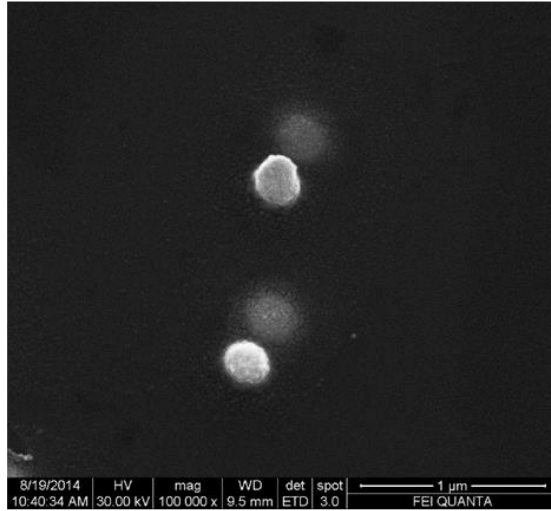


Figure 3.6. Multi-material dimer fabrication, 150nm hole diameter with 40 nm Ag and 20 nm Au deposition at fixed tilt angle.

Third, the phenomena of hole shrinkage during deposition enables the construction of structures with sub-hole-size resolution as the features get smaller as the material is evaporated through the holes. In our experiments, the hole shrinkage rate has been found as - 0.63 times the total thickness of deposition through the holes at a fixed 20° tilt angle. SEM images taken between 3 consecutive evaporations of Ag are shown in Figure 3.7. The value for hole shrinkage may be different for other tilt angles. The hole shrinkage should be considered for more complex deposition with continuous tilt and rotation for accurate prediction of resulting structures. Hole shrinkage can be seen as an advantage as it makes it possible to fabricate at a lower resolution than the hole size, or it can be a disadvantage as it limits the total amount of material to be deposited inside the undercut region. The walls of high aspect ratio structures are tapered due to this effect.

A highly asymmetrical dimer fabrication is shown in Figure 3.9; for this fabrication, 140 nm Ag is evaporated at a fixed azimuth angle from 175 nm holes, followed by a polar rotation of 180 degrees, and another deposition of 30nm is applied. The second disc turned out to be around 55 nm in diameter due to the hole shrinkage. Inset in the figure is a 3d model representing the fabricated asymmetrical dimer.

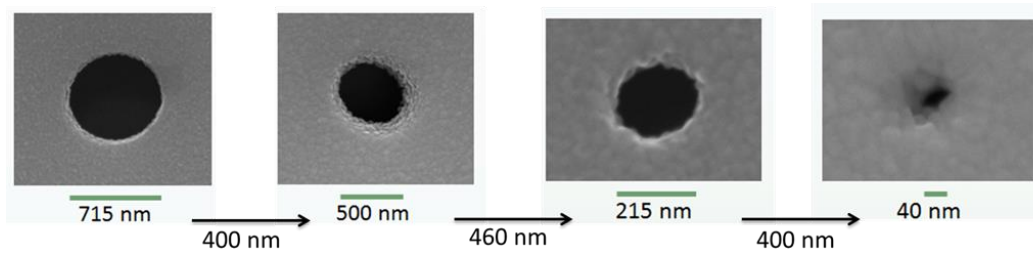


Figure 3.7. SEM images taken in between 3 consecutive evaporation of Ag at fixed 20° tilt angle showing hole shrinkage



Figure 3.8. SEM image of highly asymmetric Ag dimers fabricated by HMCL by utilization of hole shrinkage

3.1.1 Hole Mask Colloidal Lithography

Surface distribution and feature size of an HML fabrication solely depend on the hole decoration method used on the surface. Most of the research used colloidal lithography after HMCL was first introduced in 2007 by Fredriksson and teammates [95]. The reason is easy accessibility as colloidal polystyrene nanospheres can be purchased in various sizes from several nanometers to millimeters with very accurate size distribution. These products are both sold as a dry powder or as a suspension in aqueous form. Various sizes of PS and silica nanosphere suspensions are used in our studies.

The general procedure for sample preparation used by methods pioneers' work [95] is shown in Figure 3.9 and can be summarized briefly. First, a sacrificial layer is deposited on substrates to be nanostructured by spin-coating; PMMA was the choice for this layer in the literature. After a surface charge switching step by an appropriate poly-electrolyte, the nanosphere suspension is spread on this surface, layer kept for a particular time and then washed off, leaving isolated nanospheres adhered to the surface. Then, a thin (20-50 nm) Au layer is deposited on nanosphere-decorated PMMA prior to a mechanical nanosphere removal. With time and pressure-controlled oxygen plasma etching as the last step, the desired cavities under the mask layer are achieved for the actual structuring. SEM images taken after nanosphere decoration, nanosphere removal, and cavity formation are shown in Figure 3.10.

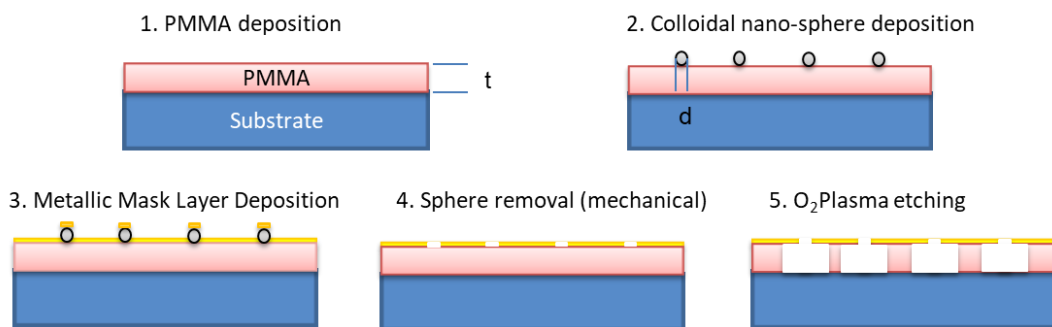


Figure 3.9. Sample preparation for HMCL, a schematic procedure

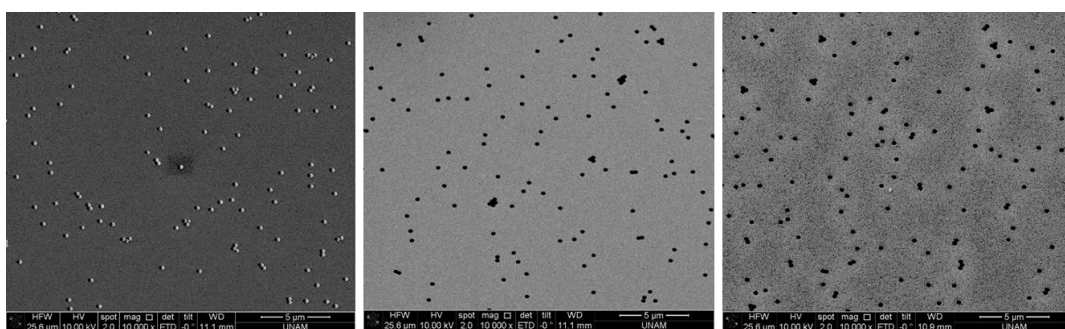


Figure 3.10. SEM images taken after hole mask preparation steps, nanosphere decoration, nanosphere removal and cavity formation from left to right.

In previous studies by our research group, an alternate method for sample preparation was proposed, and the original procedure was altered. It is shown that instead of PMMA, a photoresist layer can be used as a sacrificial layer, and instead of plasma etching for cavity formation, photolithography is an alternative. Using the Au top layer as an exposure mask for photolithography, the resist is over-exposed and over-developed for cavity formation. The method as proposed was successfully applied. However, wet undercutting by a photoresist developer is found to be more problematic due to excessive forces during development. These forces limit the size of the cavity as overlying mask layer. Oxygen plasma is so delicate because it erodes the polymer layer very gently and equally from each direction in a dry environment. Please refer to our previous work about an alternate procedure for HMCL and

detailed discussions about each step. Although the approaches are completely new, all the work explained in this section was developed based on our previous studies and discussions [100].

3.1.1.1 Hole Mask Formation Procedure

Finalized procedure for application of HMCL is detailed in this part. To ensure scientific integrity in our experiments optimizing the steps to a repeatable degree for Hole Mask fabrication, different procedures only applied for the parts that need to be tested. All prepared samples go through the same processing steps. Below is an explanation of the general process steps used to create the hole mask.

1. Substrate Cleaning and preparation: Substrates are cut to size roughly to 1 inch and are cleaned by 10-minute ultrasonic bath in deionized water, acetone, or isopropyl alcohol, respectively. If the substrate is made of Si, they kept in a 10% HF solution until complete hydrophobicity is observed. By taking this step, the Si surfaces become even more hydrophobic, which boosts photoresist adhesion. If the substrate is glass they are submerged for fifteen minutes in piranha solution (3:1; H₂SO₄: H₂O₂) to rid them of possible organic matter contaminations. Glass surfaces are treated with HDMS to get similar adhesion of PMMA. For this, we use Microchem's "MCC Primer 80/20" on glass substrate at datasheet procedure.

2. PMMA Coating: PMMA is spin-coated onto the clean substrates. Layer thickness is aimed to be roughly twice as thick as the hole diameter that is intended. This ratio provides adequate tilt angle resolution as we do not want to use excessive tilt angles to reach sidewalls of the cavity, as the amount of material to be evaporated increases at higher angles to obtain desired structure thickness. "950PMMA A7" resists by Microchem is used in our experiments together with "A thinner" specifically made for this resist. This resist concentration allows thickness control in the range of 1.5 μ m to 600 nm without thinning. When spin-coating the resist directly does not yield films thin enough, it is thinned by desired amount. The substrates are

coated in 45 seconds at the proper rotation speed, followed by a minute of annealing at 110° C.

3. Pre-plasma procedure: At this stage the surface of PMMA layer is highly hydrophobic which makes coating of polyelectrolyte and nanospheres impractical as both of these are aqueous. Exposing samples to oxygen plasma for roughly two minutes makes the PMMA surface hydrophilic enough without etching the layer too much.

4. Poly-electrode coating: Samples are submerged in a 0.2% by weight solution of poly (diallyldimethylammonium chloride) (PDDA) in deionized water. After that, rinse with deionized water and use N₂ to dry. The concentration of solution affects the surface coverage to some degree, higher concentration of PDDA solution yields better nanosphere adhesion. However, 0.2% is found to be near saturation and increasing this concentration more does not significantly increase the surface coverage. This value is kept constant and surface coverage is changed by increasing nanosphere suspension concentration in next step.

5. Nanosphere decoration: Using deionized water, the suspension of nanospheres is diluted for desired concentration. The diluted suspension is kept in ultrasonic bath for a duration of twenty minutes to separate some of the weakly agglomerated nanospheres in the suspension.

The concentration of nanospheres directly affect surface coverage and plays an important role for isolated surface decoration, a must for successful mask preparation. The values we found to be fitting for different diameters of nanospheres are; 0.125% by weight for 750 nm, 0.015% by weight for 500, 0.026% by weight for 250 nm, and 0.015% by weight for ~150 nm nanospheres. At this stage, the concentration rates can be adjusted to achieve the required surface occupancy. An SEM image after 500 nm nanosphere deposition is shown in Figure 3.10 left panel.

The surface is coated by dripping this suspension onto it until the whole surface is covered, wait 1 minute, and then rinse with deionized water followed by N₂ blow drying.

6. Mask layer coating: SiO₂ is sputtered with a thickness of about 30-50 nm on the sample surface. The resistance of mask layer to the PMMA etching step is crucial. In our trials Au, Cr and SiO is also examined as possible mask layer candidates, these experiments are discussed later in text.

7. Removal of nanospheres: After hole mask layer coating, nanospheres are physically removed with a 10-minute ultrasonic bath. After this step samples are examined visually and through microscopy, this is found to be enough for most cases. However, in some experiments depending on mask layer thickness and deposition directionality, ultrasonic bath may not remove all of the spheres. In these cases, a very gentle q-tip scrubbing is applied in di-water followed by N₂ blow drying.

10. Cavity formation: This step, samples undergo oxygen plasma etching to create cavities with the appropriate diameters at the bottom of the holes. The time required for this step depends on the PMMA thickness and plasma parameters. In our experiments the etch rate of PMMA is found to be around 10 nm/min by consecutive thickness measurements with a profilometer. The etching time is chosen to be 2 to 2.5 times the time it takes to completely remove an unmasked PMMA layer of the same thickness. This approach yielded cavities wide enough for use up to 30 degrees tilt angle.

Optimized colloidal surface decoration method yielding randomly placed ~150 nm holes on SiO₂ mask layer with about 1.2% to 1.8% surface coverage when used with 500 nm nanospheres, with an average around 1.5%. Figure 3.11 shows SEM image grain size and distribution results averaged from 3 different SEM images of the sample surface. Gwyddion is used for analysis of average disc size and surface coverage by using an contrast selective mask. The masked SEM image and size

distribution histogram is shown in Figure 3.11. For all experiments requiring size and coverage analysis the same method is used.

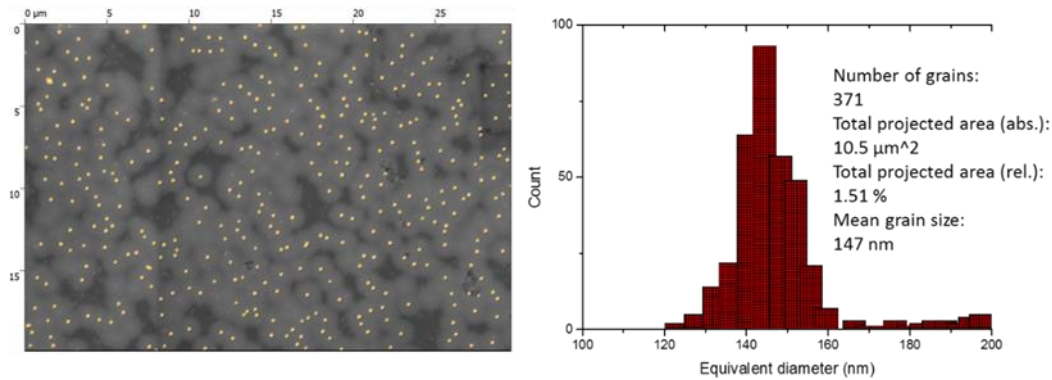


Figure 3.11. Left: SEM image of a surface decorated with holes masked for grain analysis. Right: Size distribution histogram with grain analysis results averaged from 3 SEM images

It is feasible to manipulate parameters like hole size and distribution up to some degree without significantly changing the decoration procedure. Over 1 μm undercuts have been observed on SEM images of fabricated structures. Based on 1.5% surface coverage of hole mask may yield up to 66% surface coverage of fabricated structures, by considering undercut with diameter 1 μm fully filled with material from each hole. In a more desirable case we can consider a structure covering an area of 10 holes yields 15% surface coverage which may be desirable for several practical applications like solar cell surface applications which will be discussed in section 4.3.

Complicated structures fabricated using HMCL with rotation of sample holder in azimuthal and/or polar directions simultaneously during material evaporation. For this purpose, an evaporation system with a sample holder similar to the one shown in Figure 3.3 is purchased from “Nanovak”. For enhanced control on motor movements an Arduino development board with CNC controller shield with 2 motor drivers have been utilized. A freeware firmware developed for Arduino called GRBL

is flashed to the development board. This allowed easy pre-programming of motor movements for desired nano-structure with the use of g-code files. Motor movements programmed for fast repeated movement during deposition. SEM images of three of these fabrications are shown in Figure 3.12. In all fabrication Ag is used as the main material as it is cheaper than Au, the other frequently used material for plasmonics.

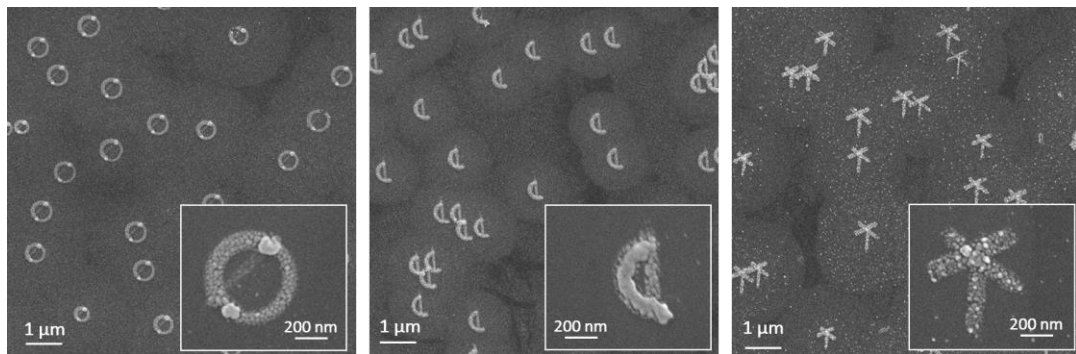


Figure 3.12. SEM images of fabricated structures with complicated geometrical aspects

Main purposes of these fabrications are:

- 1.) To observe the method is working properly, including repeatability of each device used in fabrication
- 2.) To understand dynamics of the method during production, and get a better understanding about which parameters are more important.
- 3.) To Examine structural properties of fabricated structures.
- 4.) To see how post annealing effects structural and optical properties.

Most of these purposes got some development in this fabrication series of complicated structures. To achieve this some parameters are not kept constant, adjusted some slightly between samples. Method has been shown to be able to fabricate complicated structures that show plasmonic activity. Further discussions and measurements conducted on these structures are detailed in section 4.2.

3.1.2 Hole Size Reduction

As one of the improvements to the hole mask fabrication discussed previously we explored the question “can the hole size be tuned without changing PS nanoparticle size?”. By achieving this the researchers would require a fewer suspension purchases in the experiments that require different hole sizes. Two methods proposed are oxygen plasma treatment of polystyrene (PS) nanospheres after nanosphere decoration and tilted rotating evaporation of mask layer.

Oxygen plasma size reduction experiments are shown in Figure 3.13, which shows SEM images of PMMA surface with reduced-sized particles after each consecutive oxygen plasma etching session applied on initially 500nm nanospheres. Sem images are analyzed in Gwyddion using an automatic mask. The average sphere area is measured, and the average diameter is obtained. 500nm PS nanospheres on the PMMA layer are etched with oxygen plasma for 0min, 5min, 10min, and 20min at 150W RF plasma power at 30mtorr pressure before SEM analysis, respectively. The average diameter of nanospheres in each case is found to be 500nm, 435nm, 395nm, and 255nm, respectively. The size reduction rate seems linear, with a slope of 12nm/min. Twenty minutes of etched spheres show deviation in size, and they lose their circular shape. Thus, this method is applicable for size reduction to about $2/3$ times the original particle diameter. Further size reduction may change the geometry and remove some spheres from their location, as seen in (d) in Figure 3.13. Note that in this size reduction step, the PMMA underlying the particles is also etched, so the primary thickness of the PMMA layer should be chosen considering the etch rate.

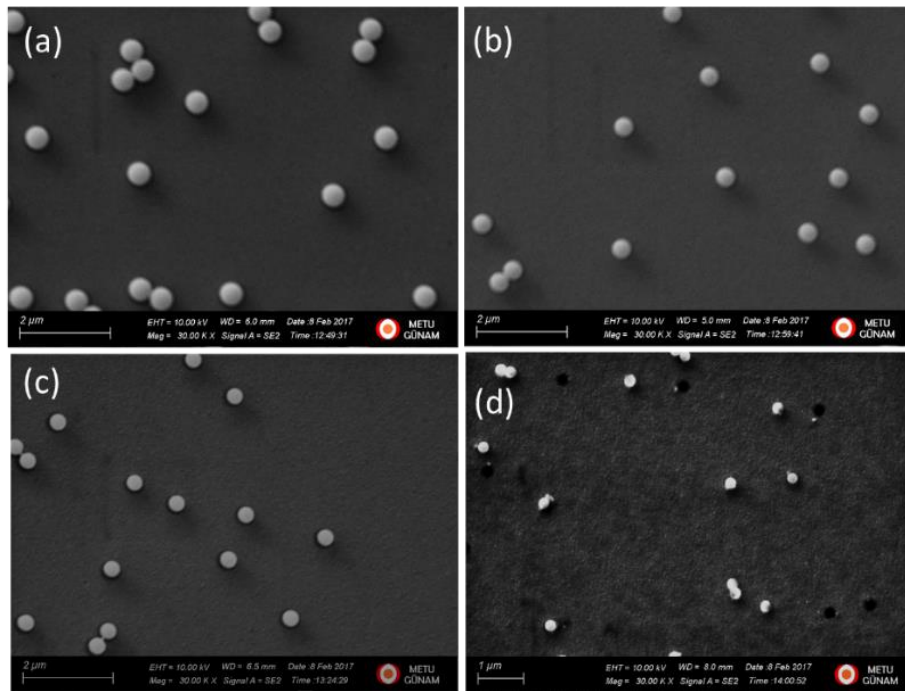


Figure 3.13. SEM images of PS nanosphere size reduction by Oxygen plasma etching (a) 500nm nanospheres as deposited (b) 5 minutes (c) 10 minutes (d) 20 minutes etched nanospheres

Deposition of the mask layer with a tilted sample holder while constantly rotating the sample is the second size reduction method that is explored. For examination of how this effect can be used to manipulate the hole size, hole masks are prepared with varied tilt angles and rotate the sample continuously during mask evaporation. Figure 3.14 shows the holes with reduced sizes when the evaporation angle is increased from 0 to 30 degrees. For all the samples, 500nm PS particles were used. The average size of resulting holes measured to be 435nm for 10° tilted, 400nm for 20° tilted and 330nm for 30° tilted samples.

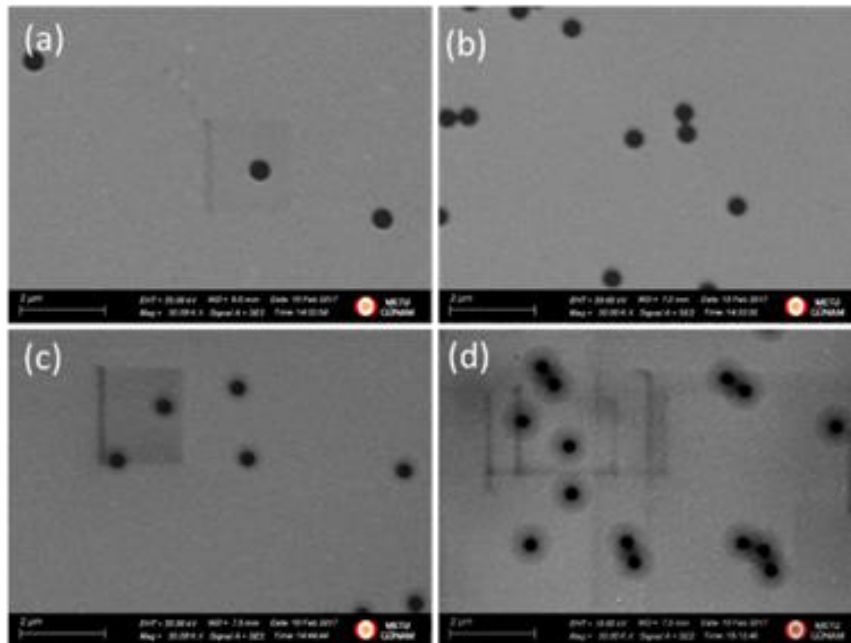


Figure 3.14. SEM images of hole size reduction tests by tilted evaporation of Au mask layer PS nanospheres of 500nm diameter are used. (a) no tilt (b) 10° tilt (c) 20° tilt (d) 30° tilt

After hole size reduction experiments, a new set is prepared for the fabrication of Au discs that have strong dipolar plasmonic peaks in the visible region. The purpose is to make the holes as small as possible to obtain smaller discs to see plasmonic activity using visible and NIR excitation using 500nm nanospheres. First, a 1 μm PMMA layer is spin-coated, and its surface is decorated with 500nm PS nanospheres. Then, a size reduction step of 15 minutes of Oxygen plasma etching was applied. The hole mask layer of 30nm SiO then evaporated with a constant tilt angle of 20 degrees while the sample was constantly rotating. After particle removal and cavity formation, 30nm Au is evaporated through the holes. The remaining PMMA and the mask layer are lifted off in acetone. The expectation for the resulting disc size by purely geometrical calculations was about 150nm. However, upon examination of SEM images, an average disc diameter is measured as 270 ± 15 nm.

The images shown in Figure 3.14 are performed with tilted mask evaporation of Au thin film. Au as a mask layer is later found to not work as an oxygen plasma mask

mainly because it melts due to Eddy currents caused by RF radiation inside the plasma chamber. That is why we needed a dielectric film, and due to its availability and compatibility with thermal evaporation, a SiO film was chosen. Another set of discs is fabricated, this time using 170nm silica nanospheres. Since silica is unaffected by oxygen plasma etching, only tilted evaporation as a hole size reduction method can be used. For these samples, 1 μ m PMMA surface is decorated with nanosphere with the same methods, and a SiO mask layer is evaporated on the surface with 20° tilted evaporation. Figure 3.15 shows SEM images of the PMMA layer after nanosphere decoration and the resulting hole mask. After nanosphere removal, oxygen plasma is used to etch and undercut the holes. Following the hole mask preparation, 30nm Au discs has been evaporated at surface normal angle. The resulting average discs' size is measured to be 174 nm \pm 38nm. The average size is still larger than expected, almost the same size with no tilted mask layer deposition. The size distribution divergence results from the low-quality suspension.

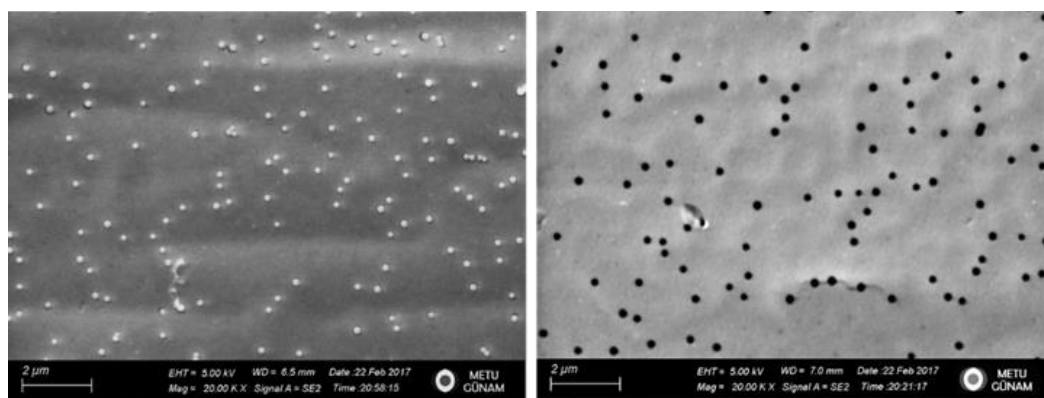


Figure 3.15. SEM images left: PMMA surface decorated with 170 nm silica nanospheres, right: hole mask layer after particle removal

In these experiments, we have seen that the size reduction of holes is applicable but only to some degree. The reason behind larger fabricated discs than expected is the failure of the SiO mask layer to hold its shape in thinner parts under the nanoparticle. Later, instead of a thermally evaporated SiO mask layer, a sputtered SiO₂ layer is

used. In the experiments, the sputtered SiO₂ mask layer observed to yield about 150nm hole diameter when 500nm PS spheres were used. Due to more isotropic deposition nature of plasma sputtering, this method achieves hole size reduction without the need for the considerations described in this section.

3.1.3 Strategies for Periodic Structuring With HMCL

HMCL is a great nanofabrication method as is. However, one drawback can be emphasized, which is the random decoration of structures on the surface. If we can somehow place the hole masks in a controllable periodic order, possible applications would increase significantly. Periodic decoration allows the fabrication of metasurfaces. Far-field scattering properties of collective plasmonic response can be harvested. Metasurfaces allow light manipulation at a distance using an ultra-thin surface. For this purpose, several methods for periodic surface decoration are proposed, and some of them are explored experimentally. This section involves details of these proposals and experimental studies conducted for the realization of these proposals.

Close-packed monolayer deposition of PS nanospheres has been successfully applied in our laboratories by a method called controlled evaporation, in which the suspension of nanospheres is spin-coated on the surfaces and left overnight for drying. It has been observed that a monolayer surface deposition can be achieved when the colloidal concentration is tuned correctly. The initial approach for periodic patterning with HMCL involves harvesting the close-packed deposition technique. However, for HMCL, colloidal nanospheres decorated on the surface, which then set the location of respective hole masks on the surface of the mask layer, are required to be isolated. Nanospheres deposited closely packed on the surface cannot be used the same way since there will be much less open space for the subsequent mask layer to cover the PMMA surface. The proposal involves etching the PS nanospheres with O₂ plasma before proceeding with mask layer deposition. Preliminary experiments were conducted on Si surfaces without PMMA, and the results show promise. SEM

images of close-packed deposited $1\mu\text{m}$ spheres and reduced-diameter periodic spheres after 10 minutes of O_2 plasma etching are shown in Figure 3.16 respectively.

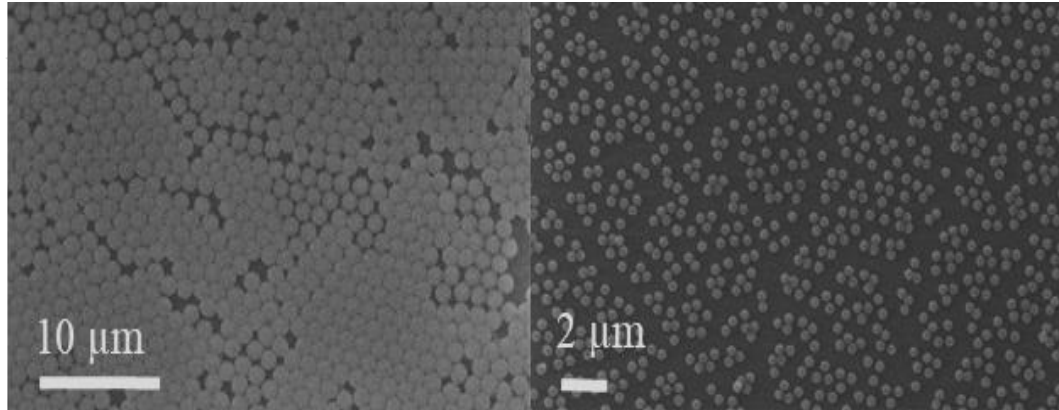


Figure 3.16. SEM images of Left: close packed deposited $1\mu\text{m}$ spheres, right: reduced diameter spheres after 10 minutes O_2 plasma etching

This proposal for the fabrication of hole masks is further investigated by the deposition of closely packed nanospheres on the PMMA surface. However, the adhesion properties of PMMA turned out to be quite different, and the same method did not yield close-packed deposition. This method was not further pursued experimentally in the context of this thesis; however, it shows promise for periodic decoration of hole masks as long as the thickness reduction of PMMA due to oxygen plasma sphere size reduction etch is compensated by thicker initial PMMA coating.

Another method proposed was the use of the interference lithography method for the hole mask decoration. In this method, some of the expanded UV laser beam falls directly on the sample, and some of it reflects off the mirror placed perpendicular to the sample and falls on the sample, called Lloyd's mirror setup. A schematic representation of the experimental Lloyd's mirror setup in our laboratory is shown in Figure 3.17. The path difference between the two parts of the beam creates an interference pattern on the sample. When this interference pattern is shined on the photoresist, the bright regions are exposed, while the dark region is not exposed so

that the interference pattern can be produced on the sample. In the double exposure method, at the end of the first exposure, the sample is rotated 90 degrees and re-exposed. When a negative photoresist is applied to the substrate prior to exposure, periodic holes with square periodicity can be obtained.

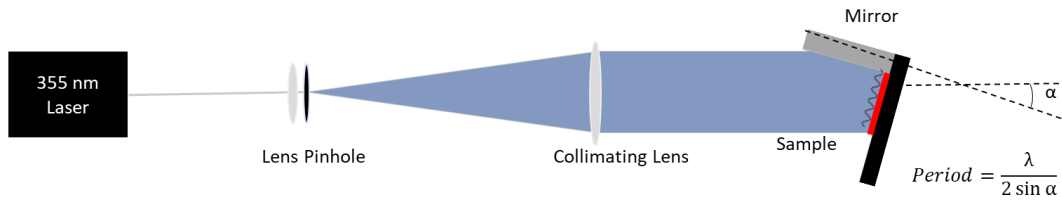


Figure 3.17. Schematic of Lloyd's mirror setup for interference lithography.

Experimental steps proposed for hole mask fabrication involving orthogonal double exposure interference lithography to produce periodic hole masks are illustrated in Figure 3.18. Su-8 2000.5 negative photoresist is used as the photoresist layer. SU-8 2000.5, which yields around 600nm thickness when spin coated at 3000rpm, is thinned with 2:3 PR:thinner ratio. The measured thickness is about 300nm at a spin speed of 3000rpm.

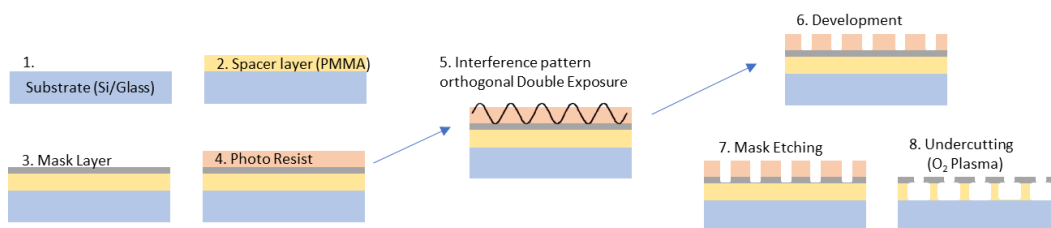


Figure 3.18. Proposed experimental procedure periodic hole mask fabrication with interference lithography

Several experiments are conducted for the reliable use of double orthogonal exposure interference lithography to optimize the exposure time of SU-8. These sets are prepared by directly spin-coating thinned Su-8 photoresist on Si substrates. The size

reduction of holes as the exposure time increases as expected; from these experiments, 27.5 second exposure is found to be the most appropriate exposure time. An AFM image of 27.5 sec orthogonally double-exposed sample after development is shown on the left side of Figure 3.19. When the line cross-section of the AFM measurement on holes are examined, it is found that the holes do not go all the way down to the substrate surface. The problem is even the areas that should not be exposed to UV laser are exposed a little. This may be originated from unequal intensities of two interfering beams creating a DC offset in the interference intensity distribution, exposing the dark region a little. Upon further examination of the specs of the mirror used in Lloyd's mirror setup, it turns out there is a mere 4% loss from reflection at the laser's wavelength even though the mirror is optimized for UV region.

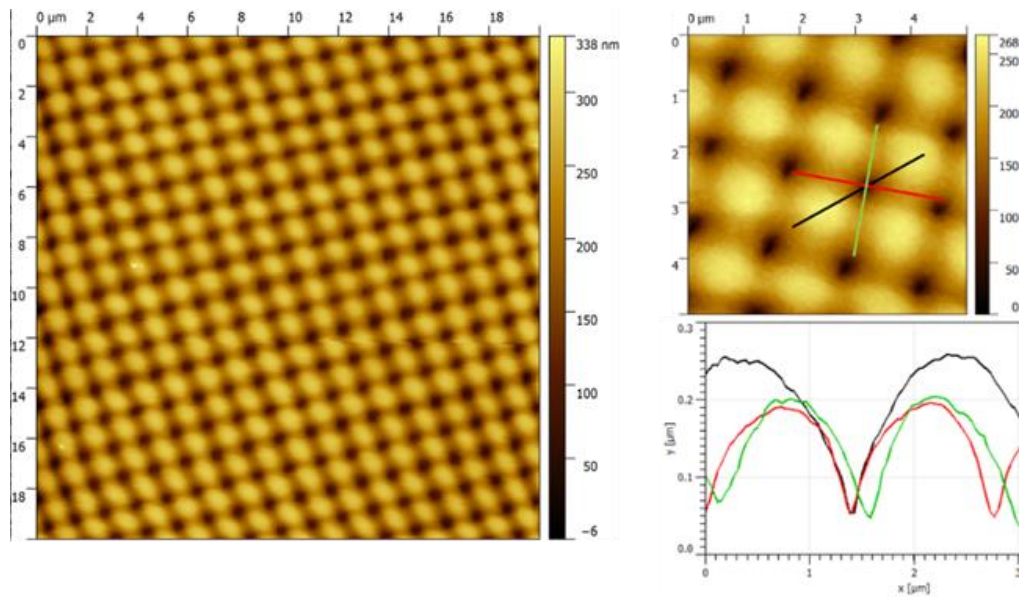


Figure 3.19. Left: AFM image of 27.5 sec orthogonally double exposed sample after development. Right: line cross-section analysis on the sample

The use of oxygen plasma etching is proposed to overcome this problem. By a mild oxygen plasma etching after development the sample surface can be reached at the hole regions. To test this several samples are fabricated with same parameters and

etched at various durations. AFM images of the sample after varied oxygen plasma etching time can be seen in Figure 3.20; line cross-sections at hole regions are included at the bottom of the figure. It is clear from the flat regions at the bottom of cross-section graphs that the etch method works. The sample surface is reached after 10 minutes of plasma etching without significant hole size increase.

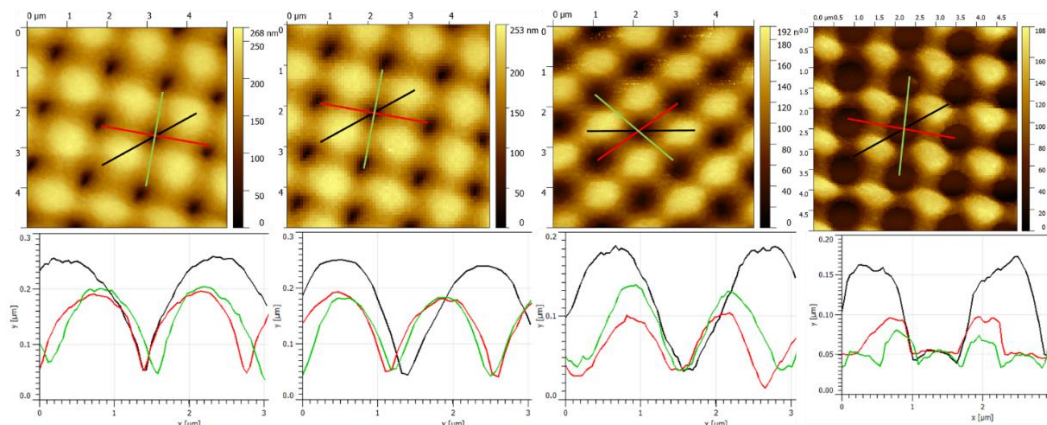


Figure 3.20. Up: AFM images of 27.5 seconds exposed samples after oxygen plasma etching for 0min, 6min, 10 min and 20 min respectively. Down: The line cross-section plots taken from hole regions of respective images.

Following the successful results from hole fabrication with interference lithography, a full trial for hole mask interference lithography (HMIL) is explored. Hole mask formation procedure in subsection 3.1.1.1 is followed. Colloidal sphere deposition step is omitted, directly depositing SiO_2 mask layer over plain PMMA surface. SU-8 photoresist spin-coated on the mask layer for interference lithography; however, at this step, it has been found out that the mask layer leaks solvent of SU-8 photoresist, causing swelling of PMMA that forms cracks on the mask layer. Another trial with thicker mask layer reduced the cracks, but we could not get rid of them completely. The leak is thought to be originating from micro-cracks on the mask layer, a different mask layer material or a more refined deposition method may overcome this problem. However, HMIL trials are terminated at this point; the fabrications are continued with standard HMCL described in subsection 3.1.1.

3.2 Optical Characterization

Optical characterization of fabricated plasmonic structures is characterized by dark-field spectroscopy. In DF spectroscopy, the sample is illuminated with a ring of broad-spectrum light, and only scattered photons are collected from the middle of the illumination ring. This setup allows only the diffuse light to enter the spectrometer and eyepiece, leaving the direct reflections or transmissions outside of the light collection cone. A DF setup is shown with an image of scatterers with different plasmonic resonances, shown in Figure 3.21.



Figure 3.21. Left: schematic of dark field spectroscopy. Mid: The inverted microscope setup used in measurements. Right: A dark field image of a surface with different plasmonic resonances.

DF objective is equipped on an inverted microscope, and then the output port is coupled to a fiber spectrometer. A BaSO_4 powder-coated substrate is used as the reference measurement to eliminate spectral dependence coming from illumination source. BaSO_4 is known to be a very good diffuse scatterer for the visible and NIR regions with over 95% diffuse reflection and very little spectral dependence; since spectral dependence is so small, the measurements did not further correct to reference spectral reflection. Both measurements from the reference and the samples are collected at same integration time and averaging settings. To achieve same data

collection parameters, an attenuator is used for reference measurements. This way, when normalized, the resulting spectrum should correspond to the normalized scattering cross-section of the plasmonic structures on the surface. In Figure 3.22, SEM images of fabricated Au nanodiscs with average sizes 175 nm and 270 nm and their dark field microscopy images are shown in the lower pane. With dark field microscopy, we can clearly distinguish sub-diffraction limit size particles, thanks to their strong plasmonic scattering. The surface distribution of SEM and DF images align well. The produced discs scattered light show a reddish hue, which correlates with the spectrum results in Figure 3.23. Dark field scattering spectra obtained from these samples are shown in Figure 3.23. A transmission mode DF setup was used to obtain the spectrum, the samples were illuminated from glass side. The illumination numerical aperture of DF objective used is 0.80-0.95, which corresponds to incident angles ranging from ~55-70 degrees in the air, as the illumination is from the glass side, refraction makes the incident angle roughly ranging from 32 to 40 degrees, these values are used in model building for experiment matched simulations. The transmitted part of scattered light is collected by a 40x, NA=0.60 imaging objective. The surface is imaged, and spectrum data is collected from regions without any other strong scatterer in vision (like dust particles). The same measurement setup is used for all scattering measurements reported in this thesis.

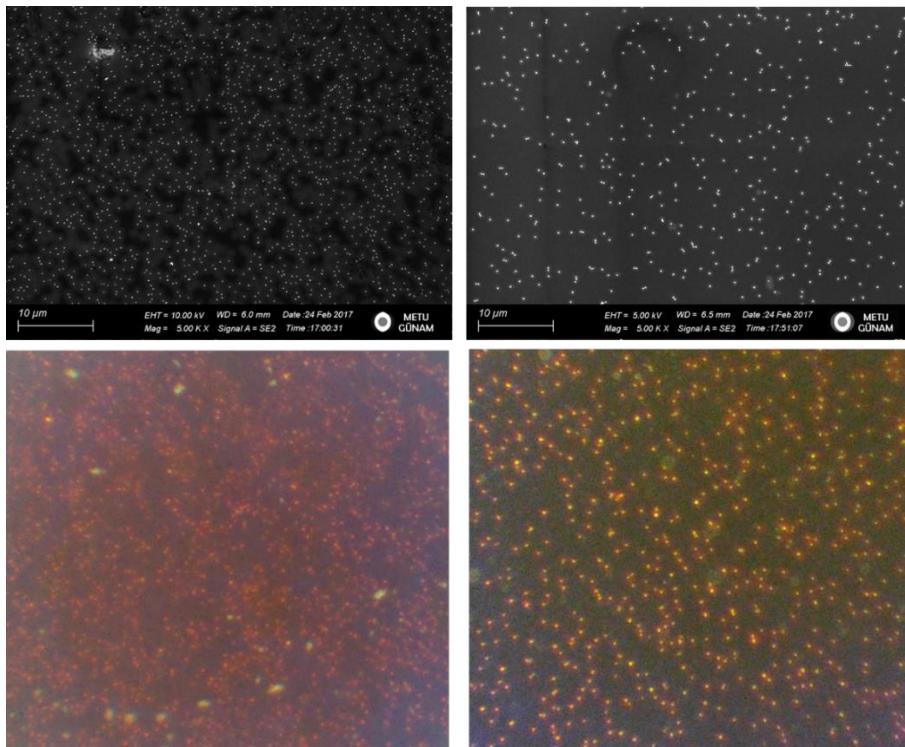


Figure 3.22. Left to right 174nm and 270nm average sized Au nanodiscs. Upper: SEM lower: Dark field optical microscope images

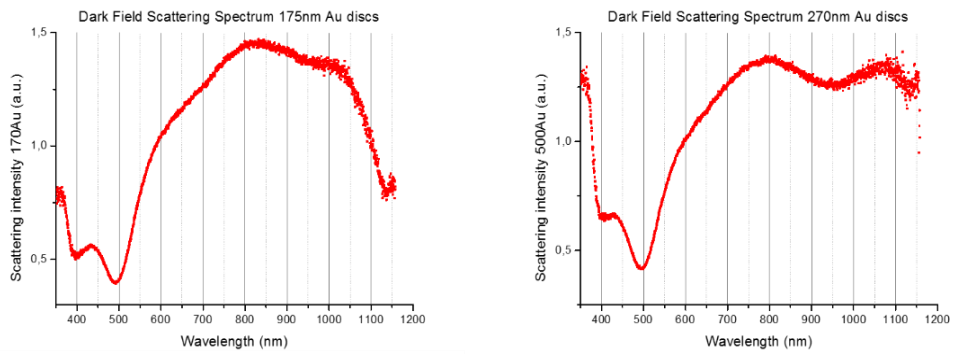


Figure 3.23. Dark field scattering spectra obtained from samples of Au nanodiscs of 175nm and 270nm average sizes respectively.

3.3 Numerical Simulations

Exploration of a theoretical model often results in new scientific discoveries. Although the Maxwell equations have been well established, they are seldom solved exactly in nanophotonics. Consequently, it is necessary to solve the equations using numerical methods in order to identify the events predicted by the equations. The theory and numerical solutions aim for results that have the potential to be observed in experiments. These observations can be used to confirm whether the experiment aligns with the physics anticipated by the model or whether it reveals surprising new occurrences that may improve the theoretical background. Simulations serve as an intermediary between theoretical concepts and experimental observations.

Today's simulation tools and personal computers are capable of numerically solving full Maxwell's equations for arbitrary nano geometries considering the substrate or surrounding discontinuities and include the effect of the surface distribution of nanostructures when the model is built correctly. It is clear that getting a close solution to fairly complicated problems has never been this accessible. Experimental refractive index values for these materials are used in all calculations. Most used refractive indices are adapted from experimental results in literature: fused silica glass substrates [212], Si substrates [213], and Ag and Au [214].

In this thesis, "Mnpbem17" is utilized as the primary simulation tool due to 3 main factors. Firstly, it is an open-source tool enabling deep modifications that work on Matlab, a well-established programming environment. Secondly, it employs the boundary element method, enabling relatively faster computation. Finally, it has very good documentation with several example models covering most of its capabilities, which are included in the toolbox. Moreover, Mnpbem can solve for layer structures, which is crucial since plasmonic response is affected strongly by the surrounding media. Despite its advantages for some problems, Mnpbem is not the best tool for calculation, such as transmission from a surface with periodically decorated plasmonic structures, as light interference comes into play and affects the far-field radiation pattern. One important consideration is there is a large room for mistakes

in the model-building stage; as a modular tool, there are lots of parameters to choose correctly to build a physically and numerically correct model.

Using the Mnpbem toolbox, field enhancement near the particles and Scattering, Absorption, and extinction cross-sections are obtained for nanoparticles with arbitrary geometries on arbitrarily many layers. Their far-field radiation patterns are also calculated. One example of Mnpbem's shortcomings is a case with periodic structures; as a boundary element method, it cannot simply solve for periodic structures, such solutions may be possible but not without new code to implement far-field interference additions on the source code. A secondary tool for patching the shortcomings and confirming the results, Comsol Multiphysics, is used with the wave-optics tool package. Comsol has a well-established environment with a lower number of parameters to tune, making mistakes harder, but it takes longer both to build the model and to solve it.

With the finite element method, problems for periodic structures can also be solved by using periodic boundary conditions. A more comprehensive method has been developed to determine the overall photonic effect of nanoparticle arrays placed on dielectric surfaces, including the effect of surface coverage. For this purpose, reflection and transmission coefficients are calculated in Comsol with periodic boundary conditions on the sides of the computational domain with the nanoparticle placed in the middle. This way, the size of the computational domain determines the overall surface coverage of nanoparticles and overall reflection and transmission coefficients. Simulation results for periodically placed 100nm discs on Si substrate are shown in Figure 3.24.

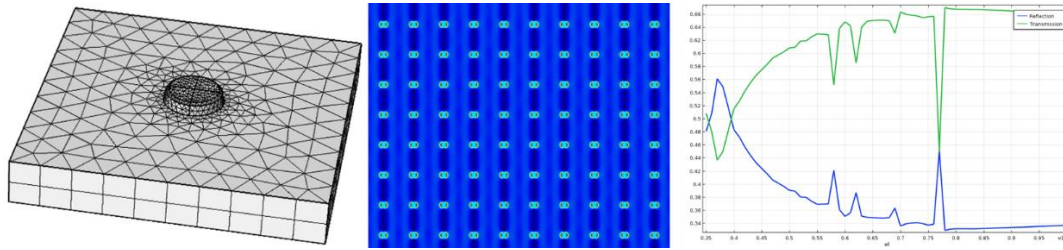


Figure 3.24. A FEM simulation of periodic array of 100nm diameter discs. Left: Meshed geometry of 100nm disc on Si substrate. Mid: Electric field distribution on the substrate surface. Right: Calculated reflection and transmission coefficients.

For all simulations reported in this thesis, three different PC's are used, personal laptops, one with 2.7 GHz Intel i7(2nd gen) processor with 8GB Ram which is later replaced with 4.3 GHz AMD Ryzen7 (4th gen) processor with 16GB Ram or a Desktop PC with 4 GHz i7(7th gen) processor and 16GB Ram, although there were many occasions these PCs were not enough to solve the problem in reasonable time or even at all. In such cases either the problem simplified, discretized more coarsely or different approaches to obtain a physically accurate result have been investigated.

One of the most important things came upon working on several different problems in both simulation tools is the simulation reliability. The simulations do not always proceed as expected and yield the correct physical result; in fact, it has been observed that the result is most likely wrong on the first try. That is why checking the result with analytical models and testing the model with different parameters is very important. Simulation workflow to obtain confidence in results can be summarized with steps shown in Figure 3.25. The workflow starts with the model building, where numerical methods may diverge from actual physical results due to either mistakes or ill-defined parameters. For debugging any possible mistakes, a time-efficient approach is to build a simpler case of the model either by simplifying the geometry or reducing discretization points. For example, a layer-structured problem containing thin dielectric layers below the nanostructures was first simplified to a single-layered problem for preliminary results. The thin layer onto the substrate is added only after preliminary results gain some confidence in terms of physical consistency and

discretization optimizations. After building the model the problem is solved more than once with different discretization's since a physical result should not depend on the discretization (meshing) used in the numerical approach.

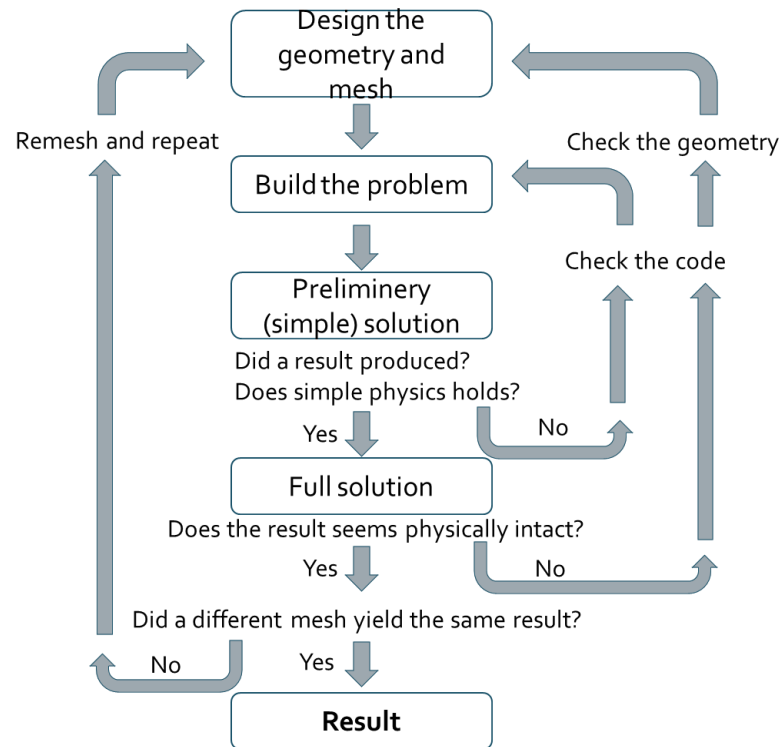


Figure 3.25. Workflow of simulations

3.3.1 Cross Validation

A good validation of the simulation results would be to get the same results with different numerical or analytical approaches for the same physical problem. MNPBEM's built-in models incorporate Mie theory for spherical or elliptical small particles, moreover it incorporates quasistatic approximation for arbitrary MNP geometry. These results are useful to compare with retarded Maxwell solutions at conditions where these approximations are valid. The MNPBEM's Maxwell solution

plotted with the calculation with the Mie theory and the quasistatic approximation for a 10 nm diameter Au disc are shown in Figure 3.26.

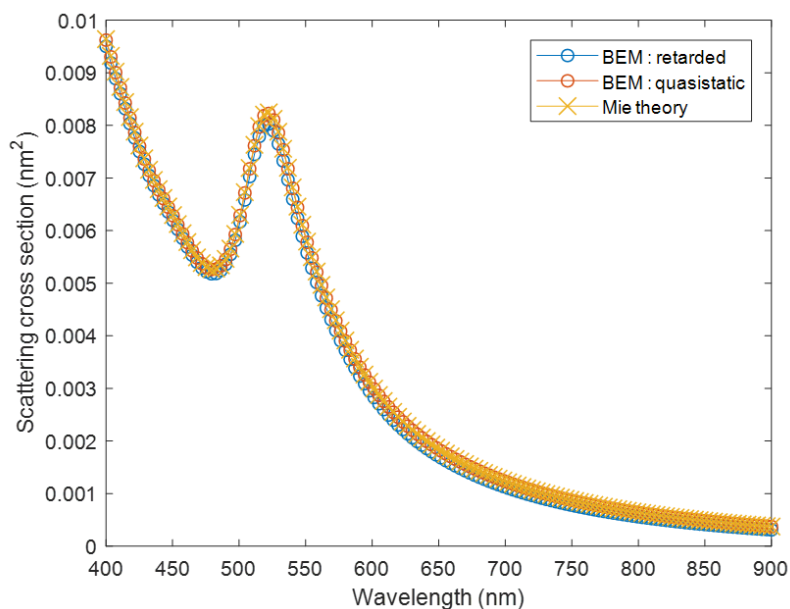


Figure 3.26. Scattering cross-section of a 10nm diameter Au nanosphere, the comparison of Mie solution, quasistatic solution and retarded full Maxwell solution calculated using Mnpbem toolbox

Quasistatic solutions quickly diverges from actual solution quickly as the particle size increases, the divergence is apparent for particle diameter above 50nm and quasistatic solution should not be used for larger nanoparticle size. Figure 3.27 clearly shows the large discrepancy between quasistatic and retarded scattering cross-section solutions for a 100nm Au nanodisc.

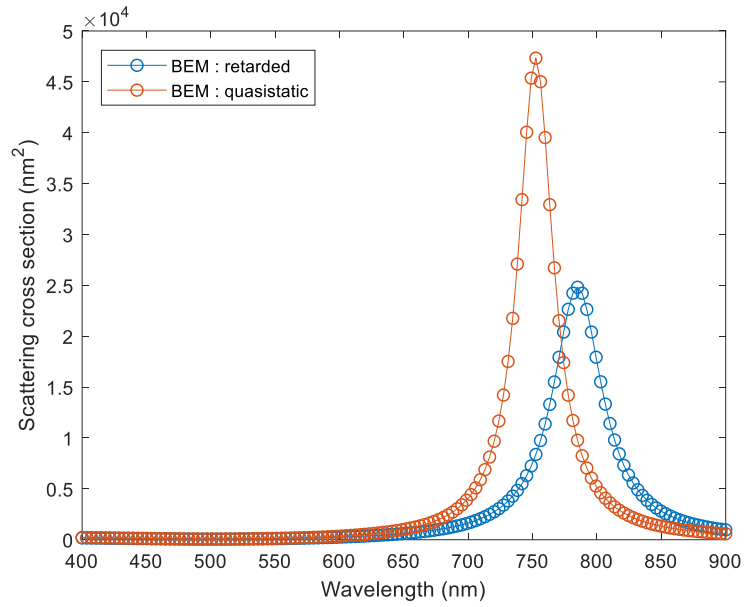


Figure 3.27. Scattering cross-section of a 100 nm diameter Au nanodisc, comparison of quasistatic approximation and retarded full Maxwell solution

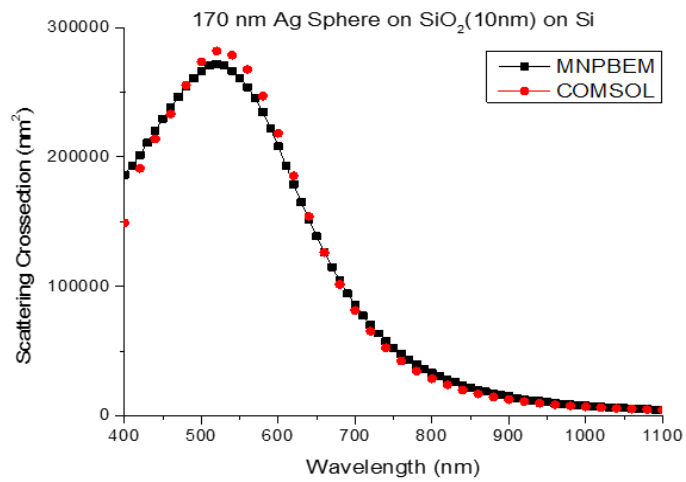


Figure 3.28. Comparison of scattering spectrum graphs calculated with MNPBEM and COMSOL. For a sphere with diameter 170 nm placed on 10nm SiO₂ coated Si substrate

For larger particles where, the quasistatic approximation is no longer valid, Comsol is used for result comparison. The two different 3D Maxwell solution methods yielding the same result strongly supports the reliability of the results. For this purpose, a planewave excitation model for a disc with diameter of 170 nm placed on 10nm SiO₂ coated Si substrate has been built in both Mnpbem and Comsol, the obtained scattering cross-sections are shown in Figure 3.28. When the workflow for correction shown in Figure 3.25 is followed the results closely matches.

In another problem where pre-modelled 3d mesh file for nano-cube is imported into model. Same problem is with same particle model file used for solution in both tools. For this specific problem 3 different solutions are performed for 8, 12 and 19 nm thicknesses of Si₃N₄ on Si surface as the substrate. The scattering cross-section calculations show close relation and shown in Figure 3.29. These results validate the solution accuracy as two completely independent Maxwell solver yielded same outputs. The mesh import code for Mnpbem is shared in Appendix A.

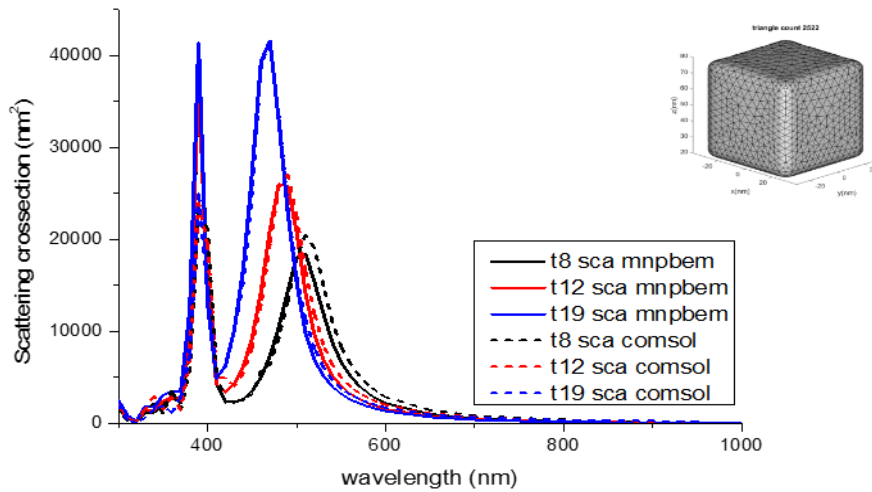


Figure 3.29. Comparison of scattering spectrum graphs calculated with MNPBEM and COMSOL for a 60 nm side length cube placed on 8, 12 and 19 nm of Si₃N₄ coated Si substrate.

3.3.2 Considerations about Discretization

The design of the geometrical features is one of the most important and challenging parts of a successful simulation, as the discretization resolution is determined at this step. The reliability of the results is directly affected by the mesh density until some point when the density is enough. If the mesh is not fine enough, the results are wrong. Thus, a problem must be solved for different mesh densities to make sure the meshing is enough. Over-meshing, on the other hand, unnecessarily increases the problem size, increasing the solution time and memory requirement. Moreover, since this dependence is polynomial, even a small increase in mesh density may make the problem unsolvable with the hardware; thus, in all the numerical simulations with large problem sizes, instead of trying to find better hardware, mesh simplification is preferred. A scattering cross-section calculation for the same structure with different meshes on MNPBEM is shown in Figure 3.30; in this figure, the left geometry surface is uniformly meshed, and in the right geometry, the number of meshes is reduced non-uniformly with shape preservation, resulting in a red shift in scattering peak position. The shift is due to sparse meshing on the surface of the structure. The skin depth of the metal is found to be a good distance for adjacent discretization point distance.

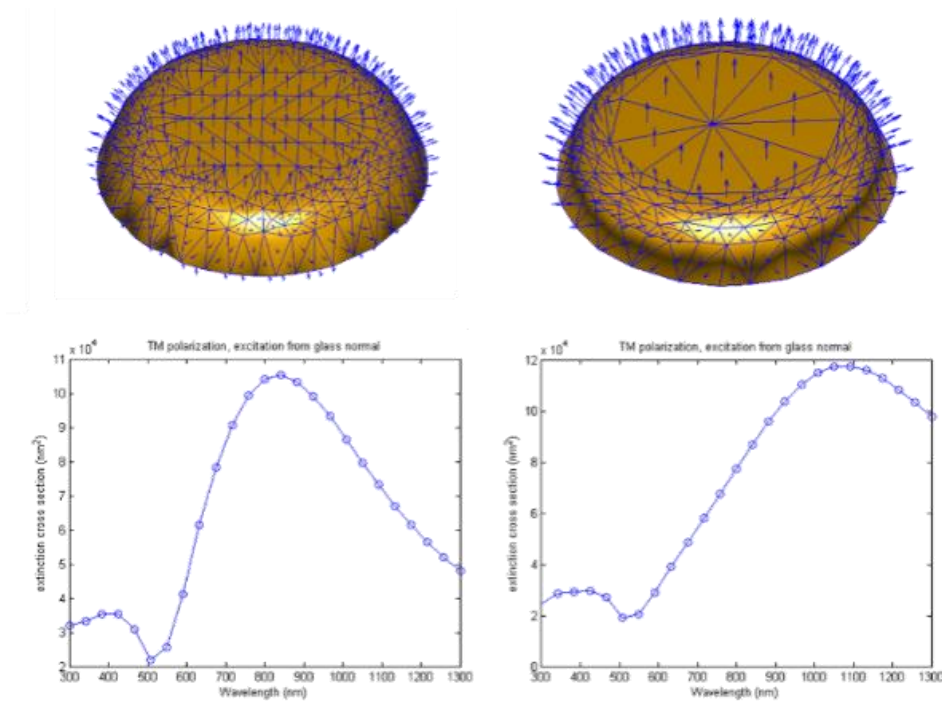


Figure 3.30. Scattering cross-sections calculated for same structure but different meshing parameters using MNPBEM.

Both Mnpbem and Comsol have the tools to design some geometrical features and to discretize them with various mesh densities. However, included design tools are somewhat primitive compared to more advanced CAD software. Thus, for any simulation with a complex geometry, I prefer to design the geometry using CAD software, namely Autodesk Fusion 360. After design, the 3D object is exported in a mesh file to be imported to simulation software. Comsol allows further remeshing and refining after the import; Mnpbem uses the mesh on the imported file directly. Thus, for BEM simulations, another mesh refining software, Autodesk Meshmixer is used according to need for further refinement and manipulation of discretization distances.

An example showing the effect of mesh density for FEM simulations is shown in Figure 3.31, in this example Ag nanocube array with 50% surface coverage on Si/Si₃N₄ substrate with 8nm (T magenta R yellow), 12nm (T red R cyan) and 19nm (T blue R green) Si₃N₄ layer thicknesses are calculated using Comsol. For the

solution on the left panel has a coarser mesh. The results seem to be somewhat spiky with a lot of errors, when a finer mesh is used in right panel, it greatly improved the spikiness in the solution but the solution time has been increased from 2hr to 10hr. Moreover, even the solution with denser mesh seems to be a little bit spiky in the blue side of the spectrum and should improve as the mesh density increased further. Although the example is from Comsol, Mnpbem solutions are also suffer from similar problems. Irregularities, inconsistencies in the solutions should be examined for all simulation results.

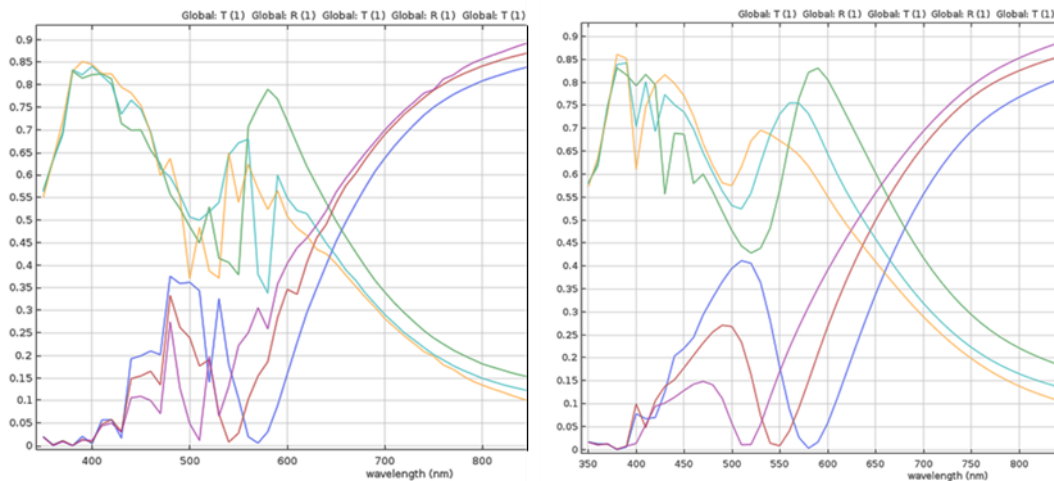


Figure 3.31. Reflection and transmission coefficients of a surface covered with periodically placed Ag nanocubes calculated using Comsol. Left: coarse meshed cube (~2hr solution time), right: finer meshed cube (~10 hr solution time)

Choosing a uniform and fine mesh distribution (ie. Triangles are roughly equal in size) is a natural way to start a simulation, but for some problems uniform meshing increases the problem size beyond hardware limitations unnecessarily. Another approach may be to increase the mesh around the region of interest and leave coarser mesh for other regions. For example, when near field distribution is examined, regions with the sharp features could be meshed denser since field amplitude greatly changes around those regions. Such a mesh refinement observed to improve scattering results without adding computational load. Another mesh simplification

for relatively larger nanostructures for FEM simulations is reducing the mesh density inside the particle at regions farther than the skin depth. The electric field amplitude inside the metal deep below the skin depth will quickly decay to zero a fine mesh is unnecessarily increasing the solution time.

One of the challenges faced when simulating complicated geometries is determining how well a mesh is enough, a good way to make sure is solve for more than one randomly dense mesh and examine the results. If the results seem to be same than the mesh is enough and the result obtained can be said to be reliable. However, it is generally not so simple most of the time because of the hardware limitations on the problem size. For some problems an adequate mesh could not be reached that can be solved within a reasonable time, yielding the problem unsolvable.

3.3.3 Model Building

After defining the geometry and mesh, the next step is to program the software to correctly model the problem and get desired information. Time should be taken in this step as all inputs and outputs should be correctly modelled and inputted to the simulation software. Parameters like illumination, polarization as well as required properties as output and required calculations on the results are all embedded to the software in this step.

Depending on required outputs the problem can be designed in different ways yielding the same result. Mnpbem contains a well-prepared documentation with appropriate examples makes this step a bit easier. Unfortunately, Comsol lacks key point explanations and examples in my opinion may be because it has many more different packages and aspects. In FEM simulations conducted with Comsol, appropriate boundary conditions have to be chosen. Computational domain can be terminated with perfectly matched layers (PML's) which absorbs all incoming radiation to damp unrealistic back reflections from computational domain boundaries. In some simulations periodic boundary conditions are used on sides of

the computational domain to simulate infinite material boundaries or periodically placed structures.

When the problem is “ill built”, most of the time, the software gives an error stating that there is a problem within the code. When such problems are faced problem is debugged until it works properly. The code should be carefully examined for any physical error at each parameter. One of such mistakes is made when using Comsol to calculate field distribution around an arbitrary nanoparticle. The mistake was definition of the incident field constant in space ($E_{inc}=E_0$ instead of $E_{inc}=E_0\exp(ikz)$). Results seemed to be correct initially but with wrong results of course. Such “silent” mistakes could be dangerous and should be very carefully investigated to be confident on the obtained result. Some other types of issues may occur due to the way that the program handles the problem. Such underlying properties of simulation software are most of the time embedded inside the code and not visible directly to the user, thus it is hard to debug. I generally start by changing model parameters that are open to manipulation and try to solve the problem each time with a different value, which requires many hours of computational time.

One of the “ill-built” problems, as shown in Figure 3.32, occurred while simulating for cross-sections of an Ag rod on glass under different incidence polarizations. As can be seen in the graph on the left at some point scattering cross-section abruptly peaks overcoming the extinction, moreover at that region absorption cross-section is found to be negative. In the right graph the problem does not occur for the same problem built and same mesh properties. The only change made between these two simulations was to lift the nanorod to 0.5nm above the substrate. Such a change should not have a significant effect in terms of physics, but due to how the software handles the solution, such a physically subtle difference sometimes becomes the line between correct and wrong results. Let’s say if we were only interested in scattering cross-section and only calculate for it, under such a circumstance, we would assume the “ghost” peak was physical and try to explain it, even build new or modify existing models. This emphasizes the importance of checking the results for errors and getting confident over it by testing it under different parameters.

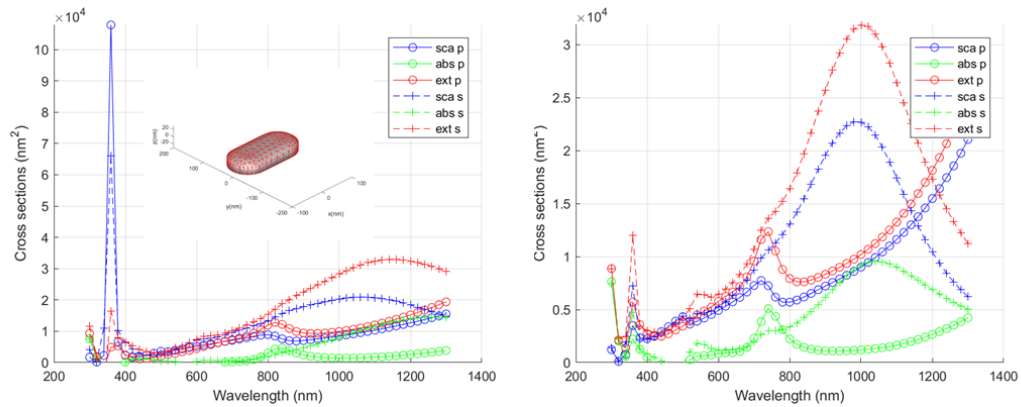


Figure 3.32. Scattering absorption and extinction spectrum of a nanorod on glass for parallel and perpendicular illumination obtained by BEM simulations. Left: particle is 0.1 nm above the surface, right: particle is 0.5 nm above the surface

3.3.4 Experimental Validation

The agreement between experimental and computational results is the most direct way to get confidence about simulation results. Matching experiment and simulation for a simple disc geometry was the first purpose in this context. Scattering spectra is collected with the dark field spectroscopy setup. To reproduce same experimental setup numerically, illumination conditions should match the DF objective used for measurements. This is achieved by calculations for light incident angles from 32 to 40 degrees with 1-degree step, solved independently for both TE and TM polarizations. The scattering spectrums calculated for each angle are averaged at each wavelength value. The simulation results for a 175nm Au disc is shown in Figure 3.33. The Matlab code for DF matched calculation with Mnpbem is shared in Appendix B.

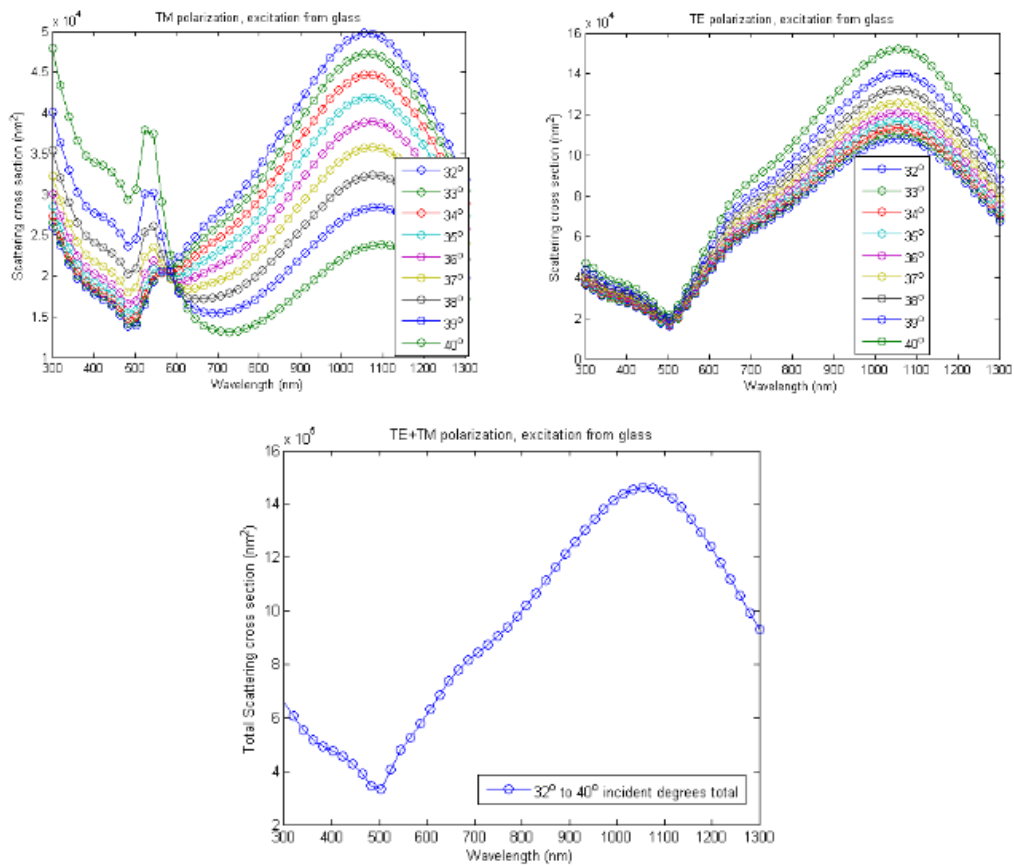


Figure 3.33. Calculations for a 175nm Au disc on glass. Up: Total of 18 simulations calculated for dark field objective illumination. Down: The average of all results is expected to match the experimental measurements.

Discs have been fabricated using hole mask preparation the procedure discussed in section 3.1 on glass substrate. 30nm of Ag is evaporated from the holes at zero polar and azimuthal angle. A SEM image of this fabrication containing randomly distributed discs is shown in Figure 3.34 left side. The average diameter of the discs is measured as 150 nm from SEM images. When 150 nm diameter value is used in simulations peak position did not match with the experiment, thus particle size is modified slightly, it has been observed that exact peak position match is obtained when the disc diameter of 160 nm. This discrepancy may be in the range of measurement and/or calculation errors. The experimental and simulation comparison

of the normalized scattering cross-section have been shown in Figure 3.34. As it can be seen almost perfect agreement is observed.

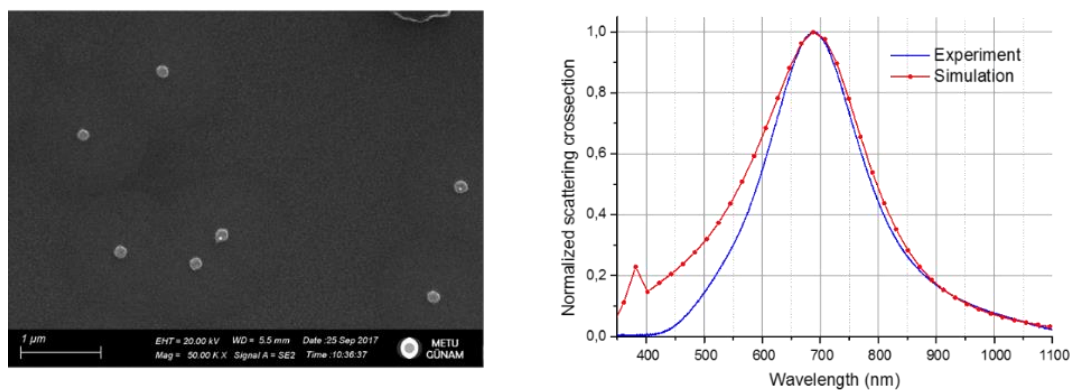


Figure 3.34. Left: SEM image of fabricated Ag discs with 150 nm average diameter
Right: Measured scattering spectrum (blue) and Mnpbem simulation (red)

CHAPTER 4

EXPLORATION OF PLASMONIC RESPONSE

In this Chapter, some plasmonic interactions are examined experimentally and computationally. First, the plasmonic coupling of structures with close gaps is explored. Two fabrications of Ag disc dimers with varied gap distances have been fabricated. Polarized optical measurements are conducted in order to show the plasmonic coupling effects on the overall scattering and SERS response of fabrications. Experiment-matched simulations are conducted, and the results are discussed. Second, various plasmonic structures with complex geometries, using the full potential of 2-axis motorized HMCL, have been fabricated. Scattering cross-section measurements are analyzed, and results indicate the presence of multiple resonance peaks and/or broadband resonance peaks. Finally, numerical calculations are conducted for plasmon-enhanced photovoltaic devices. One of the promising applications of plasmonic structures is possible efficiency enhancement by photovoltaic surface decoration with plasmonics. Plasmonic structures can scatter light very effectively with scattering cross-sections much higher than their geometrical cross-sections. Moreover, when the structures are on an interface, most of the scattered light is directed towards a higher refractive index medium, and the ratio of this directional scattering preference increases as the index gradient is higher. In this section, numerical studies and approaches for harvesting these properties for PV efficiency enhancement are reported. A model was developed incorporating cross-sections, far-field scattering distribution, and surface coverage for quantification of the overall plasmonic effect for a PV device. Several MNPs have been compared using this model.

4.1 Coupling of Closely Spaced MNPs

Coupling between close plasmonic structures has been examined through simulations and fabrication of several dimers with the optimized hole preparation procedure with 500 nm PS nanospheres with 150nm diameter resulting discs. Dimers are one of the most straightforward structures that can be fabricated using HMCL, enabling easy manipulation of distance between discs to manipulate electromagnetic interaction between them. Thus, they have an important role in our analyses. The Gap distance between discs is controlled by the azimuth angle between successive evaporations.

The scattering spectrum simulations are conducted in Mnpbem for dimers made of 150 nm discs on a glass substrate with varied gap sizes ranging from 10 to 50 nm, as shown in Figure 4.1. Continuous lines show the results when the incident light polarization is parallel to the dimer axis, while dotted lines are the results of perpendicular polarization. Scattering peaks show the effect of plasmonic coupling when the incident light polarization is parallel to the dimer axis, while when perpendicular, the peak position stays the same as the gap varies.

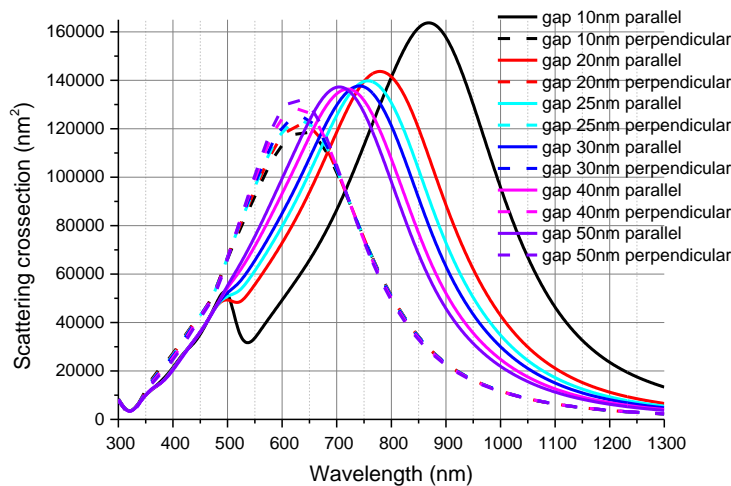


Figure 4.1. Simulation results for scattering spectra of 150 nm Ag dimers with varied gap size with normal illumination

Two of the many dimer fabrications are chosen for detailed analysis in this part, for the fabrication of these two, 30 nm of Ag evaporated at each fixed azimuth angles of ± 10 (dimer 1), and ± 9.5 (dimer 2) degrees at $0.5 \text{ \AA}^2/\text{s}$ deposition rate. The SEM images of these fabrications are shown in Figure 4.2. These fabrications are made both on Si and Glass substrates simultaneously. Si substrates are used for SEM imaging and Raman scattering measurements, while glass samples are used to obtain DF scattering measurements. All optical measurements conducted as soon as fabrication finished in same day to keep the effects of oxidation minimal.

Upon analysis of SEM images, the gap is found to be $\sim 20 \text{ nm}$ for dimer 1 and $\sim 10 \text{ nm}$ for dimer 2 which deposited with a smaller angle as expected. Moreover; with a rough analysis, distance between the discs found to be varied around several nanometers for different dimers on the same substrate. This indicates one of the important limitations of HMCL, the degree of gap control is in the range of several nanometers with used procedure not in sub-nanometer range.

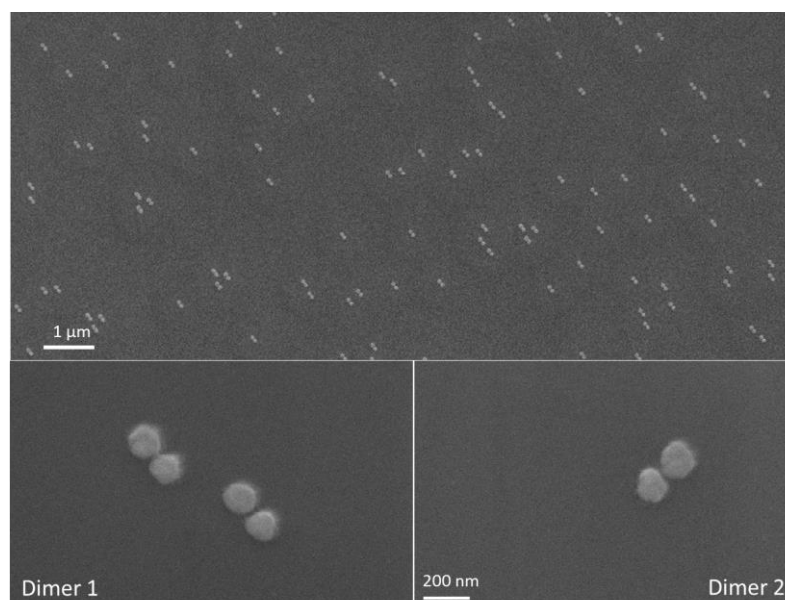


Figure 4.2. Up: Surface distribution of fabricated dimers, down: Close up SEM view of dimers fabricated with fixed azimuth angle of ± 10 for dimer 1 and ± 9.5 degrees for dimer 2.

4.1.1 Scattering Cross-section Analyses

Scattering spectrums of dimers are collected by adding a polarizer to the illumination port of dark field setup, keeping the dimer orientation w.r.to light polarization at parallel and perpendicular, two DF scattering spectra are collected from each sample. The resonance shift between polarization axis parallel and perpendicular to dimer axis is clear in the collected spectrums shown in Figure 4.3, proving the plasmonic coupling. Increased redshift of resonance peak for parallel illumination as gap becomes smaller in dimer 2 shows that, the interaction between close discs increases thus coupling between them increases as gap between them decreases. When the illumination polarization is perpendicular to the dimer axis, gap distance does not seem to affect the scattering peak, thus a very similar spectrum to isolated disc response is observed. This shows that plasmonic coupling does not occur when the illumination polarization is perpendicular. Results indicate as the distance between dimer get smaller the plasmon resonance peak redshifts when illumination is parallel to the dimer axis. When the illumination is perpendicular to the dimer axis, gap does not seem to affect the resonance peak significantly, as expected from simulations in Figure 4.1.

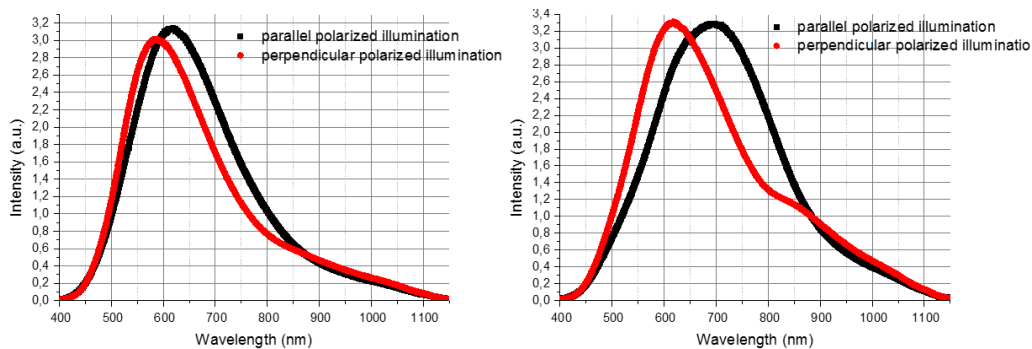


Figure 4.3. Polarized illumination scattering spectra collected from dimer1 and dimer2, black curves are obtained with polarization axis parallel to dimer axis and red curves with perpendicular.

Examination of experimental results and simulation results together a conclusion about the gap distance can be made by considering the amount of shift between parallel and perpendicular polarized illuminated resonance peaks. Experimental spectral difference of peak positions between parallel and perpendicular polarized illuminations are roughly 40nm and 80nm respectively for dimer 1 and dimer 2. Examination of simulation results in Figure 4.1 with measurements in Figure 4.3, the gap distance between dimer 2 should be around 50nm, while gap for dimer 1 should be much more if we compare the amount of total redshift. This seems to be a discrepancy between SEM images and simulation indications. However, such comparison is not accurate since experimental conditions does not match with simulated conditions. In simulations shown in Figure 4.1, substrates are illuminated with normally incident light while dark field condenser used in experiments illuminates the samples from a hollow cone with incident angle is a range of very oblique angles. To match simulation to the actual experiment, direction and polarization should be chosen accordingly. Numerically there is no way to illuminate from multiple directions simultaneously. However, results from different illuminations can be averaged to obtain experiment matching conditions.

A simulation model is built for experiment-matched simulation using Mnpbem, in which scattering cross-sections are calculated for the DF objective illumination cone for every degree, and then the angular results are averaged. The same calculation is performed for dimers with 10, 20, and 30nm gaps. The results are shown in Figure 4.4. The Mnpbem code for this calculation is shared in Appendix B.

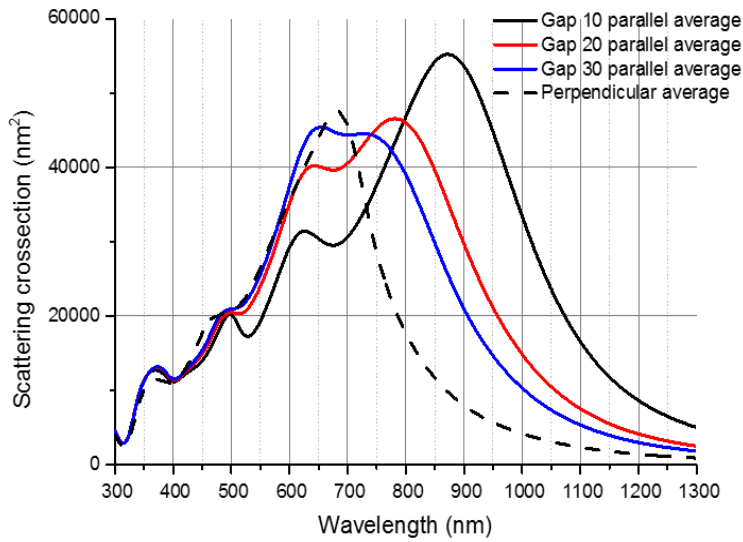


Figure 4.4. Scattering cross-section calculated for dimer gaps 10, 20 and 30 nm with DF objective matched illumination conditions

Comparing the results for normal illumination in Figure 4.1, in Figure 4.4, both parallel and perpendicular peaks are wider, and as the gap increases, the parallel peak gets closer to the perpendicular peak more rapidly. Perpendicular polarization peak also redshifts compared to normal incidence, but the peak is wider, as it does not depend on the gap distance significantly. Only the average is shown in Figure 4.4. We were also able to observe the quasistatic Ag peak around 350nm for both polarizations. Since fields for both cases have a component in the vertical direction, the Small (30nm) thickness of the disc is causing this extra dipolar resonance peak as the polarization of incident light has a component in vertical direction.

This analysis yields a more reasonable conclusion compared to the one made with simulations at normal incidence. When the experimental peak-shifts shown in Figure 4.3 are compared, gap distances can be estimated to be around 30nm for dimer 2. The distance found from SEM images was closer to 10 to 20 nm but the number of samples these direct measurements conducted are limited while dark field measurements collected from at least several hundred dimers. Probably the gap

distance distribution in the actual samples is high causing the discrepancy between experiment matched simulations and actual experiments.

Hole-to-substrate distance variation could be the main reason for gap size variation; this variation should be minimized by undercutting just enough to fit the structure in preparation. A careful examination of the upper image in Figure 4.2 shows a circular area surrounding dimers (undercut) that has a very large area ($\sim 1\mu\text{m}$ diameter), which could have been much smaller to still fit dimers ($\sim 400\text{ nm}$). When the undercut is larger, small differences in temperature between substrate and air above the mask can create stresses on the mask layer due to pressure differences creating little humps and burrows centered at the hole. Such humps and burrows may stay deformed at high vacuum conditions. This effect may be the main reason for poor gap distance stability and tunability. Making the undercuts smaller increases the PMMA support on the mask layer, lowering hole-to-substrate distance variation, which increases the stability.

4.1.2 Field Enhancement Near Dimers

One of the most important and interesting effects caused by plasmonics with small gaps is the electric field enhancement at the gap region. These local enhancements are called hot-spots. This enhancement boosts the interaction of light with matter in the vicinity of the plasmonic structure. One of the mostly recognized applications occurring from this boost is surface enhanced Raman scattering (SERS). The field enhancement around 100 nm diameter Ag dimers is simulated for varying gap distances as shown in Figure 4.5. For gap distances 5nm, 10nm, 20nm, 30nm, 40nm, and 50nm, maximum field enhancements are calculated to be 52, 25, 13, 10, 8, and 6 folds, respectively.

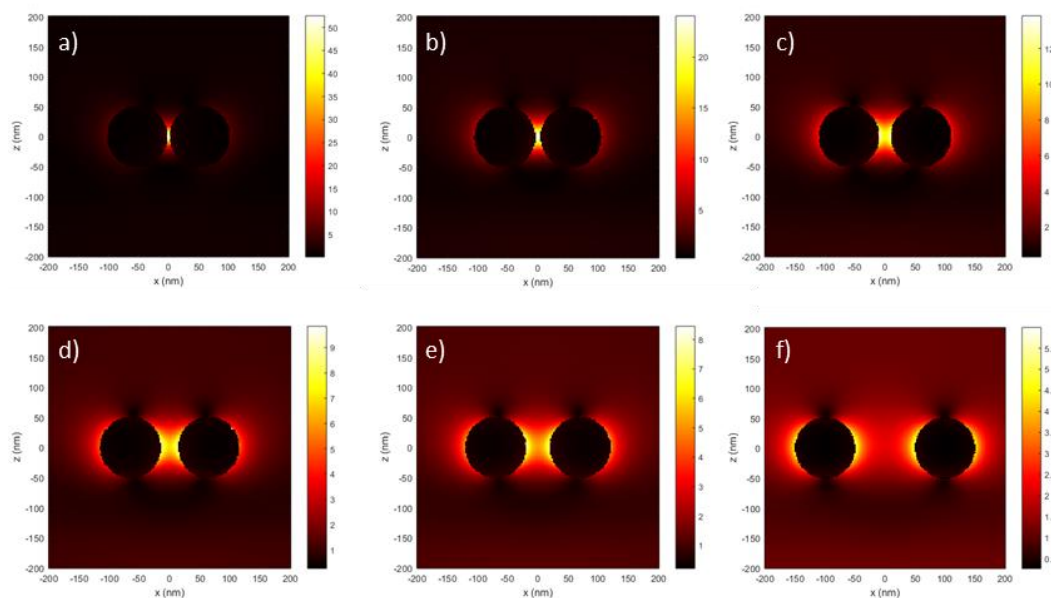


Figure 4.5. Relative electric field calculations around 100nm diameter dimers at 532nm illumination a) 5nm, b) 10nm, c) 20nm, d) 30nm, e) 40nm and f)100nm

The field enhancement occurring around plasmonic particles also enhances the SERS signal. To show this experimentally, dimer 1 and dimer 2 fabrications on Si substrates covered with a Raman active dye brilliant cresyl blue (BCB) for observing field enhancement properties. Raman measurements have been collected using a reflection setup on an optical microscope with a 532 nm excitation laser; the received signal is then filtered with a sharp 532nm notch filter and sent to a high-resolution spectrometer. Longer exposure times are used in the order of 100 ms with an average of several independent data. Note that the laser used can be considered unpolarized due to long propagation in fiber before coupling to the system. This has been validated by unchanged laser power measurements when a linear polarizer is rotated in front of the detector.

Raman measurement results are given in Figure 4.6. The graph shows Raman data collected from dimer-1 and dimer-2 samples discussed in the previous part and a bare Si surface after BCB deposition. The molecular structure of BCB is given as an inset. The small peak at 520 cm^{-1} is a characteristic Si peak coming from the substrate. The rest of them are BCB Raman peaks. Two dominant peaks are located

at 580 cm^{-1} and 1653 cm^{-1} , clearly observed in all measurements. Since smaller gaps are known to more efficiently enhance the field strength in the gap region, a higher BCB peak is expected from the dimer with a smaller gap. As expected, the dimer-2 decorated substrate has more Raman enhancement than the dimer-1 decorated one. Proving the increased field enhancement occurring closer dimers. Moreover, comparing the measurement for plain substrate, the substrate peak did not significantly enhance, which is also expected as hot spots poorly penetrate into Si substrate both because of the high refractive index and the absorptive nature of Si.

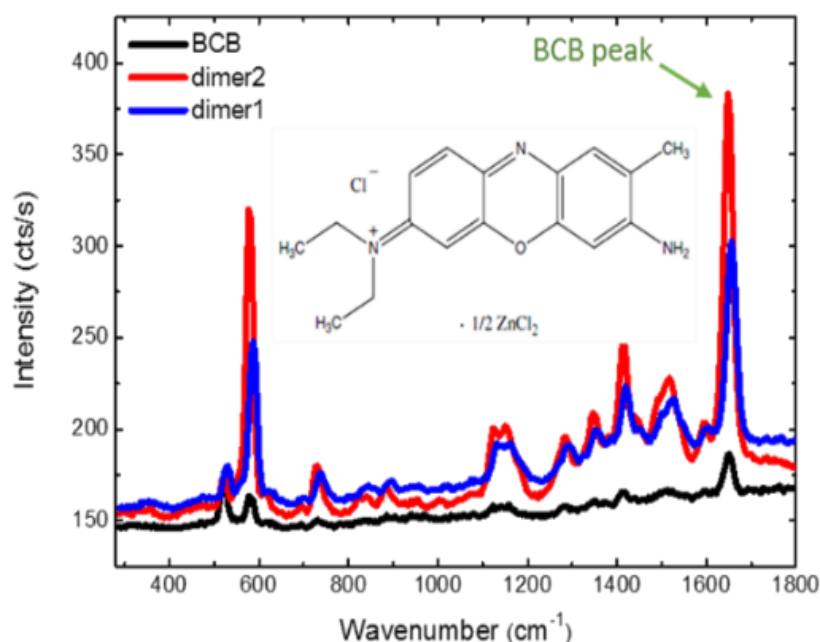


Figure 4.6. Raman measurement collected from BCB coated dimer1, dimer2 and bare Si surface with unpolarized laser.

Another measurement has been made on dimer 2 by linearly polarizing the excitation laser parallel and perpendicular to dimer axis has been shown in Figure 4.7. Since the laser power had to be set low to keep polarizing filter not burned and extra 50 % loss due to polarization, it is harder to see the BCB peak, thus exposure time of the camera is increased and a lower grid period grating is used which lowers the

resolution. Plain substrate and dimer-1 measurements are also collected but peaks were almost indistinguishable from the noise. In the graph the BCB peak at 1653 cm^{-1} is clearly distinguishable when the polarization is parallel to the dimer axis, while when illuminated with perpendicularly polarized laser, it is not distinguishable from the background. This result clearly supports plasmonic coupling at the gap region.

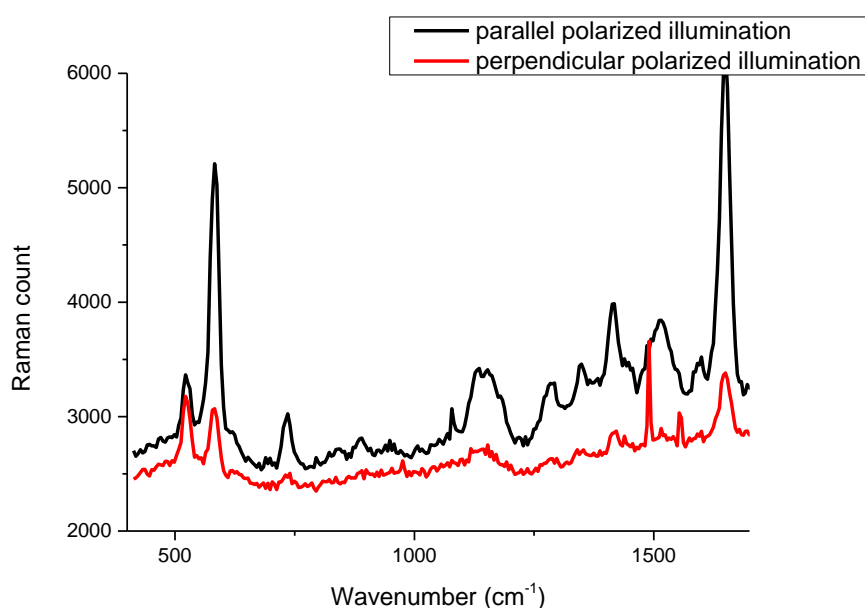


Figure 4.7. Raman measurement collected with polarized laser for polarization direction is parallel (red) and perpendicular (black) to dimer axis from dimer-2

An experiment matched simulation is modelled for dimer 2 with gap distance measured by scattering peak shift analyses ($\sim 30\text{nm}$) and SEM images ($\sim 10\text{nm}$). The field distribution calculation for 10nm gap is shown in Figure 4.8. shows simulation results of the enhancement in electric field norm for a dimer with 10nm gap. In the gap region maximum field enhancement is calculated to be about 30-fold for 10nm gap and about 10-fold for 30nm gap with parallel polarized illumination at 532nm . These enhancements may yield up to $10^4 - 10^6$ fold SERS enhancements from molecules at the hot-spot since probability of Raman events scales with the fourth

power of electric field strength. Experimental results indicate much lower enhancement factors since none of dimers shown significant Raman enhancement. This is due to very low surface coverage of dimers, which is about 3% as shown in Figure 4.2. The density of hot spots throughout the surface is even lower, we can observe this by considering the size of red regions (hot-spots) from Figure 4.8.

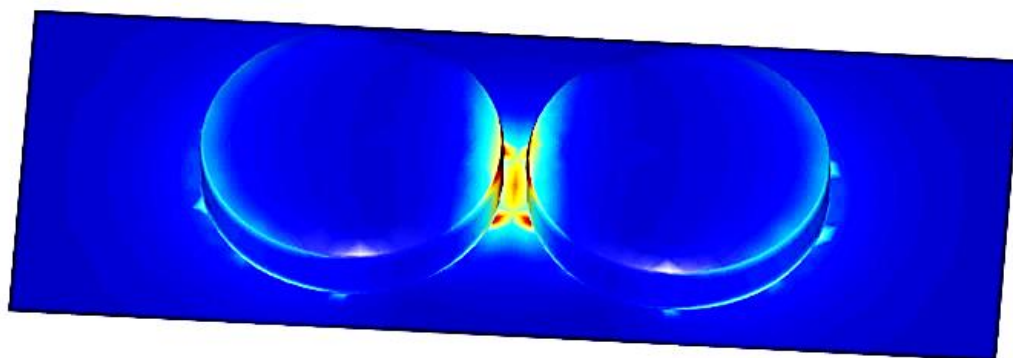


Figure 4.8. Plot of electric field distribution on and around of a dimer with 150 nm disc diameter on Si with 10 nm gap with parallel polarized 532nm illumination

While simply taking the 4th power of maximum electric field enhancement may approximate somewhat accurate SERS electro-magnetic EF value for a surface with densely populated hot-spots, such as plasmonic aggregates with sharp features; for sparsely distributed hot-spots like the dimers discussed here the approximation should also include non-enhanced fields on the surface. More accurate approximation may be achieved by using equation (4-1), integration of relative electric field norm over the surface divided by total area.

$$EF = \frac{\int_S E_{rel}^4 da}{\int_S da} \quad (4-1)$$

The total area S should be the average area on the substrate for each structure can be determined by surface coverage. For example, for a surface coverage of 5% total

surface area should be 20 times the structure area. E_{rel} is relative electric field norm calculated as the ratio of sum of incident ($|\vec{E}_{inc}|$) and plasmon induced (\vec{E}_{ind}) electric fields norm to incident electric field norm;

$$E_{rel} = \frac{|\vec{E}_{ind} + \vec{E}_{inc}|}{|\vec{E}_{inc}|} \quad (4-2)$$

Since the computational methods discretize the problem with appropriate steps equation (4-1) can be written as summation and into the simulation tool as summation of E_{rel} at each discretization point multiplied by mesh area (a_i) at each mesh point divided by total area per nano structure (A).

$$EF = \frac{\sum_i (E_{rel,i}^4 a_i)}{A} \quad (4-3)$$

In the approximation method described above Raman dye is assumed to be uniformly adsorbed on the sample surface and fully cover the surface. The simulation should be built to calculate the field distribution not at the surface but at a distance where molecule resides. This distance is dependent on the type of the Raman dye, for BCB 2 to 4 nm maybe a good approximation for molecule distance from the surface.

4.2 Fabrication and Analysis of Complicated Geometries

HMCL is very versatile in terms of geometrical nano-fabrication capabilities when applied with 2 axes rotation during material evaporation. In order to challenge the geometrical nano-fabrication capabilities and exploration of wide-band plasmonic resonances, nine different considerably complicated nano-geometries have been fabricated. High magnification close-up SEM images and respective deposition parameters have been reported in Figure 4.9. The same structures are fabricated on glass and on Si substrates. The deposition rate and the underlying substrate are

indicated in the information provided near the SEM images. Upon examination of structures, each is given a name to be referred to in text; based on their appearance.

Upon examination of SEM images, although very interesting structures have been fabricated, the poor quality of fabricated structures catches the eye compared to the dimers examined in the previous part. Dewetting of structures is the main reason for observed structural nonuniformities. Dewetting is a frequently used method to create low uniformity plasmonic interfaces and is conducted by annealing a thin metal film deposited on the substrate at much lower temperatures than the melting point of the metal. Since the film is too thin, it starts to separate into hemispherical nano-island. A similar process is seemingly happening in shown HMCL depositions, too. Deposition rate varied between depositions as it may be important in structural deformation by dewetting. At lower rates, deposition takes much more time, and evaporation chamber heats up a bit more due to radiation from the evaporation source. Upon examination of SEM images, it seems not to have a large impact on structure quality. Deposition rates ranging from 0.2 Å/s to 2 Å/s have been used with little indication of any effect on the resulting structure.

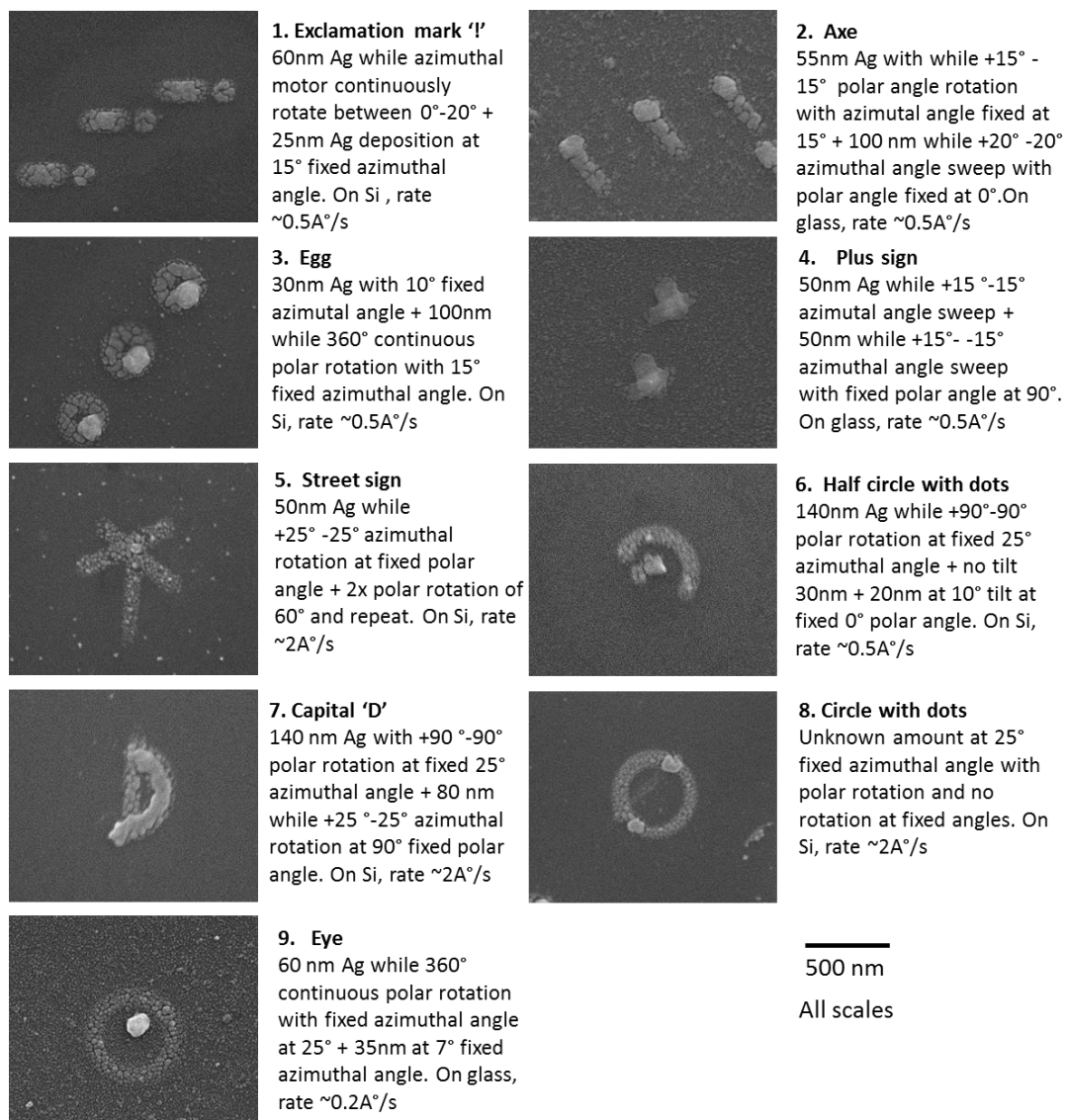


Figure 4.9. SEM images of complicated nano-structures with rotation and evaporation parameters and structure names

The total thickness of evaporated material seems to have an important effect on dewetting. Increased nonuniformities are observed when the total thickness of the structure is low. Wall thicknesses of several of the fabrications are calculated by dividing total evaporation thickness by the ratio of hole area to the resulting structure area, which has been shown in Figure 4.10. Upon examination of the figure, it can be said that structure deforming due to dewetting is increased when the thickness is below 20nm; a thickness of at least 30nm seems to get rid of dewetting completely.

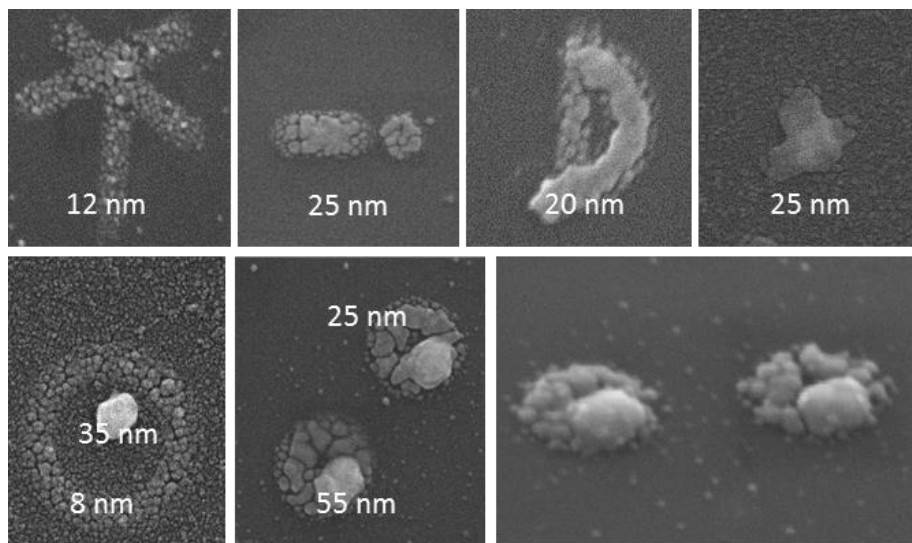


Figure 4.10. SEM image array with thicknesses of several structures

Structures fabricated on glass samples also show slight differences from their Si counterparts. Figure 4.11 shows the “exclamation mark” geometry differs a bit even though the two samples treated almost all experimental steps side by side with the same parameters. This difference may be caused due to different heat conductivities and capacities or the different adhesion properties of Si and Glass substrates.

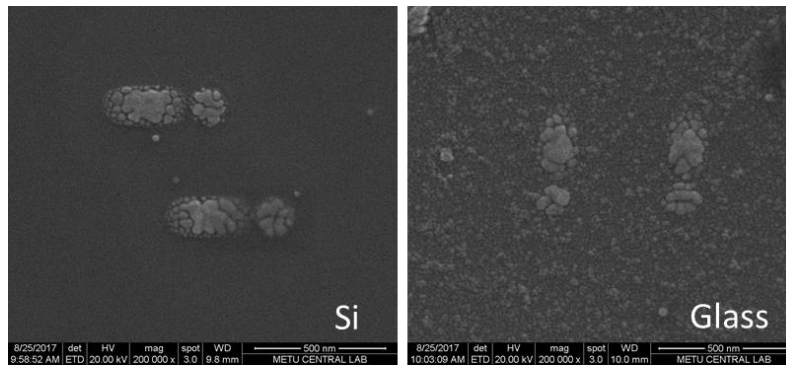


Figure 4.11. Same structure left: on Si substrate right: on glass substrate

4.2.1 Scattering Measurements

DF spectroscopy of each fabricated structure have been measured for examination of plasmonic scattering properties; some of the scattering results from simpler structures allow further analyzable scattering peaks. The scattering spectrum of the “the exclamation mark” is shown in Figure 4.12. The structure contains two plasmonic particles, and the gap between them is higher than both of the dimers examined in section 4.1; thus, little coupling between them is expected, and the total scattering cross-section should include two distinct Gaussian peaks. Gaussian peak fitting analysis made using Originlab yielded that the measured spectrum almost perfectly contains two distinct peaks from the disc and rod. The peak found to be around 650 nm is originating from the plasmonic resonance of the disc and short side of the rod, as these two have very similar dimensions, and the peak around 970nm is from the long side of the rod. A similar two-peak fit analysis is made for the scattering result of “the plus sign” structure, shown in Figure 4.13. This structure has a thicker square at the middle and two crossing arms at each orthogonal direction, the smaller peak around 750nm is supposed to result from the plasmonic resonances at the thick square middle section, and the larger and narrower peak at around 1 μ m is the resonances from the two arms of the structure.

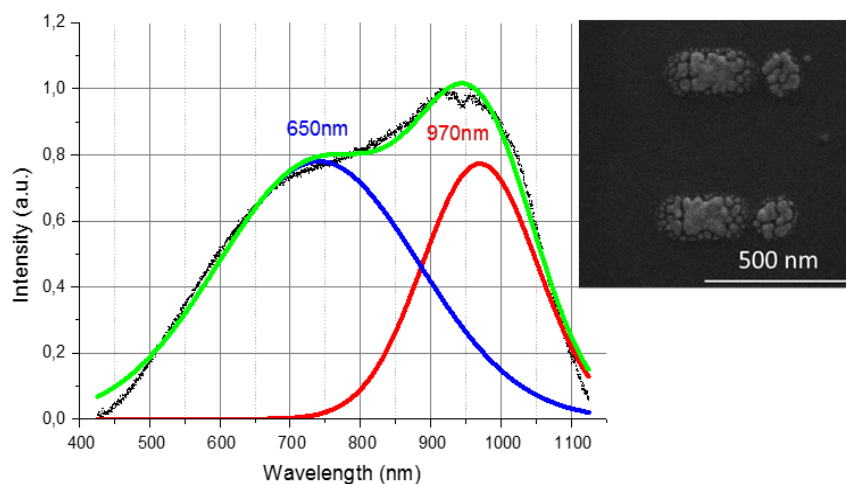


Figure 4.12. Scattering spectra of “exclamation mark” and two Gaussian peak fit analysis. Green curves show the sum of two fitted curves.

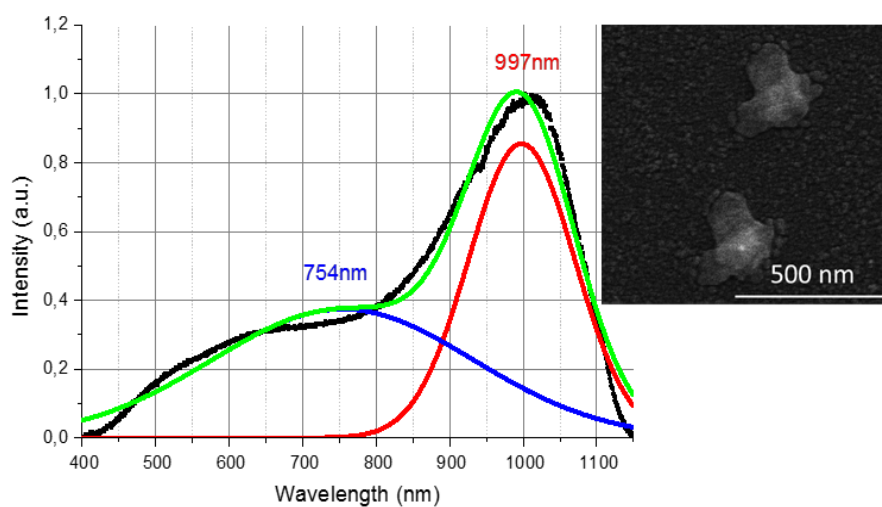


Figure 4.13. Scattering spectra of “plus sign” and two Gaussian peak fit analysis. Green curves show the sum of two fitted curves.

The measurements from “eye” structure shown in Figure 4.14, the spectrum is dominated by the peak from the thick disc inside the thin outer circle. Other structures that show wide peaks in the measurement region are “egg” and “half circle with dots”. both of their measurement results are shown in Figure 4.15. As the structures most probably more than two distinct scattering peaks and more complicated plasmonic coupling properties, peak analysis attempts were unsuccessful. However, their wide peaks may be useful for applications where wide band plasmonic scatterers are desired, such as solar cell applications. Other structures in Figure 4.9 did not show distinguishable scattering peaks at measurement range thus are not further discussed.

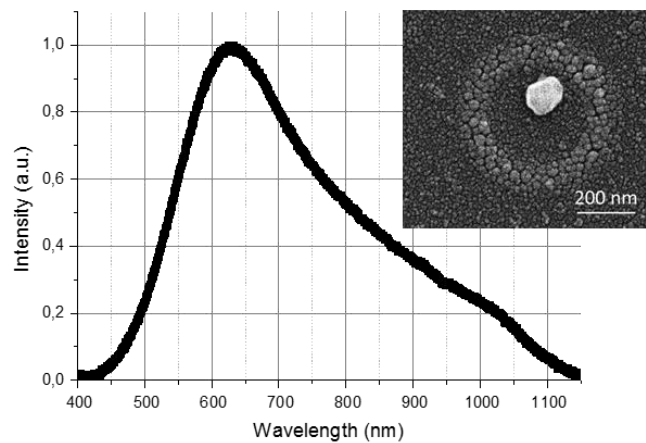


Figure 4.14. Scattering spectrum of “eye” structure

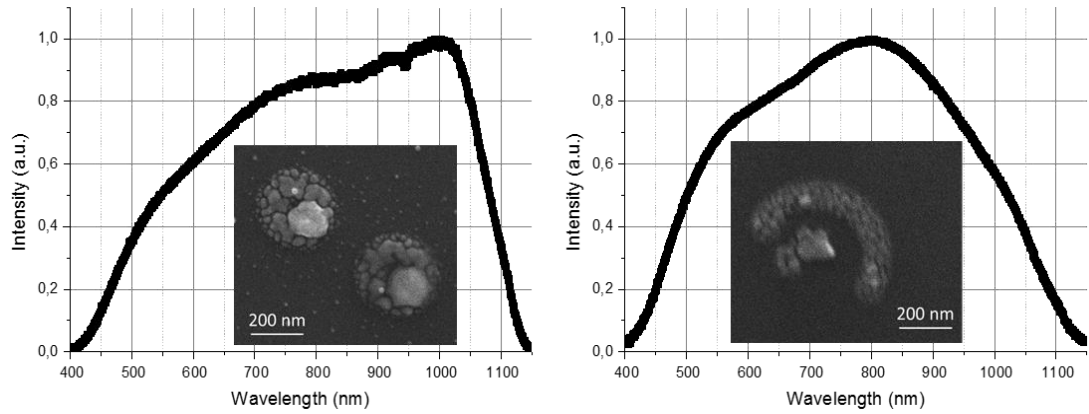


Figure 4.15. Scattering spectra of “egg” and “half circle with dots” structures.

4.2.2 Examination of Annealing

Annealing is a frequently used method to modify structural properties of metal nanostructures. It is mostly used to get rid of sharp features and nonuniformities. To observe how annealing effect the structural properties of these fabrications, several of the fabricated structures on Si substrate are annealed on a hot plate set to 210°C for 5minutes. Figure 4.16 shows SEM images of several structures before and after annealing. Symmetric and thick structures are observed to keep their shape better after annealing, annealing seems to disturb the geometry even more by increasing islands formed by dewetting for thinner structures.

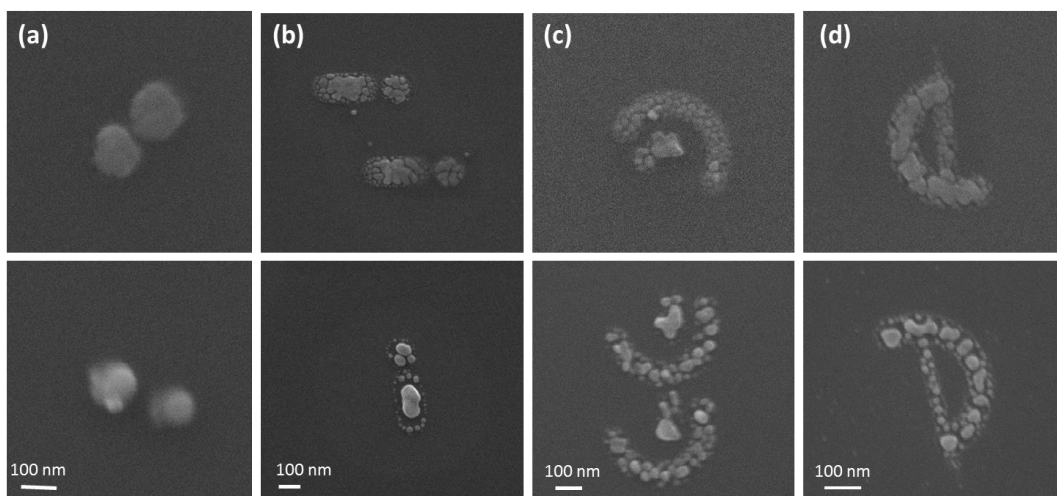


Figure 4.16. Structural effects of annealing on fabricated structures, up: before, down: after annealing

Effect of dewetting on scattering properties have been examined for dimers and “exclamation mark” fabrications. Figure 4.17 shows measurements of scattering spectrums before and after annealing for each structure. Since particle size gets smaller as seen in SEM image insets, a blueshift is observed. Change in the spectrum is more significant for the exclamation mark, but as SEM images show, structural deformation is also significant and structure is much smaller after annealing.

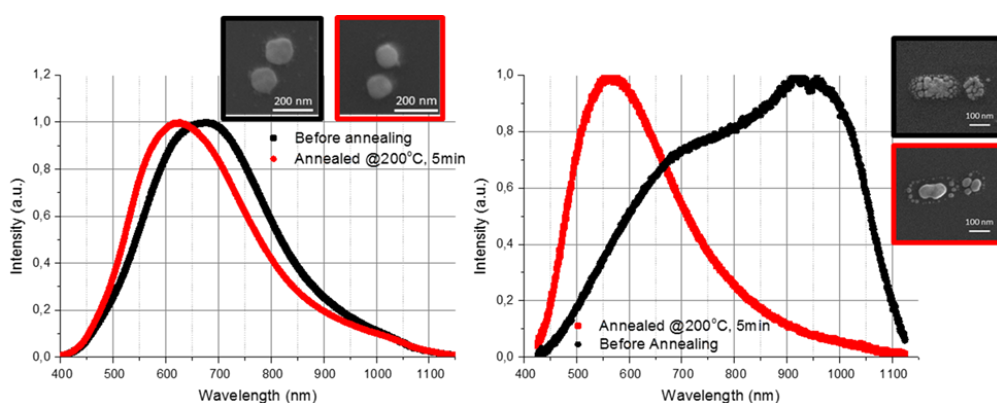


Figure 4.17. Dark field spectrum before (black) and after annealing (red), insets for respective SEM images

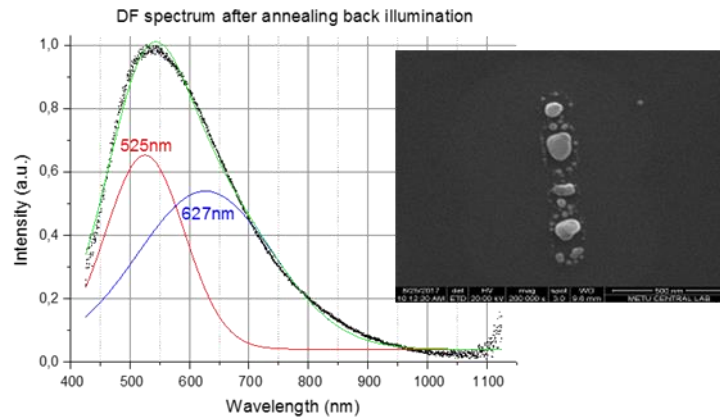


Figure 4.18. two Gaussian peak fit analysis on “exclamation mark” after annealing. Green curves show the sum of two fitted curves.

A two peak gaussian fit analysis is performed on annealed “exclamation mark” structure. When compared with same analysis before annealing shown in Figure 4.12, both peaks are blue shifted. The peak corresponding to the disc is shifted from 650nm to 525nm and the peak corresponding to the rod is shifted from 970nm to 627nm. SEM images support this behavior as the size of each structure gets smaller than the original dimensions after annealing which is the reason for blueshift in their resonance wavelength.

A contrary outcome is obtained for another dimer fabrication, this time with thicker discs of 50nm. The polarized illumination DF spectra is examined for the two discs shown in Figure 4.19, the measurements on the left is done right after the fabrication and the graph on the right measured after 210°C, 5 minutes annealing treatment. A red shift is observed in both parallel and perpendicular polarized measurements indicating overall disc diameter is increased after annealing. Moreover, comparing the parallel polarized measurements the coupling between the discs are enhanced. The inset SEM images supports the reduction in gap distance after annealing treatment.

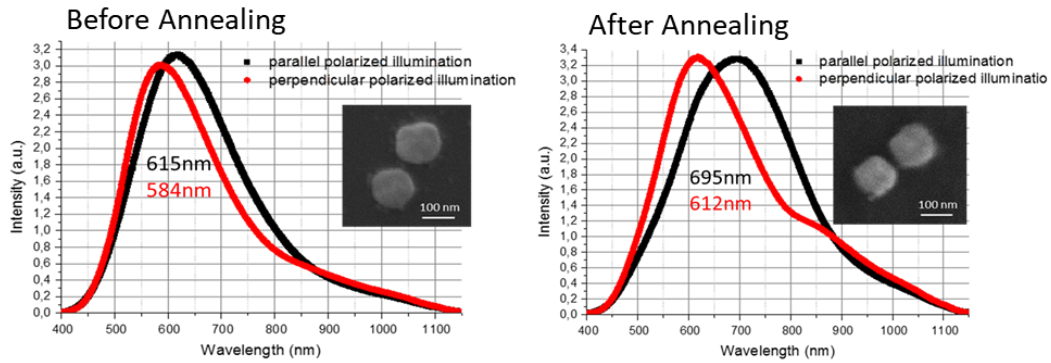


Figure 4.19. Polarized DF spectrums of a dimer fabrication with thicker discs, left: before and right: after annealing.

4.3 Preferential Scattering Calculations for Plasmon Enhanced Photovoltaics

Plasmonic nanoparticles on interfaces have been shown to radiate preferentially to the higher refractive index medium [212]. One particular paper examines the ratio of forward scattering compared to overall scattering for various simple nanoparticle geometries placed over a solar cell surface [213]. Far-field radiation mode of simulation software can be used to realize and reproduce this result. Since HMCL can be used to fabricate various geometries on interfaces, and one of the promising applications is photovoltaic surface decoration for efficiency enhancement. It has been proposed such structures could be most effective on the surfaces of thin film solar cells by increasing the effective path length of light, reducing energy escape from the active region. Mnpbem is used for calculation of the radiation pattern from structures placed on Si substrate, 3D angular far-field scattering distribution pattern for 100 nm diameter disc at 500 and 650nm wavelengths and for a sphere from left to right, respectively are shown in Figure 4.20. The radiation pattern suggests that the preferential scattering into the Si substrate is much higher than backscattering through the air side.

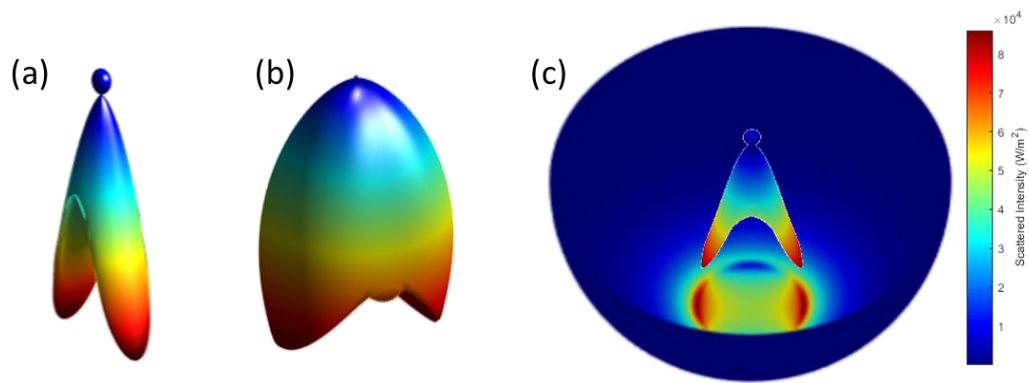


Figure 4.20. Mnpbem simulation results. 3D polar plots for angular far field scattering distribution pattern for a) 100 nm diameter sphere b) 100 nm diameter disc at 800 nm wavelength. c) Hemisphere defined at infinity for Poynting vector calculation.

With the calculation model built for far-field scattering patterns, the ratio of scattering into the substrate to total scattering can be calculated for various structures. Model is first used to reproduce the results in the paper published by Catchpole and Polman [213], in which preferential scattering ratio is calculated for Ag disc, hemisphere, and two sizes of spheres shown in the left side of Figure 4.21, same calculations performed by our model and results are shown in the right side of Figure 4.21. When compared, a very similar trend is observed; the disc with a 100nm diameter has the largest preferential scattering, followed by a 100nm hemisphere, 100nm sphere, and 150 nm sphere. Moreover, wavelength dependencies follow very similar trends. However, the values of the ratio are much higher in our simulations. The discrepancy in ratio values is thought to originate from the differences in model building. In our simulations, the structures are placed directly over the Si surface, while in the article, there is an intermediate SiO₂ layer. Another difference is the simulation method; we used a 3-dimensional Maxwell solution with the BEM method; in the paper, a 2-dimensional solution with the FDTD method is used [213].

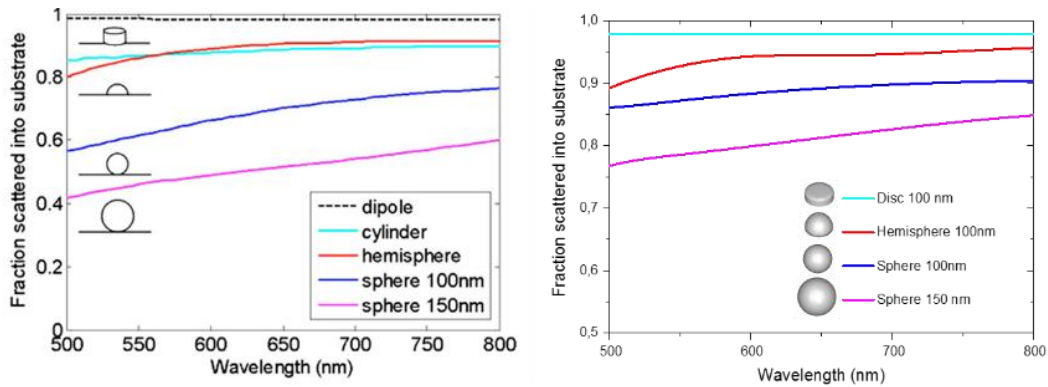


Figure 4.21. Simulation results showing fraction of incident radiation scattered into substrate for 4 different plasmonic structures. Left: simulation results acquired from [213], right: Reproduction of results by Mnpbem simulations

Using the same approach several different geometries have been examined, for geometry selection structures that can be fabricated with HMCL are preferred. Since the discs yield the highest preferential scattering ratio upon examined geometries in Figure 4.21, results obtained from different geometries have been compared to disc results. Preferential scattering ratios for Dimers of diameter 150 nm with 10 and 20 nm gap distance, Quadromers with 50nm gap between neighboring discs with diameters 100 nm and 150 nm Analyses include rods of 3 aspect ratio, cross with different geometrical aspects, split rings and ring structures. For structured that does not show symmetry two perpendicular illumination polarizations are analyzed independently.

The preferential scattering ratio results for 150 nm dimers with gap distances of 10nm and 20 nm and quadromers have been shown in Figure 4.22. The fraction scattered into substrate show similarly high values over 94% for all the structures. The disc with 100nm diameter is the winner again in this comparison. The values calculated for 150nm diameter disc and 150nm diameter dimers' perpendicular polarization results are virtually the same. Dimer gap distance change from 10nm to 20nm shows very little difference when the polarization is parallel, unlike their scattering spectra previously calculated and shown in Figure 4.4, where the plasmonic resonance peak is shown to be redshifted and get wider as the gap distance

reduced. Wider resonance peak however, may be beneficial in overall plasmonic contribution as the scattering cross-section is higher overall at a wider band of the spectrum.

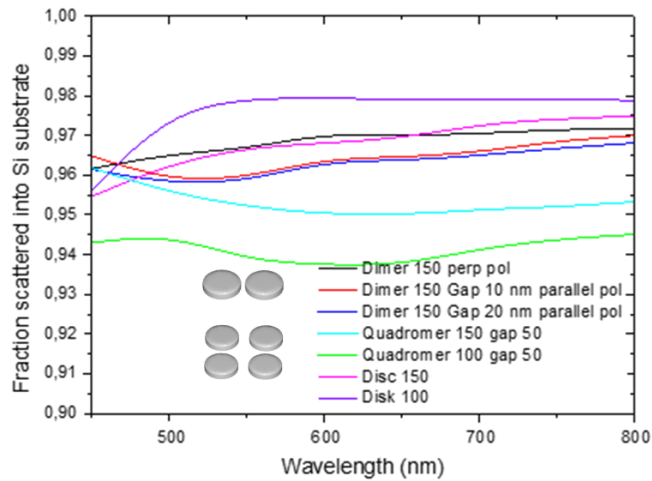


Figure 4.22. Fraction scattered into Si substrate for Dimers and quadromers

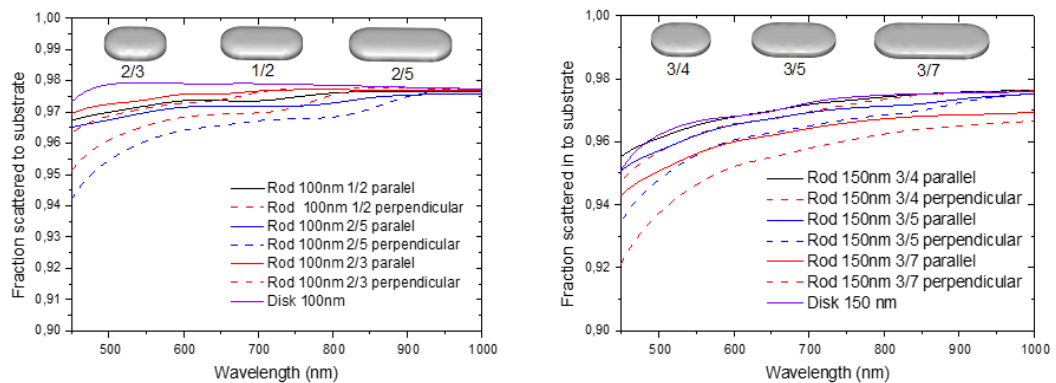


Figure 4.23. Fraction scattered into Si substrate for rods of different aspect ratio, the short axis length is left: 100nm, right: 150 nm.

The results obtained for rods are shown in Figure 4.23, in these analyses 3 different rods with varying aspect ratio, width/length values are given in insets with 3D models, are examined for 100 and 150nm widths. Similar to the dimers these structures also yield very high fractional scattering ratios. The fraction scattered into

substrate lowers as the aspect ratio getting lower and overall values are higher for 100nm width structures. The compared discs of same size, which are aspect ratio one rods, yields highest preferential scattering into Si.

Another consideration is the angular distribution of scattered light in the substrate, which is especially important for thin film solar cell applications where light escaping from thin active region before absorption is a problem. Angular distribution of scattered radiation calculations can be used to estimate how much of the scattered light will be directed into guided modes i.e., scattered with an angle above TIR. The simulation results for angular distribution of pointing vector norm inside the Si substrate at far field for a sphere and disc of diameter 100nm is shown in Figure 4.24. Comparing the two results the majority of scattered light from the sphere is directed directly below with a smaller portion is directed into guided modes, for disc higher portion of the scattered light is directed at higher angles. The poynting vector norm of the scattered light is much lower for the disc due to the off-resonance of the incident wavelength. A similar pattern is observed over a range of wavelengths indicating that disc is better at directing the scattered light into guided modes for a thin film solar cell.

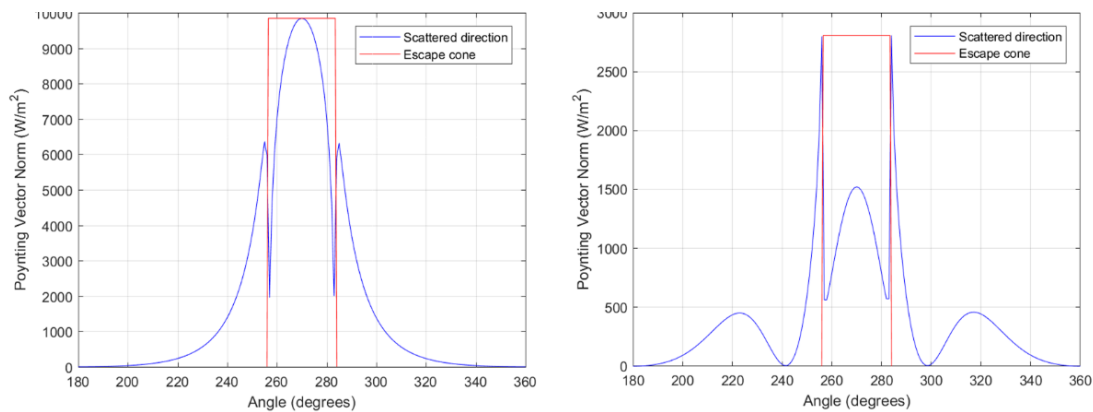


Figure 4.24. Angular distribution of pointing vector norm of scattered light inside the substrate. Left: A sphere, Right: A disc with 100nm diameter each at 500nm wavelength. Red lines indicate the TIR angle of Si/air interface

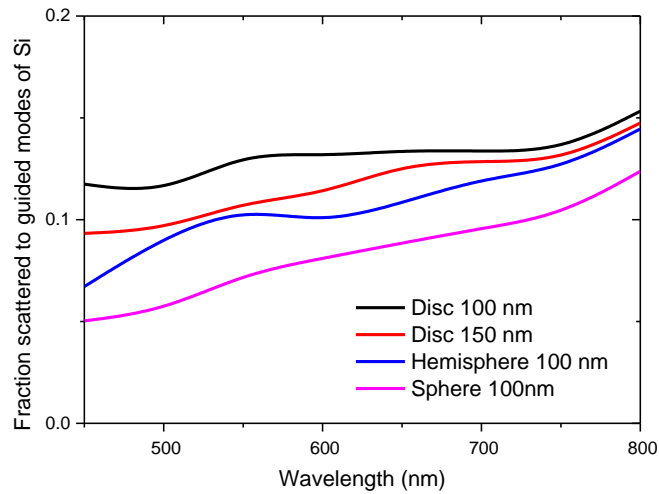


Figure 4.25. Calculation of the fraction of scattered light directed into guided modes of a thin film Si solar cell for different plasmonic structures

None of the geometries under examination seems to reach the preferential scattering ratios obtained from discs. However, this analysis does not fully indicate the overall contribution of such structures to the efficiency of a solar cell when placed on the surface. One of the important values to consider here is scattering efficiency. For example, discs examined in these analyses have their plasmonic resonance at near infrared regions shown in Figure 4.26, the resonance positions are redshifted compared to previous analyses on glass substrates due to the high refractive index Si substrate in the vicinity. While, the resonance position of a sphere of same diameter does not red-shift as much as the disc. The resonance peak position is around 550nm for a 100nm diameter Ag sphere. The wavelengths used for these analyses are out of resonance for the discs. Even if the fraction scattered into substrate values are very high, scattering efficiency of these discs are below 1 at 600nm. This means the interaction area is lower than the geometrical area and depending on surface coverage a very small portion of incident light interacts with discs in the visible region.

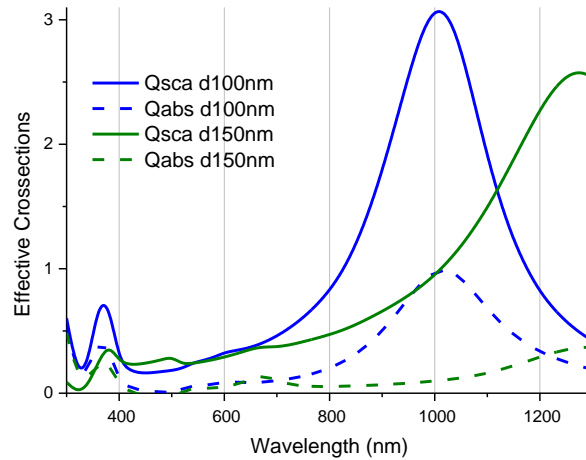


Figure 4.26. Calculated scattering and absorption efficiencies for discs on Si substrate. Blue curves are for disc diameter 100nm and green curves are for 150nm

4.4 A Model for Quantification of Plasmonic Contribution to Photovoltaics

There are many variables that should be considered when the contribution of plasmonic structures to efficiency is aimed to be calculated. A model can be used to combine these variables to quantify the overall effect of plasmonic surface scatterers to PV efficiency. When the wavelength range for calculation is determined we can incorporate scattering and absorption efficiencies, fraction scattered into PV, plasmonic path enhancement factor and surface coverage together into the model. Using this approach, for a PV surface covered with plasmonic particles, we should be able to estimate the total plasmonic contribution to the absorption at active layer. A calculation model below is proposed for thin film solar cell.

We should start with conditions that this model is valid:

- Active layer is far from particles such that near field enhancement effects do not contribute to PV absorption
- Surface and back reflector are perfectly flat
- No coupling between the structures, there can be coupling inside the analyzed structure but next structure on the surface does not interact with previous one

- Particles are randomly distributed on the surface so scattered light don't collectively interfere

Portion of incoming energy interacting with plasmonic structures (g) can be defined as;

$$g = \frac{C_{ext}}{A} \rho \gamma = Q_{ext} \rho \gamma \quad (4-4)$$

Where; C_{ext} is extinction cross-section, A is the area of the plasmonic structure, ρ is surface coverage ratio of plasmonic structures.

γ is defined as the overlapping factor. Since Q_{ext} may be much larger than 1 around resonance, it takes a value that reduces g to 1 if $Q_{ext} S$ is higher than 1 indicating a purely plasmonic interface interaction, otherwise $\gamma = 1$.

$1 - g$ portion of incoming energy does not interact with plasmonic structures, governed by Fresnel R-T coefficients of the decorated interface.

Total plasmonic absorption loss (L) and total scattered portion (S) can be calculated as;

$$L = g \frac{C_{abs}}{C_{ext}} \quad (4-5)$$

$$S = g \frac{C_{sca}}{C_{ext}} \quad (4-6)$$

Total portion scattered into substrate can be calculated using preferential scattering ratio (Ps_r) calculated in the previous section as;

$$S_{sub} = S Ps_r \quad (4-7)$$

For a c-Si PV active region with thickness in the range of 100 μm , all the light entering the substrate can be assumed to be absorbed after one pass. The plasmonic enhancement generally worked on thin film devices as the plasmonic contribution compared to uncoated case would be significantly more. For the case of a thin film device the angular distribution calculation of scattered light in substrate should be considered. The path enhancement factor can be calculated as;

$$f = \frac{\sum_{\theta_{sub}} \frac{1}{\cos(\theta_{sub})} S_{sub}(\theta_{sub})}{S_{sub}} \quad (4-8)$$

With active region thickness t and absorption coefficient α , PV absorption coefficient by plasmonics structures Abs_p and non-plasmonic absorption coefficient Abs_F after 2 passes in active region can be found using;

$$Abs_p = S_{sub} (1 - e^{-2\alpha ft}) \quad (4-9)$$

$$Abs_F = (1 - g) T_{Fresnel} (1 - e^{-2\alpha t}) \quad (4-10)$$

After 2 passes from active region the leftover energy portion $S_{leftover}$ that will incident to the interface from inside is:

$$S_{leftover} = S_{sub} e^{-2\alpha ft} + (1 - g) T_{Fresnel} e^{-2\alpha t} \quad (4-11)$$

Here, depending on the amount of leftover energy portion, calculation can be repeated again this time for light incident from the inside, the angular distribution may be ignored and most dominant angle can be used as the angle of incidence. Until the leftover energy falls a certain threshold calculation can be repeated. Adding all absorption coefficients yields total absorbed portion of incoming light. Repeating for multiple wavelengths a spectral graph of portion of energy absorbed will be obtained.

By using the internal quantum efficiency (IQE) of the cell total efficiency can be predicted. The obtained result can be compared to the case without plasmonic nanoparticles and total contribution of plasmonic nanoparticle to overall efficiency can be calculated. For a case with conventional thick solar cell complete absorption after 2 passes can be assumed, equation (4-7) would be enough to obtain total absorption due to plasmonic scattering, which can be combined with Fresnel transmission thus a simpler solution would be obtained.

For solar cell surface decoration, the plasmonic enhancement should be integrated over the wavelength region of the device, weighted over the solar spectrum. The equation (4-12) can be used to calculate the overall plasmonic enhancement for Si based solar cells both for experimental results and for calculations [195].

$$\eta_{plasmonic} = \frac{\int_{300}^{1200} A_{s+np}(\lambda) AM1.5 d\lambda}{\int_{300}^{1200} A_s(\lambda) AM1.5 d\lambda} \quad (4-12)$$

Where AM1.5 is the normalized solar spectrum on Earth's surface, $A_s(\lambda)$ is the absorption of Si device without plasmonic surface decoration and $A_{s+np}(\lambda)$ is the absorption of Si device with plasmonic surface decoration.

4.4.1 Comparison of Basic Plasmon Geometries at Resonance

For comparison of different geometries, a simpler approach deriving from this model is used. A completely plasmonic case can be examined by using resonant particles at a specific wavelength with surface coverage chosen such that $g=1$. Resonance position is chosen for purely plasmonic interaction analysis, at of resonance illumination extinction efficiency falls below 1 quickly making purely plasmonic analysis impossible even with very high surface coverages. By conducting the analysis this way maximum contribution to PV efficiency due to plasmonic structures can be calculated. The surface this time kept more realistic by adding a 10nm SiO₂ layer on top of Si substrate as plain Si substrates quickly oxidizes until a

natural oxide layer is formed when exposed to atmosphere. As a first example 532 nm is chosen for analysis. The Ag disc diameter that will resonate at 532nm when placed on 10nm thick SiO₂ on Si substrate found by several calculations with a rough and fine diameter span, the graphs of scattering spectra calculations are shown in Figure 4.27. 71 nm is found to be resonant at this wavelength.

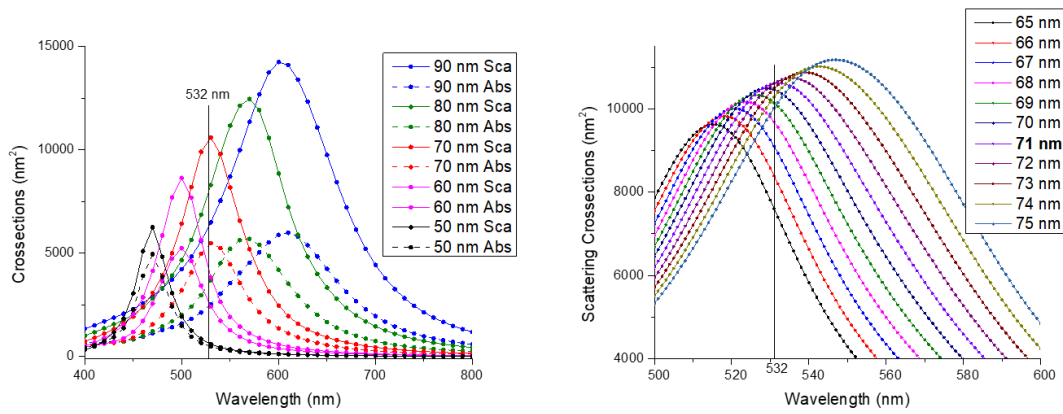


Figure 4.27. Scattering cross-section calculations for finding the diameter of the disc resonant at 532nm on 10 nm thick SiO₂ on Si substrate

The angular scattering distribution is calculated for the disc and polar distribution graph is shown in Figure 4.28. The calculated parameters are given in Table 2.

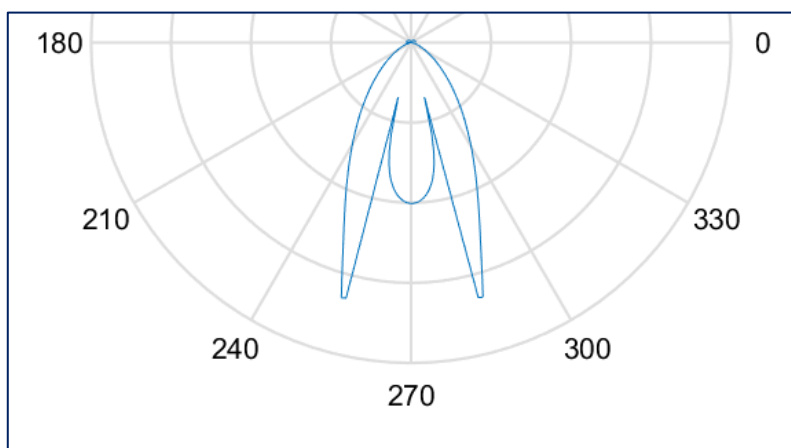


Figure 4.28. Angular distribution of scattered radiation for Ag disc of diameter 71nm on 10 nm thick SiO₂ on Si at 532 nm illumination

Table 2. Calculated values for Ag disc of diameter 71nm on 10 nm thick SiO₂ on Si at 532 nm illumination

Extinction Cross-section	C_{ext}	16203 nm ²
Absorption Cross-section	C_{abs}	5495 nm ²
Scattering Cross-section	C_{sca}	10709 nm ²
Projected area	A	3959 nm ²
Preferential scattering ratio	Psr	0.962
Surface coverage	$\rho = \frac{A}{C_{ext}}$	0.244
Fraction scattered into substrate	$S_{sub} = Psr \frac{C_{sca}}{C_{ext}}$	0.636
Fresnel Transmission	$T_{Fresnel}$	0.624
Plasmonic improvement	$S_{sub} - T_{Fresnel}$	1.2 %

With similar approach an Ag sphere with 195nm diameter is found to be resonant at 532 nm wavelength. The angular scattering distribution is calculated for the disc and polar distribution graph is shown in Figure 4.29. The calculated parameters for this case are given in Table 3.

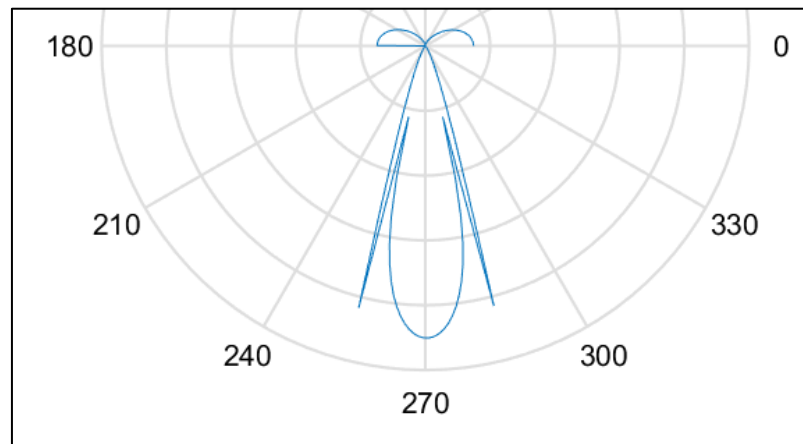


Figure 4.29. Angular distribution of scattered radiation for Ag sphere of diameter 195 nm on 10 nm thick SiO₂ on Si at 532 nm illumination

Table 3. Calculated values for Ag sphere of diameter 195 nm on 10 nm thick SiO₂ on Si at 532 nm illumination

Extinction Cross-section	C_{ext}	307360 nm ²
Absorption Cross-section	C_{abs}	35667 nm ²
Scattering Cross-section	C_{sca}	303790 nm ²
Projected area	A	29850 nm ²
Preferential scattering ratio	Psr	0.688
Surface coverage	$\rho = \frac{A}{C_{ext}}$	0.097
Fraction scattered into substrate	$S_{sub} = Psr \frac{C_{sca}}{C_{ext}}$	0.68
Fresnel Transmission	$T_{Fresnel}$	0.624
Plasmonic improvement	$S_{sub} - T_{Fresnel}$	5.6 %

Both results indicate an improvement compared to the Fresnel case where PV surfaces are empty. For the case of disc even Psr value is much higher than the case with spherical particles similar to the results shown in Figure 4.21. overall improvement due to plasmonic scattering is higher for spherical particle when both are analyzed in resonance wavelength. This indicates Psr calculation by itself is not enough to predict possible plasmonic contribution. The surface coverage required for purely plasmonic interaction is also much higher 24.4% in the case of disc compared to 9.7% for sphere. These differences may be attributed to size difference, much higher extinction, scattering and absorption cross-section is actually due to larger size of spherical particle which is expected from the equations shown in equations (2-33) and (2-34). As scattering cross-section scales with the 6th power while absorption cross-section scales with 3rd power of particle diameter, scattering cross-section to absorption cross-section ratio is also much higher for the case of the sphere, reducing plasmonic absorption loss.

Another set of calculations for Ag and Au discs resonant at 1000nm are reported in Table 4. The maximum plasmonic contribution calculated for Ag disc is calculated

as 9.5% while Au disc only contributes up to 0.5%. Although the Ps_r values are equal at 96.6% the reduced contribution of Au disc is due to increased C_{abs}/C_{ext} ratio making plasmonic absorption losses more prominent.

Table 4. Calculated values for Ag disc of diameter 190 nm and Au disc of diameter 160 nm on 10 nm thick SiO₂ on Si at 1000 nm illumination

	190 nm Ag disc	160 nm Au disc
C_{ext}	49196 nm ²	37287 nm ²
C_{abs}	9695 nm ²	10784 nm ²
C_{sca}	39501 nm ²	26503 nm ²
A	28353 nm ²	20106 nm ²
Ps_r	0.966	0.966
ρ	0.576	0.539
S_{sub}	0.776	0.686
$T_{Fresnel}$	0.681	0.681
$S_{sub} - T_{Fresnel}$	9.5 %	0.5 %

Table 5. Comparison of the absorption contribution results for all four analyzed geometries

Geometry	Ag Disc	Ag Sphere	Ag Disc	Au Disc
Diameter	71 nm	195 nm	190 nm	160 nm
Calculation wavelength	532 nm	532 nm	1000 nm	1000 nm
Absorption Contribution	1.2%	5.6%	9.5 %	0.5 %

Results shown in Table 5 indicate that the plasmonic structures have a great potential as effective surface scatterers for photovoltaic devices at their resonance. All four different calculations reported show improvement compared to Fresnel case with no anti-reflective surface coating.

4.4.2 Broadband Calculations

Next step in analysis is calculations at multiple spectral positions, off-resonance behavior can be observed. For simplicity a relatively small band spanning 500 to 800 nm wavelengths is chosen.

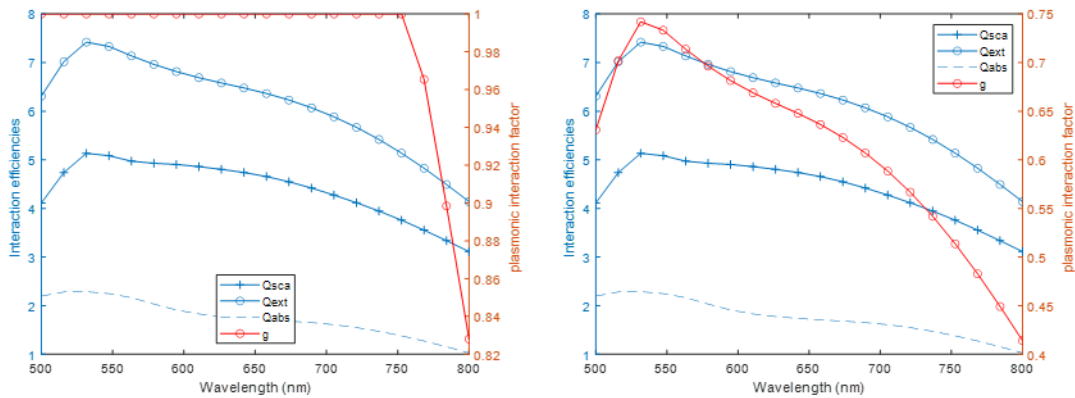


Figure 4.30. Scattering, absorption and extinction efficiencies and plasmonic interaction factor calculations for 200nm Au Sphere. Left: surface coverage 20%, right: surface coverage 10%

The model first applied to an Au nanosphere of diameter 200nm, placed 4nm above Si substrate. Scattering, absorption and extinction efficiencies with the calculated “plasmonic interaction factor”, g is shown in Figure 4.30. Left side for 20% and right side is for 10% surface coverages. At 20% surface coverage “ g ” saturates to 1 at wavelengths below 770nm. This means the plasmonic interaction is too strong for the surface coverage. We can say that the surface is so densely populated that plasmonic interaction dominates almost all the reflection-transmission dynamics. In the right picture when the surface coverage is 10%, “ g ” reaches a maximum value of 0.75. This the plasmonic interactions and Fresnel equations governs the transmission into the substrate together.

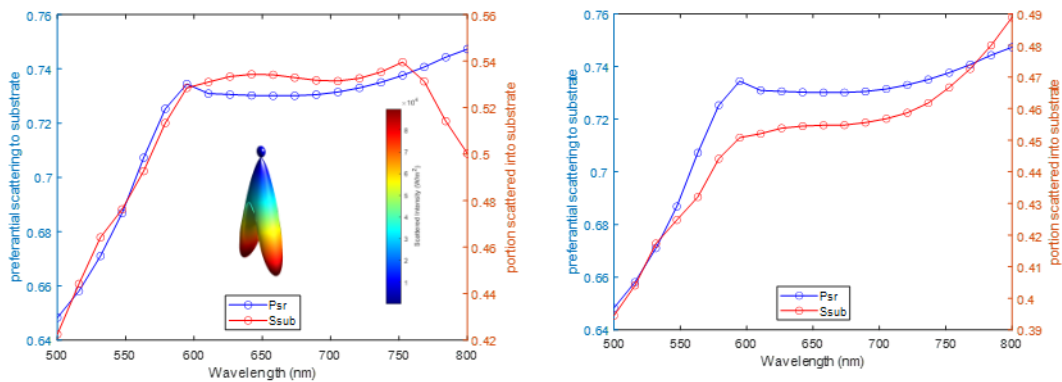


Figure 4.31. Preferential scattering to substrate and total portion scattered into substrate calculations for 200nm Au sphere. Left: surface coverage 20%, right: surface coverage 10%. Inset: angular scattering distribution at 800nm

Results for preferential scattering into the substrate, plotted together with total portion of incoming light into substrate is shown in Figure 4.31. While the total portion scattered into substrate is higher at 20% surface coverage, indicating an improvement due to Au spheres on the surface.

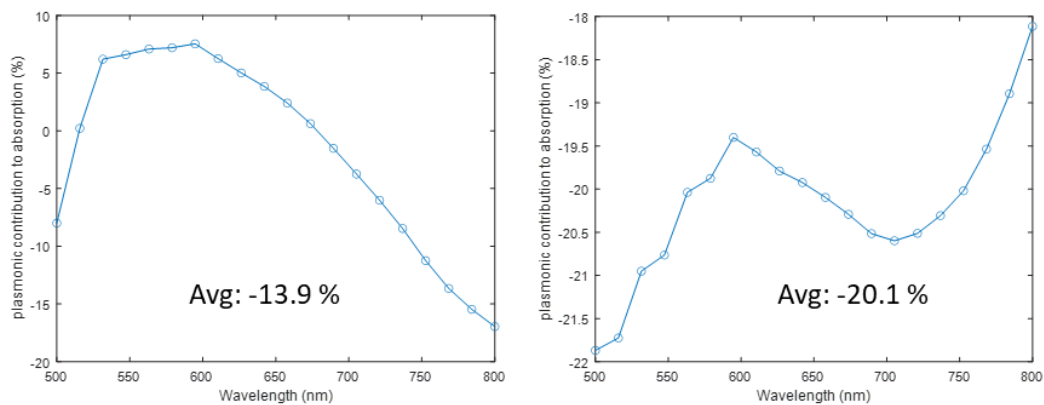


Figure 4.32. Plasmonic contribution to absorption calculations for 200nm Au sphere. Left: surface coverage 20%, right: surface coverage 10%

In Figure 4.32, spectral graph of total plasmonic contribution is calculated and plotted. The average contribution value is calculated by averaging the spectral distribution of contributions from 500 to 800nm. When the average effect is considered, the 200 nm Au sphere hinders the overall transmission of the substrate yielding lower overall efficiencies. However, we can see at 20% surface coverage positive contribution is observed from 525nm to 675nm. The effect is completely negative for 10% surface coverage at all examined wavelengths.

Same calculations are conducted for a 200 nm silver sphere this time. Interaction efficiencies are shown in the left side of Figure 4.33, The scattering efficiency is quite high, around 8, at 500nm. The plasmonic interaction factor “g” is shown with a surface coverage of 15%. The total plasmonic contribution graphs shown in the right of the same figure. The contribution is over 20-25% at 500 nm while it falls below zero quickly at around 540nm.

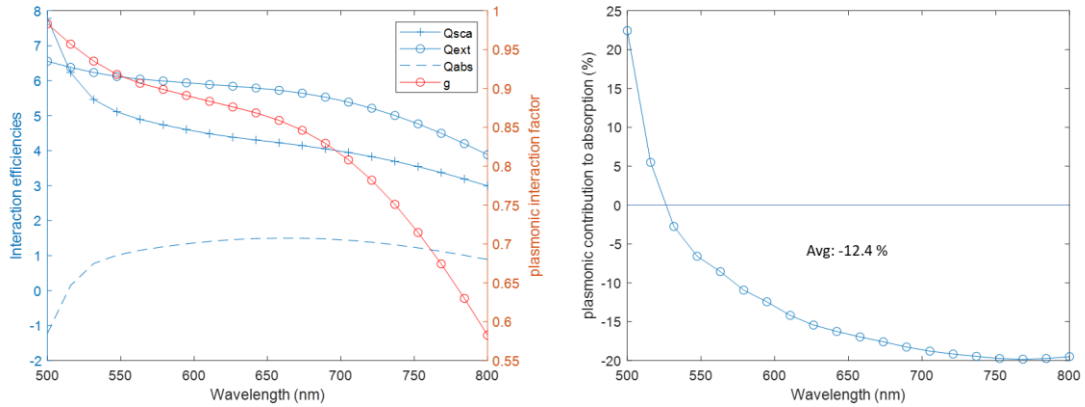


Figure 4.33. Left: Scattering, absorption and extinction efficiencies and plasmonic interaction factor calculations. Right: Plasmonic contribution to absorption calculations for 200nm Ag sphere with 15% surface coverage.

Next the same calculations are conducted for an Au disc of diameter 100nm low interaction efficiencies required very high surface coverages. In Figure 4.34 calculations at 80% surface coverage is shown. At this surface coverage the overall

plasmonic contribution become positive in between 600-700nm with a peak value over 10% around 650nm. Overall contribution between 500 to 800 nm is found to be negative at -5.5%.

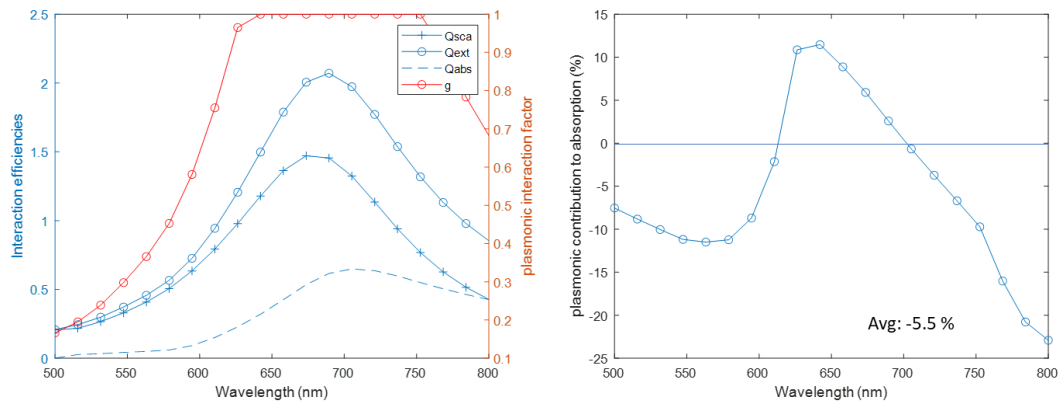


Figure 4.34. Left: Scattering, absorption and extinction efficiencies and plasmonic interaction factor calculations. Right: Plasmonic contribution to absorption calculations for 100nm Au disc with 0.8 surface coverage.

Same calculations for a 100nm diameter Ag disc are shown in Figure 4.35. The plasmon resonance position in the middle of calculation wavelengths is promising. A surface coverage value is chosen such as 40%, such that “g” is 1 at peak of the resonance. The plasmonic contribution to overall absorption peaks to positive values with maximum value over 15%. Still the average contribution is negative at -5.7%

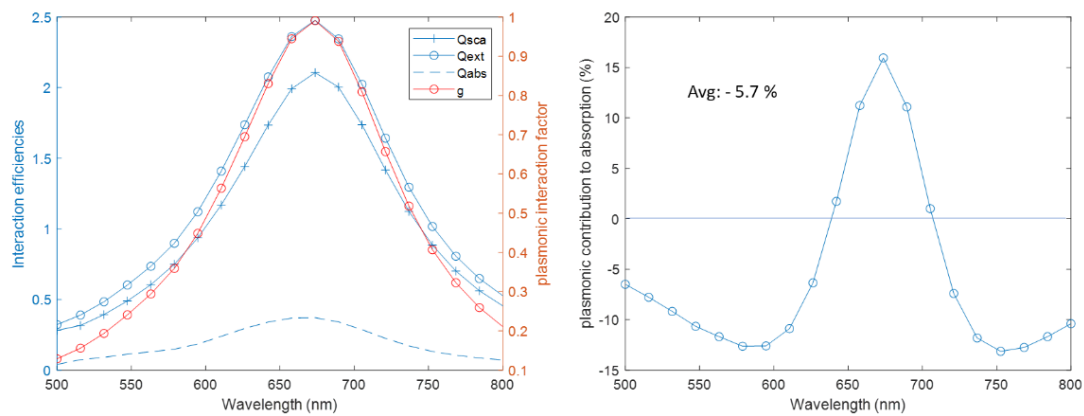


Figure 4.35. Left: Scattering, absorption and extinction efficiencies and plasmonic interaction factor calculations. Right: Plasmonic contribution to absorption calculations for 100nm Ag disc with 0.4 surface coverage.

When the same calculations are made at 70 % surface coverage the obtained plasmonic contribution to surface coverage is shown in Figure 4.36. This coverage value yielded the best contribution to overall absorption. With average is positive for the first time at 1%.

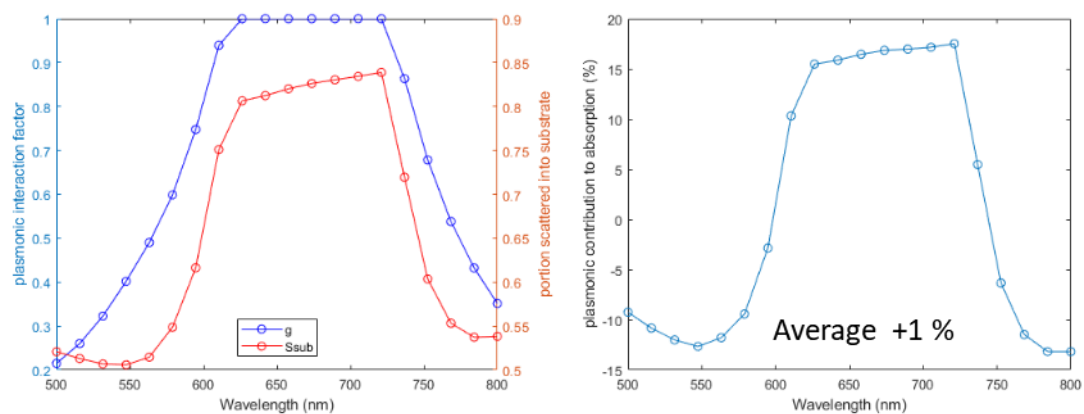


Figure 4.36. Plasmonic contribution to absorption calculations for 100nm Ag disc with 70% surface coverage.

Results shown in Figure 4.36 is significant as it is the first observation of a broader band overall contribution with average value above zero. However, practically 70% surface coverage is not very realistically achievable without plasmon-coupling effects, which were assumed to be ignorable in the model definition.

The relation of average plasmonic absorption contribution in the same wavelength range but with varied surface coverage can be calculated. The average plasmonic contribution to the transmission is calculated for 200nm Au (black) and Ag spheres (red) and 100nm Au (blue) and Al (pink) discs, is shown in Figure 4.37. All of these structures are found to hinder the overall transmission between the wavelengths 500 to 800nm for any surface coverage.

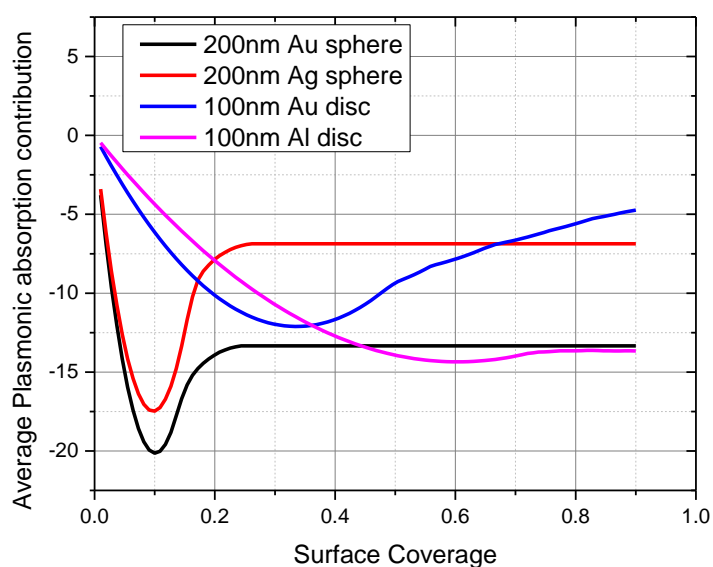


Figure 4.37. Average plasmonic contribution to PV absorption plotted against surface coverage for the analyzed nanostructures.

Next the most promising structure, the Ag discs are examined using the same calculation but with various diameters around 100 nm. The results are shown in Figure 4.38. The averaged contributions this time reaches positive values at higher

surface coverages for 100, 110 and 120 nm diameter discs. From which the 100nm diameter one seems to be slightly better than the others.

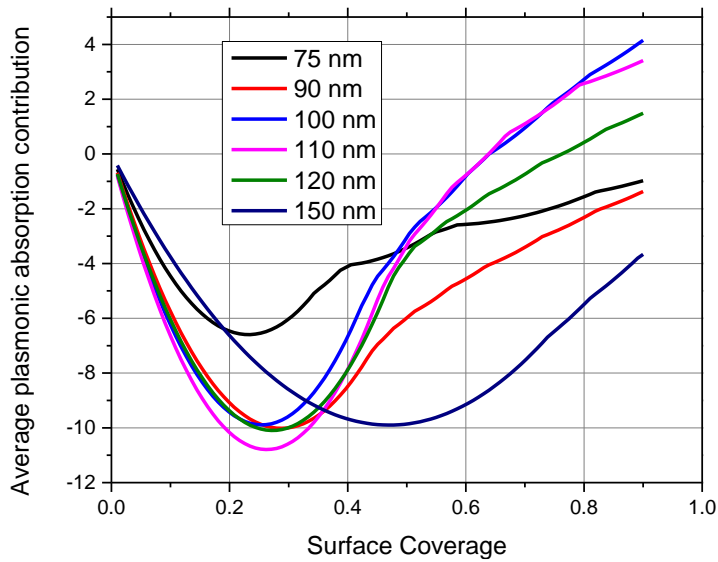


Figure 4.38. Average plasmonic contribution to PV absorption plotted against surface coverage for Ag discs of various diameters.

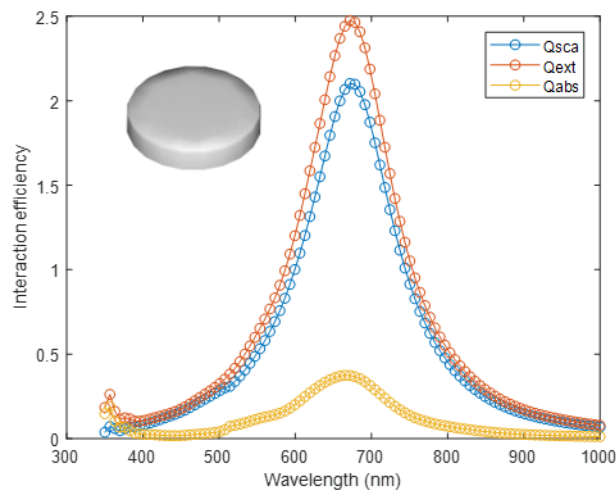


Figure 4.39. Interaction efficiencies of a 100nm diameter Ag disk placed on Si substrate

The interaction efficiencies of a 100nm Ag disc is shown in Figure 4.39, it has a very elegant resonance peak at 670nm with high scattering to absorption ratio with above one extinction efficiency in the range of 600 to 800nm. Plasmon resonance is obviously an indication the how these particles will perform as scatterers on the surfaces of PV devices. Still, almost all the examines structures have their resonance peaks in the range between 500-800nm, it should be noted that better overall contribution compared to other materials and geometries does not entirely originates from interaction efficiencies.

In many cases plasmonic structures reduce total transmission thus negatively effecting the overall efficiency. It is important to note that the calculations conducted at dipolar resonant wavelengths which is the most prominent resonance but spectrally the narrowest in general. Higher order resonances may also be implemented. At off-resonance wavelengths plasmonic scatterers may still contribute as the scattering cross-sections will still be considerably larger than absorption cross-sections. Plasmonic absorption is the main problem that need to be minimized, however absorption cross-section also peaks at resonance frequencies for small structures. Thus, we should seek for structure geometries that have a high scattering to absorption ratios.

One can discuss the case where an anti-reflective (AR) coating applied on the surface before plasmon decoration, which would highly increase the Fresnel transmission (over 95%), the plasmonic scatterers only hinders total transmission into the substrate in this case. This argument is totally valid when an efficient AR coating applied to a thick PV device. For the case of thin film photovoltaics; however, the plasmonic scatterers may still be beneficial by light trapping by directing light to guided modes and reducing escape of unabsorbed light by secondary interactions. Moreover, single band detectors also can benefit from such scatterers on the surface. An effective calculation procedure developed in this work is crucial for determination of exact effect connecting both geometry of the structures and surface distribution. The model proposed in this section can be used for analysis of this effect for much wider range of structures on various PV devices. Moreover, original model

includes thin film PV devices also. The calculations analyses and discussions made here are preliminary compared to what is possible. The results from such a small set of different geometries showing such promising results indicates that it is not far-fetched to think that a better geometry can be found.

CHAPTER 5

CONCLUSION

Plasmonics, a captivating area of nanotechnology research, explores the interaction between light and metal nanostructures, presenting fascinating applications across various scientific fields, from chemistry to biology. Devices incorporating plasmons have found widespread applications in both industrial and fundamental scientific contexts due to their interesting optical interaction and response characteristics.

The plasmonic interaction can be explained as the response of metallic free conduction band electrons to an external electric field. Externally driven electrons oscillations produce an optical response that is highly dependent on geometry, size, material, and nanometer scale features of the metal structure, when the electron oscillation frequency matches the geometry, resonances occur at particular frequency bands resulting enhanced optical response. 3 primary outcomes of this response are scattering, absorption and electric field confinement. Fine-tuning this optical response outcomes requires complete control on nanoscale features which allows light manipulation both at nanoscale and macroscale with properties not achievable with conventional optical components.

Advancements in plasmonics hinge on collaborative efforts across three domains: fabrication, measurements, and simulations. In this thesis an all in one approach for manipulation of plasmonic response is used with simultaneous studies in all three of these domains.

The chosen nano-fabrication method, Hole Mask Lithography (HML), enables large-area compatibility and diverse geometric possibilities for fabricating metal nanostructures. The method is successfully optimized in our laboratories and used for numerous fabrications from simple to complex geometries of metal nanostructures. The experiments involved the use various hole sizes both controlled

by colloidal nanosphere size and mask layer deposition procedure, experiments and findings about hole size control and manipulation are reported. For fabrication of complicated geometries, an evaporation chamber with two-axis sample rotation capabilities has been utilized, software modifications made it possible to preprogram complicated movements using CNC control system. Together with evaporation rate and hole to substrate distance, sample holder movements calculated and preprogrammed for fabrication of any possible geometry.

The random surface distribution of nano structures fabricated with HML is addressed for improvement, one of the possible improvements proposed is enabling periodic structuring. For this purpose, new strategies for controlling the surface distribution of nano geometries have been proposed and investigated. One of these proposals was the interference lithography (IL). Incorporating IL to HML is investigated in detail by proposal of a procedure and testing. It has been concluded that the IL can be used for hole preparation which enables dense periodic nano-structuring capabilities to HML. The new method is named hole mask interference lithography (HMIL).

The fabrication method HML overall is seen as a promising lithographic approach for nanoscale structuring in terms of throughput. In order to fully utilize an advanced form of HML as a fabrication technology, this research may be helpful to increase the production diversity through it. The outcomes of our efforts have broadened the spectrum of structures producible through HML. It is anticipated that the significance of HML will gather greater more recognition among researchers and even by industry in the future, especially in plasmonic research and applications, making it a widely employed nanofabrication method.

Numerical calculations are the backbone of successful experiments results. In this work full 3D Maxwell's equations solved at nanoscale with BEM and FEM methods. Correct strategies and physical grounds that should be cared in model building for obtaining physically correct results are discussed. The package programs, Mnpbem toolbox in Matlab and Comsol Multiphysics are used in application of these numerical methods. Discussions about these programs include; capability tests,

comparisons, advantages and some of the shortcomings. Considerations about common problems that are faced during model building are also discussed. By matching the results from two different computation methods, errors are minimized. By matching the modelled conditions to the experimental conditions, a good agreement has been observed. This validates the reliability of simulations to lead the experiments. Simulations allowed further examination of each investigated phenomena without need for further experimentation. Each analysis backed up by corresponding simulations which enables more accurate discussions.

The plasmonic response characteristics of plasmonic nanostructures are explored through various fabrications, measurements and numerical analyses. Plasmonic coupling of closely spaced disc dimers is shown both experimentally and numerically. SERS enhancement properties of fabricated dimers are investigated, results of simulations are compared with the experimentally obtained values. It has been found that for SERS, even though hot-spots occur at small and sharp features and small interparticle gaps, the total hot-spot area and distribution is also important and should be considered in overall electromagnetic enhancement factor calculations.

A promising application for plasmonic nanostructures is front surface decoration of photovoltaics. This application is investigated by reproducing the results of a paper from the literature by calculating angular scattering distributions of several nanoparticle geometries. A wider range of plasmonic geometries are investigated. It has been found that a simple disc is the most efficient MNP geometry for directing the scattered light into the active region; however, the ratio of substrate scattering is not the only contribution; total interaction efficiency of the plasmonic structures and their overall surface coverages play an important role for plasmon enhanced photovoltaics.

A description for quantification of overall plasmonic contribution to the efficiency of a PV device including the surface coverage is absent in the literature. A model for quantification of plasmonic contribution including surface coverage and plasmonic

interaction efficiencies has been invented. The quantification model is novel to the literature and is an important addition to the plasmonic solar cell development research. Roughly 150 papers are published in this field annually [214].

The model applied to several plasmonic geometries placed on flat Si substrate through BEM simulations. Spheres and discs made of Ag, Au and Al are investigated. It is shown that the enhancement of PV response can be tuned for a specific frequency, and from the set of analyzed nanoparticles up to 25 % efficiency enhancement at single band are observed. Broadband calculations between 500-800nm show a negative overall impact for most of the tested geometries at various surface coverages however Ag disc with 100nm diameter yielded up to 4 % average enhancement.

Through the studies many ideas have been discussed, some of these are tested turned out to be successful but some was not further pursued, for all of them however, comprehensive discussions and proposed solutions on experimental and numerical methods are provided. These approaches and considerations can help future researchers better grasp and overcome the similar difficulties through their studies.

In the vast field of nano-photonics research and development, the studies of this thesis are at best tiny, but together with numerous works from other researchers each addressing different problems, build up the field to its glory for technological developments of modern age of human era.

REFERENCES

- [1] “Lycurgus Cup,” *Wikipedia*. Aug. 21, 2023. Accessed: Oct. 07, 2023. [Online]. Available: https://en.wikipedia.org/w/index.php?title=Lycurgus_Cup&oldid=1171570592
- [2] “drinking-cup | British Museum,” The British Museum. Accessed: Oct. 07, 2023. [Online]. Available: https://www.britishmuseum.org/collection/object/H_1958-1202-1
- [3] M. Faraday, *Experimental Relations of Gold (and Other Metals) to Light*. Royal Society of London, 1857.
- [4] R. Zsigmondy, *Colloids and the ultramicroscope: a manual of colloid chemistry and ultramicroscopy*. J. Wiley & sons, 1909.
- [5] G. Mie, “Beiträge zur Optik trüber Medien, speziell kolloidaler Metallösungen,” *Ann. Phys.*, vol. 330, no. 3, pp. 377–445, 1908, doi: 10.1002/andp.19083300302.
- [6] M. L. Brongersma and P. G. Kik, *Surface Plasmon Nanophotonics*. Springer, 2007.
- [7] C. D. Geddes, Ed., *Reviews in Plasmonics 2015*, vol. 2015. in *Reviews in Plasmonics*, vol. 2015. Cham: Springer International Publishing, 2016. doi: 10.1007/978-3-319-24606-2.
- [8] R. W. Wood, “XLII. On a remarkable case of uneven distribution of light in a diffraction grating spectrum,” *Lond. Edinb. Dublin Philos. Mag. J. Sci.*, vol. 4, no. 21, pp. 396–402, Sep. 1902, doi: 10.1080/14786440209462857.
- [9] R. H. Ritchie, E. T. Arakawa, J. J. Cowan, and R. N. Hamm, “Surface-Plasmon Resonance Effect in Grating Diffraction,” *Phys. Rev. Lett.*, vol. 21, no. 22, pp. 1530–1533, Nov. 1968, doi: 10.1103/PhysRevLett.21.1530.
- [10] D. Pines, “Collective Energy Losses in Solids,” *Rev. Mod. Phys.*, vol. 28, no. 3, pp. 184–198, Jul. 1956, doi: 10.1103/RevModPhys.28.184.
- [11] M. Fleischman, P. J. Hendra, and A. J. McQuillan, “Surface-enhanced Raman scattering from silver particles on polymer-replica substrates,” *Chem Phys Lett*, vol. 26, p. 123, 1974.
- [12] T. von Foerster, “Surface-enhanced Raman effect,” *Phys. Today*, vol. 33, no. 4, pp. 18–20, Apr. 1980, doi: 10.1063/1.2914014.
- [13] T. W. Ebbesen, H. J. Lezec, H. F. Ghaemi, T. Thio, and P. A. Wolff, “Extraordinary optical transmission through sub-wavelength hole arrays,” *Nature*, vol. 391, no. 6668, Art. no. 6668, Feb. 1998, doi: 10.1038/35570.
- [14] L. Martín-Moreno *et al.*, “Theory of Extraordinary Optical Transmission through Subwavelength Hole Arrays,” *Phys. Rev. Lett.*, vol. 86, no. 6, pp. 1114–1117, Feb. 2001, doi: 10.1103/PhysRevLett.86.1114.
- [15] S. A. Maier, M. L. Brongersma, P. G. Kik, S. Meltzer, A. a. G. Requicha, and H. A. Atwater, “Plasmonics—A Route to Nanoscale Optical Devices,” *Adv. Mater.*, vol. 13, no. 19, pp. 1501–1505, 2001, doi: 10.1002/1521-4095(200110)13:19<1501::AID-ADMA1501>3.0.CO;2-Z.

- [16] E. Ozbay, “Plasmonics: Merging Photonics and Electronics at Nanoscale Dimensions,” *Sci. New Ser.*, vol. 311, no. 5758, pp. 189–193, 2006.
- [17] M. Li, S. K. Cushing, and N. Wu, “Plasmon-enhanced optical sensors: a review,” *Analyst*, vol. 140, no. 2, pp. 386–406, Dec. 2014, doi: 10.1039/C4AN01079E.
- [18] A. B. Taylor and P. Zijlstra, “Single-Molecule Plasmon Sensing: Current Status and Future Prospects,” *ACS Sens.*, vol. 2, no. 8, pp. 1103–1122, Aug. 2017, doi: 10.1021/acssensors.7b00382.
- [19] C. Caucheteur, T. Guo, F. Liu, B.-O. Guan, and J. Albert, “Ultrasensitive plasmonic sensing in air using optical fibre spectral combs,” *Nat. Commun.*, vol. 7, no. 1, Art. no. 1, Nov. 2016, doi: 10.1038/ncomms13371.
- [20] D. J. de Aberasturi, A. B. Serrano-Montes, and L. M. Liz-Marzán, “Modern Applications of Plasmonic Nanoparticles: From Energy to Health,” *Adv. Opt. Mater.*, vol. 3, no. 5, pp. 602–617, 2015, doi: 10.1002/adom.201500053.
- [21] J. J. Giner-Casares and L. M. Liz-Marzán, “Plasmonic nanoparticles in 2D for biological applications: Toward active multipurpose platforms,” *Nano Today*, vol. 9, no. 3, pp. 365–377, Jun. 2014, doi: 10.1016/j.nantod.2014.05.004.
- [22] “Optical properties and biomedical applications of plasmonic nanoparticles,” *J. Quant. Spectrosc. Radiat. Transf.*, vol. 111, no. 1, pp. 1–35, Jan. 2010, doi: 10.1016/j.jqsrt.2009.07.012.
- [23] F. J. Garcia-Vidal, L. Martin-Moreno, T. W. Ebbesen, and L. Kuipers, “Light passing through subwavelength apertures,” *Rev. Mod. Phys.*, vol. 82, no. 1, pp. 729–787, Mar. 2010, doi: 10.1103/RevModPhys.82.729.
- [24] R. F. Oulton *et al.*, “Plasmon lasers at deep subwavelength scale,” *Nature*, vol. 461, no. 7264, Art. no. 7264, Oct. 2009, doi: 10.1038/nature08364.
- [25] L. Novotny and N. van Hulst, “Antennas for light,” *Nat. Photonics*, vol. 5, no. 2, Art. no. 2, Feb. 2011, doi: 10.1038/nphoton.2010.237.
- [26] K. Kumar, H. Duan, R. S. Hegde, S. C. W. Koh, J. N. Wei, and J. K. W. Yang, “Printing colour at the optical diffraction limit,” *Nat. Nanotechnol.*, vol. 7, no. 9, Art. no. 9, Sep. 2012, doi: 10.1038/nnano.2012.128.
- [27] A. Woessner *et al.*, “Highly confined low-loss plasmons in graphene–boron nitride heterostructures,” *Nat. Mater.*, vol. 14, no. 4, pp. 421–425, 2015.
- [28] N. Yu *et al.*, “Light Propagation with Phase Discontinuities: Generalized Laws of Reflection and Refraction,” *Science*, vol. 334, no. 6054, pp. 333–337, Oct. 2011, doi: 10.1126/science.1210713.
- [29] J. B. Pendry, D. Schurig, and D. R. Smith, “Controlling Electromagnetic Fields,” *Science*, vol. 312, no. 5781, pp. 1780–1782, Jun. 2006, doi: 10.1126/science.1125907.
- [30] R. A. Shelby, D. R. Smith, and S. Schultz, “Experimental Verification of a Negative Index of Refraction,” *Science*, vol. 292, no. 5514, pp. 77–79, Apr. 2001, doi: 10.1126/science.1058847.

- [31] A. I. Fernández-Domínguez, F. J. García-Vidal, and L. Martín-Moreno, “Unrelenting plasmons,” *Nat. Photonics*, vol. 11, no. 1, pp. 8–10, Jan. 2017, doi: 10.1038/nphoton.2016.258.
- [32] T. Wakamatsu and K. Saito, “Interpretation of attenuated-total-reflection dips observed in surface plasmon resonance,” *JOSA B*, vol. 24, no. 9, pp. 2307–2313, 2007.
- [33] D. Barchiesi and A. Otto, “Excitations of surface plasmon polaritons by attenuated total reflection, revisited,” *Riv. Nuovo Cimento*, vol. 36, pp. 173–209, 2013.
- [34] S. Spindel and K. E. Sapsford, “Evaluation of optical detection platforms for multiplexed detection of proteins and the need for point-of-care biosensors for clinical use,” *Sensors*, vol. 14, no. 12, pp. 22313–22341, 2014.
- [35] A. Amirjani and D. F. Haghshenas, “Ag nanostructures as the surface plasmon resonance (SPR)-based sensors: A mechanistic study with an emphasis on heavy metallic ions detection,” *Sens. Actuators B Chem.*, vol. 273, pp. 1768–1779, Nov. 2018, doi: 10.1016/j.snb.2018.07.089.
- [36] Y. Jin, “Engineering Plasmonic Gold Nanostructures and Metamaterials for Biosensing and Nanomedicine,” *Adv. Mater.*, vol. 24, no. 38, pp. 5153–5165, Oct. 2012, doi: 10.1002/adma.201200622.
- [37] A. J. Gormley, N. Larson, S. Sadekar, R. Robinson, A. Ray, and H. Ghandehari, “Guided delivery of polymer therapeutics using plasmonic photothermal therapy,” *Nano Today*, vol. 7, no. 3, pp. 158–167, 2012.
- [38] M. Sharifi *et al.*, “Plasmonic gold nanoparticles: Optical manipulation, imaging, drug delivery and therapy,” *J. Controlled Release*, vol. 311, pp. 170–189, 2019.
- [39] X. Huang and M. A. El-Sayed, “Plasmonic photo-thermal therapy (PPTT),” *Alex. J. Med.*, vol. 47, no. 1, pp. 1–9, Mar. 2011, doi: 10.1016/j.ajme.2011.01.001.
- [40] X. Huang, P. K. Jain, I. H. El-Sayed, and M. A. El-Sayed, “Plasmonic photothermal therapy (PPTT) using gold nanoparticles,” *Lasers Med. Sci.*, vol. 23, no. 3, pp. 217–228, Jul. 2008, doi: 10.1007/s10103-007-0470-x.
- [41] S. A. Kim *et al.*, “Optical measurement of neural activity using surface plasmon resonance,” *Opt. Lett.*, vol. 33, no. 9, pp. 914–916, 2008.
- [42] J. W. Lee, H. Jung, H. H. Cho, J. H. Lee, and Y. Nam, “Gold nanostar-mediated neural activity control using plasmonic photothermal effects,” *Biomaterials*, vol. 153, pp. 59–69, 2018.
- [43] E. Betzig *et al.*, “Imaging Intracellular Fluorescent Proteins at Nanometer Resolution,” *Science*, vol. 313, no. 5793, pp. 1642–1645, Sep. 2006, doi: 10.1126/science.1127344.
- [44] S. Kawata, Y. Inouye, and P. Verma, “Plasmonics for near-field nano-imaging and superlensing,” *Nat. Photonics*, vol. 3, no. 7, Art. no. 7, Jul. 2009, doi: 10.1038/nphoton.2009.111.
- [45] J. Choi, S. Lee, and K. Kim, “Plasmon based super resolution imaging for single molecular detection: Breaking the diffraction limit,” *Biomed. Eng. Lett.*, vol. 4, pp. 231–238, 2014.

- [46] F. Wei and Z. Liu, “Plasmonic Structured Illumination Microscopy,” *Nano Lett.*, vol. 10, no. 7, pp. 2531–2536, Jul. 2010, doi: 10.1021/nl1011068.
- [47] F. Wei *et al.*, “Wide Field Super-Resolution Surface Imaging through Plasmonic Structured Illumination Microscopy,” *Nano Lett.*, vol. 14, no. 8, pp. 4634–4639, Aug. 2014, doi: 10.1021/nl501695c.
- [48] S. W. Hell and J. Wichmann, “Breaking the diffraction resolution limit by stimulated emission: stimulated-emission-depletion fluorescence microscopy,” *Opt. Lett.*, vol. 19, no. 11, pp. 780–782, 1994.
- [49] T. A. Klar, E. Engel, and S. W. Hell, “Breaking Abbe’s diffraction resolution limit in fluorescence microscopy with stimulated emission depletion beams of various shapes,” *Phys. Rev. E*, vol. 64, no. 6, p. 066613, Nov. 2001, doi: 10.1103/PhysRevE.64.066613.
- [50] K. A. Willets, A. J. Wilson, V. Sundaresan, and P. B. Joshi, “Super-Resolution Imaging and Plasmonics,” *Chem. Rev.*, vol. 117, no. 11, pp. 7538–7582, Jun. 2017, doi: 10.1021/acs.chemrev.6b00547.
- [51] Y. Fu and X. Zhou, “Plasmonic Lenses: A Review,” *Plasmonics*, vol. 5, no. 3, pp. 287–310, Sep. 2010, doi: 10.1007/s11468-010-9144-9.
- [52] Z. Shen and D. Huang, “A Review on Metasurface Beam Splitters,” *Nanomanufacturing*, vol. 2, no. 4, pp. 194–228, 2022.
- [53] K. Y. Kim, *Plasmonics: Principles and Applications*. BoD – Books on Demand, 2012.
- [54] M. S. Tame, K. R. McEnery, Ş. K. Özdemir, J. Lee, S. A. Maier, and M. S. Kim, “Quantum plasmonics,” *Nat. Phys.*, vol. 9, no. 6, Art. no. 6, Jun. 2013, doi: 10.1038/nphys2615.
- [55] W. Fan, B. J. Lawrie, and R. C. Pooser, “Quantum plasmonic sensing,” *Phys. Rev. A*, vol. 92, no. 5, p. 053812, Nov. 2015, doi: 10.1103/PhysRevA.92.053812.
- [56] C. Lee, B. Lawrie, R. Pooser, K.-G. Lee, C. Rockstuhl, and M. Tame, “Quantum Plasmonic Sensors,” *Chem. Rev.*, vol. 121, no. 8, pp. 4743–4804, Apr. 2021, doi: 10.1021/acs.chemrev.0c01028.
- [57] I. Bulu, T. Babinec, B. Hausmann, J. T. Choy, and M. Loncar, “Plasmonic resonators for enhanced diamond NV-center single photon sources,” *Opt. Express*, vol. 19, no. 6, pp. 5268–5276, 2011.
- [58] H. Siampour, S. Kumar, and S. I. Bozhevolnyi, “Nanofabrication of Plasmonic Circuits Containing Single Photon Sources,” *ACS Photonics*, vol. 4, no. 8, pp. 1879–1884, Aug. 2017, doi: 10.1021/acsphotonics.7b00374.
- [59] S. I. Bozhevolnyi and N. A. Mortensen, “Plasmonics for emerging quantum technologies,” *Nanophotonics*, vol. 6, no. 5, pp. 1185–1188, Aug. 2017, doi: 10.1515/nanoph-2016-0179.
- [60] G. E. Moore, “Cramming more components onto integrated circuits, Reprinted from *Electronics*, volume 38, number 8, April 19, 1965, pp. 114 ff.,” *IEEE Solid-State Circuits Soc. Newsl.*, vol. 11, no. 3, pp. 33–35, 2006.
- [61] C. Mead, “Life Without Bits,” in *Talking Back to the Machine: Computers and Human Aspiration*, P. J. Denning, Ed., New York, NY: Springer, 1999, pp. 15–21. doi: 10.1007/978-1-4612-2148-7_2.

- [62] R. R. Schaller, "Moore's law: past, present and future," *IEEE Spectr.*, vol. 34, no. 6, pp. 52–59, 1997.
- [63] M. Lundstrom, "Moore's Law Forever?," *Science*, vol. 299, no. 5604, pp. 210–211, Jan. 2003, doi: 10.1126/science.1079567.
- [64] E. Mollick, "Establishing Moore's Law," *IEEE Ann. Hist. Comput.*, vol. 28, no. 3, pp. 62–75, Jul. 2006, doi: 10.1109/MAHC.2006.45.
- [65] R. W. Keyes, "The Impact of Moore's Law," *IEEE Solid-State Circuits Soc. Newsl.*, vol. 11, no. 3, pp. 25–27, Sep. 2006, doi: 10.1109/N-SSC.2006.4785857.
- [66] C. A. Mack, "Fifty Years of Moore's Law," *IEEE Trans. Semicond. Manuf.*, vol. 24, no. 2, pp. 202–207, May 2011, doi: 10.1109/TSM.2010.2096437.
- [67] E. P. DeBenedictis, "It's Time to Redefine Moore's Law Again," *Computer*, vol. 50, no. 2, pp. 72–75, Feb. 2017, doi: 10.1109/MC.2017.34.
- [68] A. Pimpin and W. Srituravanich, "Review on micro-and nanolithography techniques and their applications," *Eng. J.*, vol. 16, no. 1, pp. 37–56, 2012.
- [69] B. Wiley *et al.*, "Shape-controlled synthesis of silver and gold nanostructures," *Mrs Bull.*, vol. 30, no. 5, pp. 356–361, 2005.
- [70] C. J. Murphy *et al.*, "Anisotropic Metal Nanoparticles: Synthesis, Assembly, and Optical Applications," *J. Phys. Chem. B*, vol. 109, no. 29, pp. 13857–13870, Jul. 2005, doi: 10.1021/jp0516846.
- [71] J. E. Millstone, S. Park, K. L. Shuford, L. Qin, G. C. Schatz, and C. A. Mirkin, "Observation of a Quadrupole Plasmon Mode for a Colloidal Solution of Gold Nanoprisms," *J. Am. Chem. Soc.*, vol. 127, no. 15, pp. 5312–5313, Apr. 2005, doi: 10.1021/ja043245a.
- [72] J. Henzie, J. Lee, M. H. Lee, W. Hasan, and T. W. Odom, "Nanofabrication of Plasmonic Structures," *Annu. Rev. Phys. Chem.*, vol. 60, no. 1, pp. 147–165, 2009, doi: 10.1146/annurev.physchem.040808.090352.
- [73] A. K. Bates *et al.*, "Review of technology for 157-nm lithography," *IBM J. Res. Dev.*, vol. 45, no. 5, pp. 605–614, 2001.
- [74] E. C. Spivey, E. T. Ritschdorff, J. L. Connell, C. A. McLennon, C. E. Schmidt, and J. B. Shear, "Multiphoton Lithography of Unconstrained Three-Dimensional Protein Microstructures," *Adv. Funct. Mater.*, vol. 23, no. 3, pp. 333–339, Jan. 2013, doi: 10.1002/adfm.201201465.
- [75] E. M. Hicks *et al.*, "Controlling Plasmon Line Shapes through Diffractive Coupling in Linear Arrays of Cylindrical Nanoparticles Fabricated by Electron Beam Lithography," *Nano Lett.*, vol. 5, no. 6, pp. 1065–1070, Jun. 2005, doi: 10.1021/nl0505492.
- [76] C. L. Haynes *et al.*, "Nanoparticle Optics: The Importance of Radiative Dipole Coupling in Two-Dimensional Nanoparticle Arrays," *J. Phys. Chem. B*, vol. 107, no. 30, pp. 7337–7342, Jul. 2003, doi: 10.1021/jp034234r.
- [77] A. A. Tseng, A. Notargiacomo, and T. P. Chen, "Nanofabrication by scanning probe microscope lithography: A review," *J. Vac. Sci. Technol. B Microelectron. Nanometer Struct. Process. Meas. Phenom.*, vol. 23, no. 3, pp. 877–894, 2005.

- [78] D. E. Grupp, H. J. Lezec, T. Thio, and T. W. Ebbesen, “Beyond the Bethe Limit: Tunable Enhanced Light Transmission Through a Single Sub-Wavelength Aperture,” *Adv. Mater.*, vol. 11, no. 10, pp. 860–862, Jul. 1999, doi: 10.1002/(SICI)1521-4095(199907)11:10<860::AID-ADMA860>3.0.CO;2-V.
- [79] U. Stamm, “Extreme ultraviolet light sources for use in semiconductor lithography—state of the art and future development,” *J. Phys. Appl. Phys.*, vol. 37, no. 23, p. 3244, 2004.
- [80] B. Wu and A. Kumar, “Extreme ultraviolet lithography: A review,” *J. Vac. Sci. Technol. B Microelectron. Nanometer Struct. Process. Meas. Phenom.*, vol. 25, no. 6, pp. 1743–1761, 2007.
- [81] E. Spille and R. Feder, “X-ray lithography,” in *X-Ray Optics: Applications to Solids*, H.-J. Queisser, Ed., in Topics in Applied Physics. , Berlin, Heidelberg: Springer, 1977, pp. 35–92. doi: 10.1007/3-540-08462-2_9.
- [82] A. Bharti, A. Turchet, and B. Marmiroli, “X-ray lithography for nanofabrication: is there a future?,” *Front. Nanotechnol.*, vol. 4, p. 835701, 2022.
- [83] S. Y. Chou, P. R. Krauss, and P. J. Renstrom, “Nanoimprint lithography,” *J. Vac. Sci. Technol. B Microelectron. Nanometer Struct. Process. Meas. Phenom.*, vol. 14, no. 6, pp. 4129–4133, 1996.
- [84] L. J. Guo, “Nanoimprint Lithography: Methods and Material Requirements,” *Adv. Mater.*, vol. 19, no. 4, pp. 495–513, Feb. 2007, doi: 10.1002/adma.200600882.
- [85] M. C. Traub, W. Longsine, and V. N. Truskett, “Advances in Nanoimprint Lithography,” *Annu. Rev. Chem. Biomol. Eng.*, vol. 7, no. 1, pp. 583–604, Jun. 2016, doi: 10.1146/annurev-chembioeng-080615-034635.
- [86] C. Lu and R. H. Lipson, “Interference lithography: a powerful tool for fabricating periodic structures,” *Laser Photonics Rev.*, vol. 4, no. 4, pp. 568–580, Jun. 2010, doi: 10.1002/lpor.200810061.
- [87] J.-H. Seo *et al.*, “Nanopatterning by Laser Interference Lithography: Applications to Optical Devices,” *J. Nanosci. Nanotechnol.*, vol. 14, no. 2, pp. 1521–1532, Feb. 2014, doi: 10.1166/jnn.2014.9199.
- [88] H. van Wolferen and L. Abelmann, “Laser interference lithography,” *Lithogr. Princ. Process. Mater.*, pp. 133–148, 2011.
- [89] Y. Wang, M. Zhang, Y. Lai, and L. Chi, “Advanced colloidal lithography: From patterning to applications,” *Nano Today*, vol. 22, pp. 36–61, Oct. 2018, doi: 10.1016/j.nantod.2018.08.010.
- [90] U. Ch. Fischer and H. P. Zingsheim, “Submicroscopic pattern replication with visible light,” *J. Vac. Sci. Technol.*, vol. 19, no. 4, pp. 881–885, Nov. 1981, doi: 10.1116/1.571227.
- [91] H. W. Deckman and J. H. Dunsmuir, “Natural lithography,” *Appl. Phys. Lett.*, vol. 41, no. 4, pp. 377–379, 1982, doi: 10.1063/1.93501.
- [92] W. Wu, D. Dey, O. G. Memis, A. Katsnelson, and H. Mohseni, “Fabrication of Large Area Periodic Nanostructures Using Nanosphere

- Photolithography,” *Nanoscale Res. Lett.*, vol. 3, no. 10, p. 351, Sep. 2008, doi: 10.1007/s11671-008-9164-y.
- [93] C. L. Haynes, A. D. McFarland, M. T. Smith, J. C. Hulteen, and R. P. Van Duyne, “Angle-Resolved Nanosphere Lithography: Manipulation of Nanoparticle Size, Shape, and Interparticle Spacing,” *J. Phys. Chem. B*, vol. 106, no. 8, pp. 1898–1902, Feb. 2002, doi: 10.1021/jp013570+.
- [94] A. Nemiroski, M. Gonidec, J. M. Fox, P. Jean-Remy, E. Turnage, and G. M. Whitesides, “Engineering Shadows to Fabricate Optical Metasurfaces,” *ACS Nano*, vol. 8, no. 11, pp. 11061–11070, Nov. 2014, doi: 10.1021/nn504214b.
- [95] H. Fredriksson *et al.*, “Hole–Mask Colloidal Lithography,” *Adv. Mater.*, vol. 19, no. 23, pp. 4297–4302, Dec. 2007, doi: 10.1002/adma.200700680.
- [96] S. Cataldo *et al.*, “Hole-Mask Colloidal Nanolithography for Large-Area Low-Cost Metamaterials and Antenna-Assisted Surface-Enhanced Infrared Absorption Substrates,” *ACS Nano*, vol. 6, no. 1, pp. 979–985, Jan. 2012, doi: 10.1021/nn2047982.
- [97] V. Peksa *et al.*, “Testing gold nanostructures fabricated by hole-mask colloidal lithography as potential substrates for SERS sensors: sensitivity, signal variability, and the aspect of adsorbate deposition,” *Phys. Chem. Chem. Phys.*, vol. 18, no. 29, pp. 19613–19620, 2016, doi: 10.1039/C6CP02752K.
- [98] R. Ogier, “Plasmonics with a Twist: from Single Particles to Metasurfaces,” 2016.
- [99] R. Ogier, L. Shao, M. Svedendahl, and M. Käll, “Continuous-Gradient Plasmonic Nanostructures Fabricated by Evaporation on a Partially Exposed Rotating Substrate,” *Adv. Mater.*, vol. 28, no. 23, pp. 4658–4664, 2016, doi: 10.1002/adma.201600112.
- [100] İ. M. Öztürk, “Fabrication of various metal nanostructures with hole mask colloidal lithography,” Master’s Thesis, Middle East Technical University, 2014. Accessed: Nov. 11, 2023. [Online]. Available: <https://open.metu.edu.tr/handle/11511/24111>
- [101] E. M. Purcell and C. R. Pennypacker, “Scattering and absorption of light by nonspherical dielectric grains,” *Astrophys. J. Vol 186 Pp 705-714 1973*, vol. 186, pp. 705–714, 1973.
- [102] B. T. Draine and P. J. Flatau, “Discrete-dipole approximation for scattering calculations,” *Josa A*, vol. 11, no. 4, pp. 1491–1499, 1994.
- [103] A. Taflove, S. C. Hagness, and M. Picket-May, “Computational Electromagnetics: the Finite-Difference Time-Domain Method, vol. 3.” Elsevier Amsterdam, The Netherlands, 2005.
- [104] U. S. Inan and R. A. Marshall, *Numerical electromagnetics: the FDTD method*. Cambridge University Press, 2011. Accessed: Nov. 26, 2023. [Online]. Available: [https://books.google.com/books?hl=tr&lr=&id=mGdH_W0YBdQC&oi=fnd&pg=PR7&dq=Inan+U.S.,+Marshall+R.A.+Numerical+Electrodynamics:+The+FDTD+Method,+Cambridge+Univ.+Press,+Cambridge+\(2011\)&ots=G2yJoHx0S_&sig=gxCX6asU57IHPP7g2-GQ7kqXHAQ](https://books.google.com/books?hl=tr&lr=&id=mGdH_W0YBdQC&oi=fnd&pg=PR7&dq=Inan+U.S.,+Marshall+R.A.+Numerical+Electrodynamics:+The+FDTD+Method,+Cambridge+Univ.+Press,+Cambridge+(2011)&ots=G2yJoHx0S_&sig=gxCX6asU57IHPP7g2-GQ7kqXHAQ)

- [105] J. S. Hesthaven, “High-order accurate methods in time-domain computational electromagnetics: A review,” in *Advances in Imaging and Electron Physics*, vol. 127, P. W. Hawkes, Ed., Elsevier, 2003, pp. 59–123. doi: 10.1016/S1076-5670(03)80097-6.
- [106] K. Busch, M. König, and J. Niegemann, “Discontinuous Galerkin methods in nanophotonics,” *Laser Photonics Rev.*, vol. 5, no. 6, pp. 773–809, Nov. 2011, doi: 10.1002/lpor.201000045.
- [107] J. A. Stratton and L. J. Chu, “Diffraction Theory of Electromagnetic Waves,” *Phys. Rev.*, vol. 56, no. 1, pp. 99–107, Jul. 1939, doi: 10.1103/PhysRev.56.99.
- [108] F. J. García De Abajo and A. Howie, “Retarded field calculation of electron energy loss in inhomogeneous dielectrics,” *Phys. Rev. B*, vol. 65, no. 11, p. 115418, Mar. 2002, doi: 10.1103/PhysRevB.65.115418.
- [109] V. Myroshnychenko, E. Carbó-Argibay, I. Pastoriza-Santos, J. Pérez-Juste, L. M. Liz-Marzán, and F. J. García de Abajo, “Modeling the Optical Response of Highly Faceted Metal Nanoparticles with a Fully 3D Boundary Element Method,” *Adv. Mater.*, vol. 20, no. 22, pp. 4288–4293, 2008, doi: 10.1002/adma.200703214.
- [110] G. A. E. Vandenbosch, V. Volski, N. Verellen, and V. V. Moshchalkov, “On the use of the method of moments in plasmonic applications,” *Radio Sci.*, vol. 46, no. 5, 2011, doi: 10.1029/2010RS004582.
- [111] E. K. Miller, “A selective survey of computational electromagnetics,” *IEEE Trans. Antennas Propag.*, vol. 36, no. 9, pp. 1281–1305, Sep. 1988, doi: 10.1109/8.8607.
- [112] F. M. Kahnert, “Numerical methods in electromagnetic scattering theory,” *J. Quant. Spectrosc. Radiat. Transf.*, vol. 79–80, pp. 775–824, Jun. 2003, doi: 10.1016/S0022-4073(02)00321-7.
- [113] P. Giri, K. Choudhary, A. S. Gupta, A. K. Bandyopadhyay, and A. R. McGurn, “Klein-Gordon equation approach to nonlinear split-ring resonator based metamaterials: One-dimensional systems,” *Phys. Rev. B*, vol. 84, no. 15, p. 155429, Oct. 2011, doi: 10.1103/PhysRevB.84.155429.
- [114] T. D. Corrigan, P. W. Kolb, A. B. Sushkov, H. D. Drew, D. C. Schmadel, and R. J. Phaneuf, “Optical plasmonic resonances in split-ring resonator structures: an improved LC model,” *Opt. Express*, vol. 16, no. 24, pp. 19850–19864, 2008.
- [115] A. Agrawal, T. Benson, R. M. De La Rue, and G. A. Wurtz, Eds., *Recent Trends in Computational Photonics*, vol. 204. in Springer Series in Optical Sciences, vol. 204. Cham: Springer International Publishing, 2017. doi: 10.1007/978-3-319-55438-9.
- [116] A. Amirjani and S. K. Sadrnezhad, “Computational electromagnetics in plasmonic nanostructures,” *J. Mater. Chem. C*, vol. 9, no. 31, pp. 9791–9819, Aug. 2021, doi: 10.1039/D1TC01742J.
- [117] J. Smajic, C. Hafner, L. Raguin, K. Tavzarashvili, and M. Mishrikey, “Comparison of Numerical Methods for the Analysis of Plasmonic

- Structures,” *J. Comput. Theor. Nanosci.*, vol. 6, no. 3, pp. 763–774, Mar. 2009, doi: 10.1166/jctn.2009.1107.
- [118] B. Gallinet, J. Butet, and O. J. F. Martin, “Numerical methods for nanophotonics: standard problems and future challenges,” *Laser Photonics Rev.*, vol. 9, no. 6, pp. 577–603, 2015, doi: 10.1002/lpor.201500122.
- [119] F. Della Sala, R. Pachter, and M. Sukharev, “Advances in modeling plasmonic systems,” *J. Chem. Phys.*, vol. 157, no. 19, p. 190401, Nov. 2022, doi: 10.1063/5.0130790.
- [120] R. Esteban, A. G. Borisov, P. Nordlander, and J. Aizpurua, “Bridging quantum and classical plasmonics with a quantum-corrected model,” *Nat. Commun.*, vol. 3, no. 1, Art. no. 1, May 2012, doi: 10.1038/ncomms1806.
- [121] Y. Yang *et al.*, “A general theoretical and experimental framework for nanoscale electromagnetism,” *Nature*, vol. 576, no. 7786, Art. no. 7786, Dec. 2019, doi: 10.1038/s41586-019-1803-1.
- [122] N. A. Mortensen, “Mesoscopic electrodynamics at metal surfaces: — From quantum-corrected hydrodynamics to microscopic surface-response formalism,” *Nanophotonics*, vol. 10, no. 10, pp. 2563–2616, Aug. 2021, doi: 10.1515/nanoph-2021-0156.
- [123] H. M. Baghramyan, F. Della Sala, and C. Ciraci, “Laplacian-Level Quantum Hydrodynamic Theory for Plasmonics,” *Phys. Rev. X*, vol. 11, no. 1, p. 011049, Mar. 2021, doi: 10.1103/PhysRevX.11.011049.
- [124] W. Yan, M. Wubs, and N. Asger Mortensen, “Projected Dipole Model for Quantum Plasmonics,” *Phys. Rev. Lett.*, vol. 115, no. 13, p. 137403, Sep. 2015, doi: 10.1103/PhysRevLett.115.137403.
- [125] C. Ciraci and F. Della Sala, “Quantum hydrodynamic theory for plasmonics: Impact of the electron density tail,” *Phys. Rev. B*, vol. 93, no. 20, p. 205405, May 2016, doi: 10.1103/PhysRevB.93.205405.
- [126] G. Toscano *et al.*, “Resonance shifts and spill-out effects in self-consistent hydrodynamic nanoplasmonics,” *Nat. Commun.*, vol. 6, no. 1, Art. no. 1, May 2015, doi: 10.1038/ncomms8132.
- [127] L. L. Jensen and L. Jensen, “Atomistic Electrodynamics Model for Optical Properties of Silver Nanoclusters,” *J. Phys. Chem. C*, vol. 113, no. 34, pp. 15182–15190, Aug. 2009, doi: 10.1021/jp904956f.
- [128] X. Chen, J. E. Moore, M. Zekarias, and L. Jensen, “Atomistic electrodynamics simulations of bare and ligand-coated nanoparticles in the quantum size regime,” *Nat. Commun.*, vol. 6, no. 1, Art. no. 1, Nov. 2015, doi: 10.1038/ncomms9921.
- [129] T. Giovannini, M. Rosa, S. Corni, and C. Cappelli, “A classical picture of subnanometer junctions: an atomistic Drude approach to nanoplasmonics,” *Nanoscale*, vol. 11, no. 13, pp. 6004–6015, 2019, doi: 10.1039/C8NR09134J.
- [130] L. Bonatti, G. Gil, T. Giovannini, S. Corni, and C. Cappelli, “Plasmonic resonances of metal nanoparticles: Atomistic vs. continuum approaches,” *Front. Chem.*, vol. 8, p. 340, 2020.

- [131] M. Barbry *et al.*, “Atomistic Near-Field Nanoplasmonics: Reaching Atomic-Scale Resolution in Nanooptics,” *Nano Lett.*, vol. 15, no. 5, pp. 3410–3419, May 2015, doi: 10.1021/acs.nanolett.5b00759.
- [132] R. Sinha-Roy, P. García-González, H.-C. Weissker, F. Rabilloud, and A. I. Fernández-Domínguez, “Classical and *ab Initio* Plasmonics Meet at Subnanometric Noble Metal Rods,” *ACS Photonics*, vol. 4, no. 6, pp. 1484–1493, Jun. 2017, doi: 10.1021/acsphotonics.7b00254.
- [133] T. P. Rossi, T. Shegai, P. Erhart, and T. J. Antosiewicz, “Strong plasmon-molecule coupling at the nanoscale revealed by first-principles modeling,” *Nat. Commun.*, vol. 10, no. 1, Art. no. 1, Jul. 2019, doi: 10.1038/s41467-019-11315-5.
- [134] T. Neuman, R. Esteban, D. Casanova, F. J. García-Vidal, and J. Aizpurua, “Coupling of Molecular Emitters and Plasmonic Cavities beyond the Point-Dipole Approximation,” *Nano Lett.*, vol. 18, no. 4, pp. 2358–2364, Apr. 2018, doi: 10.1021/acs.nanolett.7b05297.
- [135] T. V. Shahbazyan, “Exciton–Plasmon Energy Exchange Drives the Transition to a Strong Coupling Regime,” *Nano Lett.*, vol. 19, no. 5, pp. 3273–3279, May 2019, doi: 10.1021/acs.nanolett.9b00827.
- [136] M. Pelton, S. D. Storm, and H. Leng, “Strong coupling of emitters to single plasmonic nanoparticles: exciton-induced transparency and Rabi splitting,” *Nanoscale*, vol. 11, no. 31, pp. 14540–14552, 2019.
- [137] C. Ciracì, R. Jurga, M. Khalid, and F. Della Sala, “Plasmonic quantum effects on single-emitter strong coupling,” *Nanophotonics*, vol. 8, no. 10, pp. 1821–1833, Sep. 2019, doi: 10.1515/nanoph-2019-0199.
- [138] J. Flick, M. Ruggenthaler, H. Appel, and A. Rubio, “Atoms and molecules in cavities, from weak to strong coupling in quantum-electrodynamics (QED) chemistry,” *Proc. Natl. Acad. Sci.*, vol. 114, no. 12, pp. 3026–3034, Mar. 2017, doi: 10.1073/pnas.1615509114.
- [139] C. Schäfer, M. Ruggenthaler, and A. Rubio, “*Ab initio* nonrelativistic quantum electrodynamics: Bridging quantum chemistry and quantum optics from weak to strong coupling,” *Phys. Rev. A*, vol. 98, no. 4, p. 043801, Oct. 2018, doi: 10.1103/PhysRevA.98.043801.
- [140] I. Medina, F. J. García-Vidal, A. I. Fernández-Domínguez, and J. Feist, “Few-Mode Field Quantization of Arbitrary Electromagnetic Spectral Densities,” *Phys. Rev. Lett.*, vol. 126, no. 9, p. 093601, Mar. 2021, doi: 10.1103/PhysRevLett.126.093601.
- [141] J. Feist, A. I. Fernández-Domínguez, and F. J. García-Vidal, “Macroscopic QED for quantum nanophotonics: emitter-centered modes as a minimal basis for multiemitter problems,” *Nanophotonics*, vol. 10, no. 1, pp. 477–489, Oct. 2020, doi: 10.1515/nanoph-2020-0451.
- [142] W. Yan, M. Wubs, and N. Asger Mortensen, “Projected Dipole Model for Quantum Plasmonics,” *Phys. Rev. Lett.*, vol. 115, no. 13, p. 137403, Sep. 2015, doi: 10.1103/PhysRevLett.115.137403.

- [143] U. Hohenester and A. Trügler, “MNPBEM—A Matlab toolbox for the simulation of plasmonic nanoparticles,” *Comput. Phys. Commun.*, vol. 183, no. 2, pp. 370–381, 2012.
- [144] J. Waxenegger, A. Trügler, and U. Hohenester, “Plasmonics simulations with the MNPBEM toolbox: Consideration of substrates and layer structures,” *Comput. Phys. Commun.*, vol. 193, pp. 138–150, 2015.
- [145] U. Hohenester, “Making simulations with the MNPBEM toolbox big: Hierarchical matrices and iterative solvers,” *Comput. Phys. Commun.*, vol. 222, pp. 209–228, Jan. 2018, doi: 10.1016/j.cpc.2017.08.010.
- [146] R. L. McCreery, *Raman Spectroscopy for Chemical Analysis*. John Wiley & Sons, 2005.
- [147] D.J. Gardiner, P.R. Graves, and HJ Bowley, “Practical Raman Spectroscopy,” *Springer-Verl.*, vol. 55–76, 1989.
- [148] R. R. Jones, D. C. Hooper, L. Zhang, D. Wolverson, and V. K. Valev, “Raman Techniques: Fundamentals and Frontiers,” *Nanoscale Res. Lett.*, vol. 14, p. 231, Jul. 2019, doi: 10.1186/s11671-019-3039-2.
- [149] R. Pilot, R. Signorini, C. Durante, L. Orian, M. Bhamidipati, and L. Fabris, “A Review on Surface-Enhanced Raman Scattering,” *Biosensors*, vol. 9, no. 2, Jun. 2019, doi: 10.3390/bios9020057.
- [150] R. S. Krishnan and R. K. Shankar, “Raman effect: History of the discovery,” *J. Raman Spectrosc.*, vol. 10, no. 1, pp. 1–8, 1981, doi: 10.1002/jrs.1250100103.
- [151] M. Fleischmann, P. J. Hendra, and A. J. McQuillan, “Raman spectra of pyridine adsorbed at a silver electrode,” *Chem. Phys. Lett.*, vol. 26, no. 2, pp. 163–166, May 1974, doi: 10.1016/0009-2614(74)85388-1.
- [152] M. G. Albrecht and J. A. Creighton, “Anomalously intense Raman spectra of pyridine at a silver electrode,” *J. Am. Chem. Soc.*, vol. 99, no. 15, pp. 5215–5217, Jun. 1977, doi: 10.1021/ja00457a071.
- [153] D. L. Jeanmaire and R. P. Van Duyne, “Surface raman spectroelectrochemistry: Part I. Heterocyclic, aromatic, and aliphatic amines adsorbed on the anodized silver electrode,” *J. Electroanal. Chem. Interfacial Electrochem.*, vol. 84, no. 1, pp. 1–20, Nov. 1977, doi: 10.1016/S0022-0728(77)80224-6.
- [154] A. Campion and P. Kambhampati, “Surface-enhanced Raman scattering,” *Chem. Soc. Rev.*, vol. 27, no. 4, pp. 241–250, Jan. 1998, doi: 10.1039/A827241Z.
- [155] G. C. Schatz, M. A. Young, and R. P. Van Duyne, “Electromagnetic Mechanism of SERS,” in *Surface-Enhanced Raman Scattering: Physics and Applications*, K. Kneipp, M. Moskovits, and H. Kneipp, Eds., in Topics in Applied Physics. , Berlin, Heidelberg: Springer, 2006, pp. 19–45. doi: 10.1007/3-540-33567-6_2.
- [156] M. Fan, G. F. S. Andrade, and A. G. Brolo, “A review on the fabrication of substrates for surface enhanced Raman spectroscopy and their applications in analytical chemistry,” *Anal. Chim. Acta*, vol. 693, no. 1, pp. 7–25, May 2011, doi: 10.1016/j.aca.2011.03.002.

- [157] S.-C. Luo, K. Sivashanmugan, J.-D. Liao, C.-K. Yao, and H.-C. Peng, “Nanofabricated SERS-active substrates for single-molecule to virus detection in vitro: A review,” *Biosens. Bioelectron.*, vol. 61, pp. 232–240, Nov. 2014, doi: 10.1016/j.bios.2014.05.013.
- [158] R. G. Freeman *et al.*, “Self-Assembled Metal Colloid Monolayers: An Approach to SERS Substrates,” *Science*, vol. 267, no. 5204, pp. 1629–1632, Mar. 1995, doi: 10.1126/science.267.5204.1629.
- [159] A. Kaminska, O. Inya-Agha, R. J. Forster, and T. E. Keyes, “Chemically bound gold nanoparticle arrays on silicon: assembly, properties and SERS study of protein interactions,” *Phys. Chem. Chem. Phys.*, vol. 10, no. 28, pp. 4172–4180, Jul. 2008, doi: 10.1039/B803007C.
- [160] A. Cerf, G. Molnár, and C. Vieu, “Novel Approach for the Assembly of Highly Efficient SERS Substrates,” *ACS Appl. Mater. Interfaces*, vol. 1, no. 11, pp. 2544–2550, Nov. 2009, doi: 10.1021/am900476d.
- [161] C. Fang, A. Agarwal, H. Ji, W. Y. Karen, and L. Yobas, “Preparation of a SERS substrate and its sample-loading method for point-of-use application,” *Nanotechnology*, vol. 20, no. 40, p. 405604, Sep. 2009, doi: 10.1088/0957-4484/20/40/405604.
- [162] F. Toderas, M. Baia, L. Baia, and S. Astilean, “Controlling gold nanoparticle assemblies for efficient surface-enhanced Raman scattering and localized surface plasmon resonance sensors,” *Nanotechnology*, vol. 18, no. 25, p. 255702, May 2007, doi: 10.1088/0957-4484/18/25/255702.
- [163] M. Xue, Z. Zhang, N. Zhu, F. Wang, X. Zhao, and T. Cao, “Transfer Printing of Metal Nanoparticles with Controllable Dimensions, Placement, and Reproducible Surface-Enhanced Raman Scattering Effects,” *Langmuir*, vol. 25, no. 8, pp. 4347–4351, Apr. 2009, doi: 10.1021/la900462f.
- [164] E. C. Le Ru, E. Blackie, M. Meyer, and P. G. Etchegoin, “Surface Enhanced Raman Scattering Enhancement Factors: A Comprehensive Study,” *J. Phys. Chem. C*, vol. 111, no. 37, pp. 13794–13803, Sep. 2007, doi: 10.1021/jp0687908.
- [165] S. E. J. Bell *et al.*, “Towards Reliable and Quantitative Surface-Enhanced Raman Scattering (SERS): From Key Parameters to Good Analytical Practice,” *Angew. Chem. Int. Ed.*, vol. 59, no. 14, pp. 5454–5462, 2020, doi: 10.1002/anie.201908154.
- [166] A. Hakonen, P. O. Andersson, M. Stenbæk Schmidt, T. Rindzevicius, and M. Käll, “Explosive and chemical threat detection by surface-enhanced Raman scattering: A review,” *Anal. Chim. Acta*, vol. 893, pp. 1–13, Sep. 2015, doi: 10.1016/j.aca.2015.04.010.
- [167] D. Lin *et al.*, “A novel SERS selective detection sensor for trace trinitrotoluene based on meisenheimer complex of monoethanolamine molecule,” *Talanta*, vol. 218, p. 121157, Oct. 2020, doi: 10.1016/j.talanta.2020.121157.
- [168] Z. Gong, H. Du, F. Cheng, C. Wang, C. Wang, and M. Fan, “Fabrication of SERS Swab for Direct Detection of Trace Explosives in Fingerprints,” *ACS*

- Appl. Mater. Interfaces*, vol. 6, no. 24, pp. 21931–21937, Dec. 2014, doi: 10.1021/am507424v.
- [169] L. M. Malard, M. A. Pimenta, G. Dresselhaus, and M. S. Dresselhaus, “Raman spectroscopy in graphene,” *Phys. Rep.*, vol. 473, no. 5, pp. 51–87, Apr. 2009, doi: 10.1016/j.physrep.2009.02.003.
- [170] P. Venezuela, M. Lazzeri, and F. Mauri, “Theory of double-resonant Raman spectra in graphene: Intensity and line shape of defect-induced and two-phonon bands,” *Phys. Rev. B*, vol. 84, no. 3, p. 035433, Jul. 2011, doi: 10.1103/PhysRevB.84.035433.
- [171] C. Lee, H. Yan, L. E. Brus, T. F. Heinz, J. Hone, and S. Ryu, “Anomalous Lattice Vibrations of Single- and Few-Layer MoS₂,” *ACS Nano*, vol. 4, no. 5, pp. 2695–2700, May 2010, doi: 10.1021/nn1003937.
- [172] R. Yan *et al.*, “Thermal Conductivity of Monolayer Molybdenum Disulfide Obtained from Temperature-Dependent Raman Spectroscopy,” *ACS Nano*, vol. 8, no. 1, pp. 986–993, Jan. 2014, doi: 10.1021/nn405826k.
- [173] R. Loudon and N. Kurti, “Theory of the first-order Raman effect in crystals,” *Proc. R. Soc. Lond. Ser. Math. Phys. Sci.*, vol. 275, no. 1361, pp. 218–232, Jan. 1997, doi: 10.1098/rspa.1963.0166.
- [174] A. C. Ferrari *et al.*, “Raman Spectrum of Graphene and Graphene Layers,” *Phys. Rev. Lett.*, vol. 97, no. 18, p. 187401, Oct. 2006, doi: 10.1103/PhysRevLett.97.187401.
- [175] D. A. Chenet *et al.*, “In-Plane Anisotropy in Mono- and Few-Layer ReS₂ Probed by Raman Spectroscopy and Scanning Transmission Electron Microscopy,” *Nano Lett.*, vol. 15, no. 9, pp. 5667–5672, Sep. 2015, doi: 10.1021/acs.nanolett.5b00910.
- [176] S. Palleschi, D. Matrippolito, P. Benassi, M. Nardone, and L. Ottaviano, “Micro-Raman investigation of p-type B doped Si(1 0 0) revisited,” *Appl. Surf. Sci.*, vol. 561, p. 149691, Sep. 2021, doi: 10.1016/j.apsusc.2021.149691.
- [177] J. C. Burton *et al.*, “Spatial characterization of doped SiC wafers by Raman spectroscopy,” *J. Appl. Phys.*, vol. 84, no. 11, pp. 6268–6273, Dec. 1998, doi: 10.1063/1.368947.
- [178] S. J. Kim *et al.*, “Characterization of chemical doping of graphene by in-situ Raman spectroscopy,” *Appl. Phys. Lett.*, vol. 108, no. 20, p. 203111, May 2016, doi: 10.1063/1.4950969.
- [179] M. Kitajima, “Defects in crystals studied by Raman scattering,” *Crit. Rev. Solid State Mater. Sci.*, vol. 22, no. 4, pp. 275–349, Dec. 1997, doi: 10.1080/10408439708241263.
- [180] A. Nakajima, A. Yoshihara, and M. Ishigame, “Defect-induced Raman spectra in doped $\{\mathrm{CeO}\}_2$,” *Phys. Rev. B*, vol. 50, no. 18, pp. 13297–13307, Nov. 1994, doi: 10.1103/PhysRevB.50.13297.
- [181] H. Malekpour and A. A. Balandin, “Raman-based technique for measuring thermal conductivity of graphene and related materials,” *J. Raman Spectrosc.*, vol. 49, no. 1, pp. 106–120, 2018, doi: 10.1002/jrs.5230.

- [182] T. Beechem, L. Yates, and S. Graham, “Invited Review Article: Error and uncertainty in Raman thermal conductivity measurements,” *Rev. Sci. Instrum.*, vol. 86, no. 4, p. 041101, Apr. 2015, doi: 10.1063/1.4918623.
- [183] R. J. Angel, M. Murri, B. Mihailova, and M. Alvaro, “Stress, strain and Raman shifts,” *Z. Für Krist. - Cryst. Mater.*, vol. 234, no. 2, pp. 129–140, Feb. 2019, doi: 10.1515/zkri-2018-2112.
- [184] P. Colomban, “Analysis of Strain and Stress in Ceramic, Polymer and Metal Matrix Composites by Raman Spectroscopy,” *Adv. Eng. Mater.*, vol. 4, no. 8, pp. 535–542, 2002, doi: 10.1002/1527-2648(20020806)4:8<535::AID-ADEM535>3.0.CO;2-E.
- [185] L. Ma, W. Qiu, and X. Fan, “Stress/strain characterization in electronic packaging by micro-Raman spectroscopy: A review,” *Microelectron. Reliab.*, vol. 118, p. 114045, Mar. 2021, doi: 10.1016/j.microrel.2021.114045.
- [186] K. W. Adu, Q. Xiong, H. R. Gutierrez, G. Chen, and P. C. Eklund, “Raman scattering as a probe of phonon confinement and surface optical modes in semiconducting nanowires,” *Appl. Phys. A*, vol. 85, no. 3, pp. 287–297, Nov. 2006, doi: 10.1007/s00339-006-3716-8.
- [187] R. R. Prabhu and M. Abdul Khadar, “Study of optical phonon modes of CdS nanoparticles using Raman spectroscopy,” *Bull. Mater. Sci.*, vol. 31, no. 3, pp. 511–515, Jun. 2008, doi: 10.1007/s12034-008-0080-7.
- [188] C. Kranert, R. Schmidt-Grund, and M. Grundmann, “Raman active phonon modes of cubic In₂O₃,” *Phys. Status Solidi RRL – Rapid Res. Lett.*, vol. 8, no. 6, pp. 554–559, 2014, doi: 10.1002/pssr.201409004.
- [189] J. Krajczewski, K. Kołataj, and A. Kudelski, “Plasmonic nanoparticles in chemical analysis,” *RSC Adv.*, vol. 7, no. 28, pp. 17559–17576, 2017, doi: 10.1039/C7RA01034F.
- [190] W. Ahmed, İ. M. Öztürk, R. M. F. Iftikhar, and A. Bek, “Seedless, size and shape controlled synthesis of gold mesoscopic particles and their excellent SERS applications,” *Mater. Chem. Phys.*, vol. 278, 2022, doi: 10.1016/j.matchemphys.2021.125589.
- [191] W. Ahmed, Ö. Demirtaş, İ. M. Öztürk, and A. Bek, “Monolayer Assembly of MultiSpiked Gold Nanoparticles for Surface-Enhanced Raman Spectroscopy-Based Trace Detection of Dyes and Explosives,” *ACS Appl. Nano Mater.*, vol. 3, no. 7, 2020, doi: 10.1021/acsanm.0c01177.
- [192] Ö. Demirtaş, D. Doğanay, İ. M. Öztürk, H. E. Ünalın, and A. Bek, “Facile preparation of nanoparticle based SERS substrates for trace molecule detection,” *Phys. Chem. Chem. Phys.*, vol. 22, no. 37, 2020, doi: 10.1039/d0cp01866j.
- [193] S. Pillai and M. A. Green, “Plasmonics for photovoltaic applications,” *Sol. Energy Mater. Sol. Cells*, vol. 94, no. 9, pp. 1481–1486, Sep. 2010, doi: 10.1016/j.solmat.2010.02.046.
- [194] H. A. Atwater and A. Polman, “Plasmonics for improved photovoltaic devices,” *Nat. Mater.*, vol. 9, no. 3, pp. 205–213, Mar. 2010, doi: 10.1038/nmat2629.

- [195] O. O. Havryliuk, A. A. Evtukh, O. V. Pylypova, O. Yu. Semchuk, I. I. Ivanov, and V. F. Zabolotnyi, “Plasmonic enhancement of light to improve the parameters of solar cells,” *Appl. Nanosci.*, vol. 10, no. 12, pp. 4759–4766, Dec. 2020, doi: 10.1007/s13204-020-01299-w.
- [196] G. Birant, I. M. Ozturk, D. Doganay, H. E. Unalan, and A. Bek, “Plasmonic Light-Management Interfaces by Polyol-Synthesized Silver Nanoparticles for Industrial Scale Silicon Solar Cells,” *ACS Appl. Nano Mater.*, vol. 3, no. 12, 2020, doi: 10.1021/acsanm.0c02694.
- [197] D. Derkacs, S. H. Lim, P. Matheu, W. Mar, and E. T. Yu, “Improved performance of amorphous silicon solar cells via scattering from surface plasmon polaritons in nearby metallic nanoparticles,” *Appl. Phys. Lett.*, vol. 89, no. 9, 2006, Accessed: Dec. 02, 2023. [Online]. Available: <https://pubs.aip.org/aip/apl/article/89/9/093103/120468>
- [198] K. Nakayama, K. Tanabe, and H. A. Atwater, “Plasmonic nanoparticle enhanced light absorption in GaAs solar cells,” *Appl. Phys. Lett.*, vol. 93, no. 12, 2008, Accessed: Dec. 02, 2023. [Online]. Available: <https://pubs.aip.org/aip/apl/article/93/12/121904/131430>
- [199] R. B. Konda *et al.*, “Surface plasmon excitation via Au nanoparticles in n-CdSe/ p-Si heterojunction diodes,” *Appl. Phys. Lett.*, vol. 91, no. 19, 2007, Accessed: Dec. 02, 2023. [Online]. Available: <https://pubs.aip.org/aip/apl/article-abstract/91/19/191111/119034>
- [200] I. M. Pryce, D. D. Koleske, A. J. Fischer, and H. A. Atwater, “Plasmonic nanoparticle enhanced photocurrent in GaN/InGaN/GaN quantum well solar cells,” *Appl. Phys. Lett.*, vol. 96, no. 15, 2010, Accessed: Dec. 02, 2023. [Online]. Available: <https://pubs.aip.org/aip/apl/article/96/15/153501/338566>
- [201] A. J. Morfa, K. L. Rowlen, T. H. Reilly, M. J. Romero, and J. van de Lagemaat, “Plasmon-enhanced solar energy conversion in organic bulk heterojunction photovoltaics,” *Appl. Phys. Lett.*, vol. 92, no. 1, 2008, Accessed: Dec. 02, 2023. [Online]. Available: <https://pubs.aip.org/aip/apl/article/92/1/013504/913669>
- [202] M. Westphalen, U. Kreibig, J. Rostalski, H. Lüth, and D. Meissner, “Metal cluster enhanced organic solar cells,” *Sol. Energy Mater. Sol. Cells*, vol. 61, no. 1, pp. 97–105, 2000.
- [203] C. Wen, K. Ishikawa, M. Kishima, and K. Yamada, “Effects of silver particles on the photovoltaic properties of dye-sensitized TiO₂ thin films,” *Sol. Energy Mater. Sol. Cells*, vol. 61, no. 4, pp. 339–351, 2000.
- [204] Y.-F. Li, Z.-L. Kou, J. Feng, and H.-B. Sun, “Plasmon-enhanced organic and perovskite solar cells with metal nanoparticles,” *Nanophotonics*, vol. 9, no. 10, pp. 3111–3133, Aug. 2020, doi: 10.1515/nanoph-2020-0099.
- [205] S. A. Maier, *Plasmonics: Fundamentals and Applications*. New York, NY: Springer US, 2007. doi: 10.1007/0-387-37825-1.
- [206] T. Giovannini *et al.*, “Do We Really Need Quantum Mechanics to Describe Plasmonic Properties of Metal Nanostructures?,” *ACS Photonics*, vol. 9, no. 9, pp. 3025–3034, Sep. 2022, doi: 10.1021/acsp Photonics.2c00761.

- [207] J. A. Stratton and H. G. Houghton, “A Theoretical Investigation of the Transmission of Light through Fog,” *Phys. Rev.*, vol. 38, no. 1, pp. 159–165, Jul. 1931, doi: 10.1103/PhysRev.38.159.
- [208] M. Born and E. Wolf, *Principles of optics: electromagnetic theory of propagation, interference and diffraction of light*. Elsevier, 2013. Accessed: Nov. 23, 2023. [Online]. Available: <https://books.google.com/books?hl=tr&lr=&id=HY-GDAAAQBAJ&oi=fnd&pg=PP1&dq=Born+and+Wolf++mie+theory&ots=4u3gzaoEKE&sig=tCmUDjgFsOroCRPTI2BTI4ugm98>
- [209] H. C. Hulst and H. C. van de Hulst, *Light scattering by small particles*. Courier Corporation, 1981. Accessed: Nov. 23, 2023. [Online]. Available: https://books.google.com/books?hl=tr&lr=&id=PIHfPMVAFRcC&oi=fnd&pg=PA1&dq=van+de+Hulst++mie+theory&ots=Gi_8RvmrI9&sig=-nPKd6kz7KFn4ppMkRM1OYn08Bo
- [210] S. V. Gaponenko, *Introduction to Nanophotonics*. Cambridge: Cambridge University Press, 2010. doi: 10.1017/CBO9780511750502.
- [211] C. F. Bohren, “How can a particle absorb more than the light incident on it?,” *Am. J. Phys.*, vol. 51, no. 4, pp. 323–327, Apr. 1983, doi: 10.1119/1.13262.
- [212] V. E. Ferry, J. N. Munday, and H. A. Atwater, “Design Considerations for Plasmonic Photovoltaics,” *Adv. Mater.*, vol. 22, no. 43, pp. 4794–4808, Nov. 2010, doi: 10.1002/adma.201000488.
- [213] K. R. Catchpole and A. Polman, “Design principles for particle plasmon enhanced solar cells,” *Appl. Phys. Lett.*, vol. 93, no. 19, 2008, Accessed: Nov. 21, 2023. [Online]. Available: <https://pubs.aip.org/aip/apl/article/93/19/191113/335818>
- [214] A. Ali, F. El-Mellouhi, A. Mitra, and B. Aïssa, “Research progress of plasmonic nanostructure-enhanced photovoltaic solar cells,” *Nanomaterials*, vol. 12, no. 5, p. 788, 2022.

APPENDICES

A. Mesh import into MNPBEM

- Model should be exported a mesh file in “.stl” format. This format is dimensionless modeling should be made with default unit of the modeling software, MNPBEM assumes the file is in “nm” as default unit.
- “stlread” function should be added to Matlab path. The function can be downloaded from:

<https://github.com/robEllenberg/MATLAB/blob/master/toolbox/stlread/stlread.m>

- The code below can be used to import the file into simulation

```
% stl to matlab
[v, f, n, c, stltitle] = stlread('structure.stl', false);

% Duplicate vertices can be removed using:
[v, f]=patchslim(v, f);

% A flipface operation should correct
p = particle( v, f );

% Face normals should point outwards in MNPBEM
p = flipfaces( p );

% for layered problems lift the particle above layer
p = shift (p1, [0, 0, - min( p.pos( :, 3 ) ) + 0.01 + ztab]);

% set up COMPARTICLE object as usual
p = comparticle( epstab, { p }, [ 2, 1 ], 1, op );

% to check surface normals pointing outwards
figure1 = figure;
plot( p, 'EdgeColor', 'b' , 'nvec', 1 );

% to check the dimensions
figure2 = figure;
axes1 = axes('Parent',figure2);
hold(axes1,'all');
xlabel('x (nm) ');
ylabel('y (nm) ');
plot(p);
```

- It is good practice to plot particle check the dimensions and check if the surface normal vectors are pointing outward from the particle
- Note that MNPBEM uses the mesh of the file directly for simulation without further refinement. Any mesh refinement should be done prior to the import.

B. DF Objective Matched Scattering Calculation in MNPBEM

- A simulation code in MNPBEM for scattering cross-section calculation for dark field condenser illumination is shared below.
- Note that the code is tested with MNPBEM17 and works on Matlab 2017b but don't work on Matlab 2019b.

```
% Dark_Field_spectra for metallic structure on substrate.
% Incident angles thetamax and thetamin are matched to
transmission mode Dark field spectroscopy system on NOLab.
% with TM & TE polarizations and/or both of them together may be
calculated
% computes the scattering spectrum using the full Maxwell
equations.

%% initialization
% table of dielectric functions
epstab = { epsconst( 1 ), epstable( 'silver.dat' ), epsconst( 2.25
) };
% location of interface of substrate
ztab = 0;
% default options for layer structure
op = layerstructure.options;
% set up layer structure
layer = layerstructure( epstab, [ 1, 3 ], ztab, op );
% options for BEM simulations
op = bemoptions( 'sim', 'ret', 'interp', 'curv', 'layer', layer
);

% initialize nanosphere
p = trisphere( 144, 100 ); %(mesh, dia)
% shift nanosphere 2 nm above layer
p = shift( p, [ 0, 0, - min( p.pos( :, 3 ) ) + 2 + ztab ] );

% set up COMPARTICLE objects
p = comparticle( epstab, { p }, [ 2, 1 ], 1, op );

%plot( p, 'EdgeColor', 'b', 'nvec', 1 );

%% light propagation angles for DF objective
% n is the refractive index of layer on top in experiment
% Set d value to 1 for illumination from glass substrate (bottom
layer), -1 for illumination from air

d = -1;
if d == 1
    n = 1.5;
elseif d == -1
    n = 1;
```

end

```
%the numerical aperture of DF objective
thetamin = asin(0.8/n)*180/pi;
thetamax = asin(0.95/n)*180/pi;

% Sweep theta range with 9 points
theta = pi / 180 * reshape( linspace( thetamin, thetamax, 9 ), [],
1 );

% Excitation direction, dir(:,3 ; :,3) (-) for front (+) for back
excitation
dir = [ sin( theta ), 0 * theta, d*cos( theta ) ; sin( theta ), 0
* theta, d*cos( theta ) ; 0 * theta, sin( theta ) , d*cos( theta )
; 0 * theta, sin( theta ) , d*cos( theta )];
pol1 = [ cos( theta ), 0 * theta, sin( theta ) ]; %TMx
pol2 = [ 0 * theta , 1+(theta*0) , 0 * theta ] ; %TEx
pol3 = [0 * theta , cos( theta ) , sin( theta ) ] ; %TMy
pol4 = [1+(theta*0) , 0 * theta , 0 * theta ] ; %TEy
pol = [ pol1 ; pol2 ; pol3 ; pol4 ];

% photon wavelengths
enei = linspace( 300, 1300, 101 );

%% tabulated Green functions
% For the retarded simulation we first have to set up a table for
the
% calculation of the reflected Green function. This part is
usually slow
% and we thus compute GREENTAB only if it has not been computed
before.

if ~exist( 'greentab', 'var' ) || ~greentab.ismember( layer, enei,
p )
% automatic grid for tabulation
% we use a rather small number NZ for tabulation to speed up
the
% simulations
tab = tabspace( layer, p, 'nz', 10 );
% Green function table
greentab = compgreentablayer( layer, tab );
% precompute Green function table
% for a more accurate simulation of the layer the number of
% wavelenghts should be increased
greentab = set( greentab, linspace( 300, 1300, 51 ), op );
end
op.greentab = greentab;

%% BEM solver
% initialize BEM solver
bem = bemsolver( p, op );
% initialize plane wave excitation
exc = planewave( pol, dir, op );
```

```

%exc2 = planewave(pol2, dir, op);
% scattering cross section
sca = zeros( numel( enei ), size( dir, 1 ) );

multiWaitbar( 'BEM solver', 0, 'Color', 'g', 'CanCancel', 'on' );
% loop over wavelengths
for ien = 1 : length( enei )
    % surface charges
    sig = bem \ exc( p, enei( ien ) );
    % scattering cross section
    sca( ien, : ) = exc.sca( sig );

    multiWaitbar( 'BEM solver', ien / numel( enei ) );
end
% close waitbar
multiWaitbar( 'CloseAll' );

%% final plot

filename = 'filename.txt';
imagename = 'imagename.png';
figname = 'figname.fig';

% averaging the angular calculations
DF = [ enei' , (sca(:,1) + sca(:,2) + sca(:,3) + sca(:,4) +
sca(:,5) + sca(:,6) + sca(:,7) + sca(:,8) + sca(:,9) + sca(:,10) +
sca(:,11) + sca(:,12) + sca(:,13) + sca(:,14) + sca(:,15) +
sca(:,16) + sca(:,17) + sca(:,18) + sca(:,19) + sca(:,20) +
sca(:,21) + sca(:,22) + sca(:,23) + sca(:,24) + sca(:,25) +
sca(:,26) + sca(:,27) + sca(:,28) + sca(:,29) + sca(:,30) +
sca(:,31) + sca(:,32) + sca(:,33) + sca(:,34) + sca(:,35) +
sca(:,36))/36)];

figure1 = figure;
axes1 = axes('Parent',figure1);
hold(axes1,'all');
plot( enei, DF(:,2) , 'o-' ); hold on; %tot
xlabel( 'Wavelength (nm)' );
ylabel( 'Total Scattering cross section (nm^2)' ); %tot
legend( 'Dark Field Spectrum' ) %tot
title( 'TE+TM polarization, excitation from glass' );

% save data
save(filename , 'DF' , '-ascii')
% here you save the figure image
saveas(figure1,imagename)
%you can save matlab .fig file
saveas(figure1,figname)

```


CURRICULUM VITAE

Surname, Name: Öztürk, İbrahim Murat

Nationality: Turkish

EDUCATION

Degree	Institution	Year of Graduation
PHD	METU Physics	2023
MS	METU Physics	2014
BS	METU Physics	2011
High School	Ankara Atatürk Anadolu Lisesi	2006

WORK EXPERIENCE

Year	Place	Enrollment
2021 -	Tübitak Sage, Optical Systems Dept.	Researcher
2011 - 2021	METU Physics Department	Research Asistant

R&D EXPERIENCE

- Thin film interference filters and optical thin film coatings
- Computational modelling of electromagnetism
- Lithography methods and procedures
- Optical spectroscopy systems
- Thin film deposition methods
- Lasers, Fiber lasers, Pulsed lasers
- Microscopy and nano-imaging methods
- 3D printing

PUBLICATIONS

W. Ahmed, R. M. F. Iftikhar, İ. M. Öztürk, A. Bek “*Seedless Size and Shape Controlled Synthesis of Hierarchical Gold Mesoscopic Particles and their Excellent SERS applications*” *Materials Chemistry and Physics*, 125589, 2021.

T. Hacıfendioğlu, B. Balıkoğlu, F. Aydın, İ. M. Öztürk, D. Asil “*Enhanced Photocurrent from PbSe Nanorod-Quantum Dot Bulk Nano-Heterojunction Platforms via Non-Radiative Energy Transfer*” *Journal of Materials Science: Materials in Electronics*, 1-11, 2021.

G. Birant, İ. M. Öztürk, D. Doğanay, H. E. Ünalın, A. Bek “*Rapid Deposition of Plasmonic Interfaces for Industrial Scale Monocrystalline Silicon Solar Cells*” *ACS Applied Nano Materials* 3 (12), 12231-12239, 2020.

W. Ahmed, Ö. Demirtaş, İ. M. Öztürk, A. Bek “*Monolayer Assembly of MultiSpiked Gold Nanoparticles for Surface-Enhanced Raman SpectroscopyBased Trace Detection of Dyes and Explosives*” *ACS Applied Nano Materials* 3 (7), 6766-6773, 2020.

Ö. Demirtaş, D. Doğanay, İ. M. Öztürk, H. E. Ünalın, A. Bek “*Facile Preparation of Nanoparticle Based SERS Substrates for Trace Molecule Detection*” *Physical Chemistry Chemical Physics* 22 (37), 21139-21146, 2020.

A. Elçi, Ö. Demirtaş, İ. M. Öztürk, A. Bek, E. N. Esentürk “*Synthesis of tin oxide-coated gold nanostars and evaluation of their surface enhanced Raman scattering activities*” *Journal of Materials Science* Volume 53 Issue 24 Page 16345-16356, 2018.

CONFERENCE PROCEEDINGS

E. Bilek, İ. M. Öztürk, Z. Demircioğlu, R. Turan “*Transparent Conductive Oxide Layer Characterization*” Poster, 24th Turkish National Optics, Electro-Optics and Photonics Workshop, 2023, Ankara, Türkiye

Ö. Demirtaş, G. A. Khan, S. S. Esmailzad, R. M. F. Iftikhar, İ. M. Öztürk, A. K. Demir, W. Ahmed, A. Bek “*SERS-based trace detection by size and shape controlled noble metal particles with high benefit-cost ratio*” Oral presentation by Ö. Demirtaş, SPIE Nanoscience + Engineering, 2021, San Diego, California, United States

H. A. Ersin, Ö. Demirtaş, İ. M. Öztürk, A. Bek “*A Universal Tip Enhanced Raman Spectroscopy Equipment for Opaque Samples*” Poster, 21st Turkish National Optics, Electro-Optics and Photonics Workshop, 2019, Ankara, Türkiye

S. S. Esmailzad, İ. M. Öztürk, M. Zolfaghariborra, N. Avishan, A. Bek “*Nanosphere Colloidal Coating for Improvement of Solar Cell Efficiency*” Oral presentation by S. S. Esmailzad, PVSEC 2018, 35th European Photovoltaic Solar Energy Conference and Exhibition, Brussels, Belgium

İ. M. Öztürk, Ö. Demirtaş, S. S. Esmailzad, A. Bek “*Fabrication of Large Area Plasmonic Interfaces for Quantum Optics Experiments*” Poster, KOBIT 2, 2nd Quantum Optics and Information Meeting, 2018, İstanbul, Türkiye

İ. M. Öztürk, S. S. Esmailzad, Ö. Demirtaş, A. Bek “*Computation of Raman Enhancement Factor of Isolated Plasmonic Nanostructures*” Poster, 20th Turkish National Optics, Electro-Optics and Photonics Workshop, 2018, Ankara, Türkiye

Ö. Demirtaş, O. Akdemir, İ. M. Öztürk, Ş. Coşkun, H. E. Ünalın, A. Bek “*Gümüş Nanotel Folyoların Yüzeyde Güçlendirilmiş Raman Saçılması*” Poster, 20th Turkish National Optics, Electro-Optics and Photonics Workshop, 2018, Ankara, Türkiye

İ. M. Öztürk, S.S. Esmailzad, Ö. Demirtaş, A. Bek “*Plazmonik Nano Yapıların Deşik Maske Kolloid Litografisi ile Karmaşık Geometrilerde Üretilmesi ve Karakterizasyonu*” Poster, 23. Condensed Matter Physics Ankara Meeting, 2017, Ankara, Türkiye, Best poster award

İ. M. Öztürk , S. S. Esmailzad, Ö. Demirtaş , A. Bek “*Plazmonik Nano Yapıların Deşik Maske Kolloid Litografisi ile Karmaşık Geometrilerde Üretilmesi ve*

Karakterizasyonu” Poster, 19th Turkish National Optics, Electro-Optics and Photonics Workshop, 2017, İstanbul, Türkiye

S.S. Esmailzad, İ. M. Öztürk, Ö. Demirtaş, A. Bek “Fabrication of Large Area Periodic Nanoholes Using Nanosphere Lithography”, Poster, 19th Turkish National Optics, Electro-Optics and Photonics Workshop, 2017, İstanbul, Türkiye

İ. M. Öztürk, Y. Kasap, A. Bek “Hole Mask Colloidal Lithography for Large Area Nanostructuring” Oral presentation, Nanotr 11, 11th Nanoscience and Nanotechnology Conference, 2015, Ankara, Türkiye

İ. M. Öztürk, A. Bek “Fabrication of Various Metal Nanostructures With Hole Mask Colloidal Lithography” Oral presentation, Solartr 3, Third Turkish Solar Energy Conference and Exhibition, 2015, Ankara, Türkiye

Y. Kasap, İ. M. Öztürk, A. Bek “Generation of Complex Plasmonic Structures for Solar Cell Applications by Hole Mask Colloidal Lithography” poster, Nanotr10, 10th Nanoscience and Nanotechnology Conference, 2014, İstanbul, Türkiye

I. Salakhutdinov, İ. M. Öztürk, E. Sarıgül, Y. Kasap, A. Bek “Güneş Gözeleri İçin Doğrusal Olmayan Plazmonik Çevirici” Poster, 15th Turkish National Optics, Electro-Optics and Photonics Workshop, 2013, Ankara, Türkiye